ALMA MATER STUDIORUM - UNIVERSITÀ DI BOLOGNA

SCUOLA DI INGEGNERIA E ARCHITETTURA

DIPARTIMENTO DI INGEGNERIA ELETTRICA E DELL'INFORMAZIONE "GUGLIELMO MARCONI"

LAUREA MAGISTRALE IN INGEGNERIA ENERGETICA

TESI DI LAUREA

in
Ingegneria dei Magneti e Superconduttività Applicata

Electromagnetic Analysis of Transients in the ITER PF Superconducting Joints

CANDIDATO   RELATORE:
Davide Lotito   Prof. Marco Breschi

CORRELATORE/CORRELATORI
Prof. Pier Luigi Ribani
Lorenzo Cavallucci

Anno Accademico 2017/2018

Sessione II

6. Numerical Transient Analysis of PFJEU1

Abstract

La reazione di fusione nucleare può essere considerata come una promettente alternativa alle fonti fossili negli impianti di produzione di energia elettrica. Un turboalternatore può convertire in elettricità il calore di fusione sviluppato nel reattore, che opera in condizioni stabili e in piena sicurezza, immettendo nella rete energia pulita da combustibile puro e abbondante con ridotto impatto ambientale; grazie a tale impianto l'energia prodotta risulta superiore all'energia introdotta per alimentare il reattore.

Il progetto ITER (International Thermonuclear Experimental Reactor) prevede lo sviluppo e la realizzazione di un prototipo di reattore a fusione nuceare, con lo scopo di ottenere dati sperimentali sulla fisica del plasma e verificare la stabilità e l'affidabilità di componenti ad alto contenuto tecnologico che operano in condizioni estreme di temperatura, corrente e campo magnetico.

La reazione di fusione nucleare avviene in una corrente di plasma confinata in una camera toroidale attraverso il campo magnetico prodotto da bobine superconduttive sottoposte ad alto campo magnetico (fino a 12 T) e alte correnti (fino a 100 kA), mantenute a temperature criogeniche (inferiori a 5 K) tramite una corrente di elio supercritico. I componenti del sistema magnetico di ITER devono essere adeguatamente progettati e testati per verificarne l'affidabilità durante tutta la vita utile della macchina, evitando costose operazioni di riparazione in caso di guasto; dato l'elevato costo di ogni test è necessario sviluppare modelli numerici per simulare il comportamento dei componenti in diverse condizioni operative.

In questo lavoro si analizzano, tramite due differenti modelli numerici, la resistenza elettrica in corrente continua (*DC Resistance*) e le perdite di energia in corrente alternata (*AC Losses*) del giunto superconduttivo che connette due avvolgimenti (Double Pancakes) della bobina inferiore del sistema magnetico per la generazione del campo poloiodale (Poloidal Field Coil), atto al controllo della posizione verticale della corrente di plasma. La validazione dei codici è basata sull'analisi sperimentale del campione PFJEU1 testato presso la SULTAN facility (Villigen, Switzerland) in Ottobre 2016.

1. The ITER project

The nuclear fusion reaction occurs in the stars, as our Sun, where the high gravity force confines a mix of elements in the plasma state burning at high temperature, up to $13.6 \cdot 10^6$ K; the International Thermonuclear Experimental Reactor (ITER) project aims to reproduce this phenomenon on the Earth, with the scope of obtaining data and gain experience in the fabrication of a new kind of electric power plant. ITER is the most ambitious worldwide project in the modern times, involving scientists, researchers and engineers from all over the world in the developing and manufacturing phases of the first thermonuclear fusion reactor that will produce net power.

ITER reactor will not be connected to the electric grid since it has been designed only to demonstrate the feasibility and the reliability of a stable and controlled nuclear fusion plant for the generation of 500 MW during a 400 s plasma pulse. This project is very challenging since high-tech engineering applications are required for the ignition, stabilization and confinement of the plasma current. The magnetic system consists of 44 superconducting coils divided in four main groups:

- 6 Central Solenoid (CS) coils for the ignition of plasma and generation of plasma pulse;
- 18 Toroidal Field (TF) coils for the magnetic confinement of the plasma;
- 6 Poloidal Field (PF) coils for the vertical stability of the plasma;
- 18 Correction Coils (CC) for the equilibrium of the plasma.

The superconducting coils operate at very high magnetic fields up to 12 T and high currents up to 100 kA; they are cooled with supercritical Helium at 4.2 K and assembled in a stainless steel cryostat. The structure requires 150000 km of superconducting strands and tons of stainless steel, for a total weight of the machine up to 23000 tons, storing a massive magnetic energy of 51 GJ with a plasma volume of 840 m^3.

The ITER Organization (IO) and the six Domestic Agencies (DAs), as United States, Europe, Russia, India, Korea, China and Japan, are involved in the development, manufacturing, testing and producing of the ITER components: the reactor is being assembled in Saint-Paul-lez-Durance, France, and the ignition of the first plasma pulse is delayed up to the 2025 from the previous reference schedule, exposed in Fig. 1. Fusion For Energy (F4E) is the European (EU) DA for ITER; it is responsible for the supply of 25% of the magnet system, in particular of 10 PF conductor unit length for PF6 coil, which need 45 tons of superconducting NbTi strand [1]
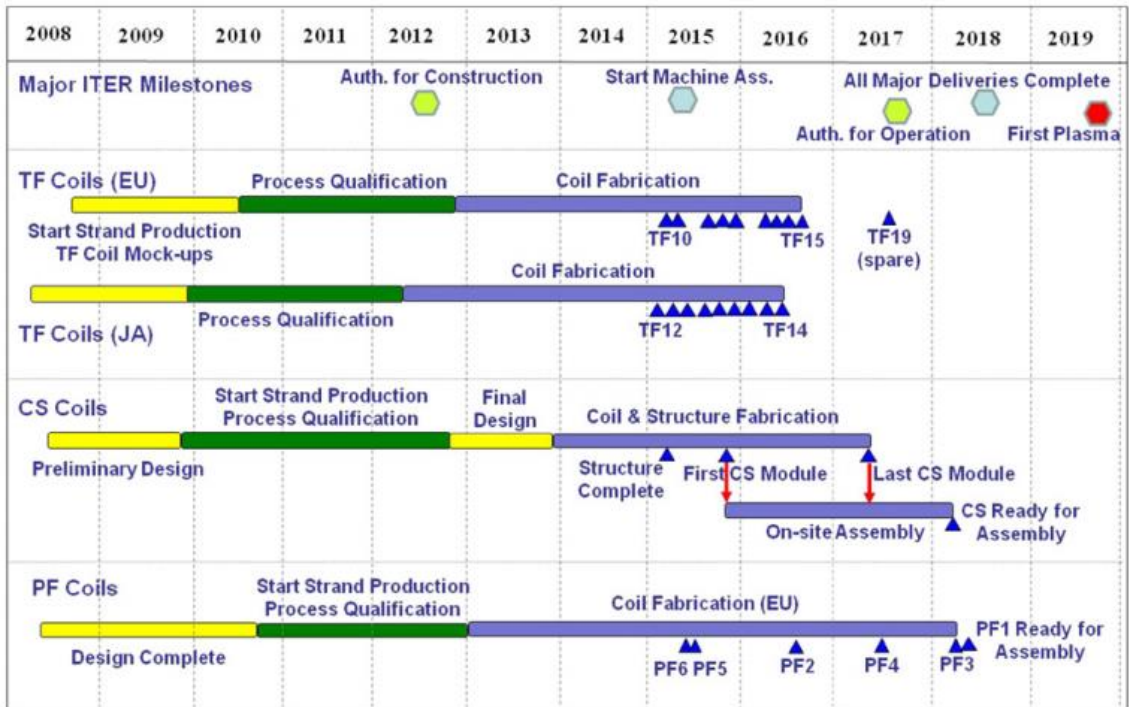
Fig. 1: Reference schedule for the delivery of ITER coils updated at 2007 [1].

Every component of the magnet system needs to be tested in the prequalification phase and the manufacturing process needs to be scaled from the laboratories to the industries; the final design of each coil will allow the ITER machine to operate in safety regime for 20 years in order to collect information about the physics of plasma and demonstrate the superconducting technology reliability in power applications.

In November 2018 a new milestone has been reached by the EAST tokamak in Heifei (China), where a 100 million Kelvin plasma current has been maintained for 10 seconds in the experimental reactor: this is a prove of the feasibility of the nuclear fusion reactor and more encouraging results are yet to come thanks to the effort of thousands of researchers all over the world. The first commercial nuclear fusion power plant is programmed to be built in the 2050 and will be designed to generate power 10 times higher than the power input needed to sustain the fusion reaction.

2. Theory of the Superconductivity

2.1. Introduction

Superconductivity was discovered by Onnes in the 1911 observing an unexpected drop of the resistance-temperature characteristic of the mercury approaching to cryogenic temperatures (Fig. 2 left). The energy of the crystal structure decreases with the temperature and electrons are less excited, therefore the bulk resistivity ρ [$\Omega \cdot m$] decreases linearly; when the temperature goes below a critical value T_C a real transition of phase from normal state to the superconducting state (as that from liquid to solid) is detected and resistivity suddenly drops: this is confirmed by a rough variation of the specific heat of the material during the cool down of the material. A perfect conductor is characterized by a null resistivity, nevertheless real bulk conductors are always affected by imperfections in the crystal structure due to the presence of chemical impurities and local fractures, therefore a very low resistivity is detected anyway: the Residual Resistivity Ratio RRR (Fig. 2 right) is the parameter that describes the purity of the conductor and is defined as the ratio between resistivity at room temperature $T_r = 293$ K and resistivity at cryogenic temperature T_{cryo}:

$$RRR = \frac{\rho(T_{room})}{\rho(T_{cryo})} \qquad (1)$$
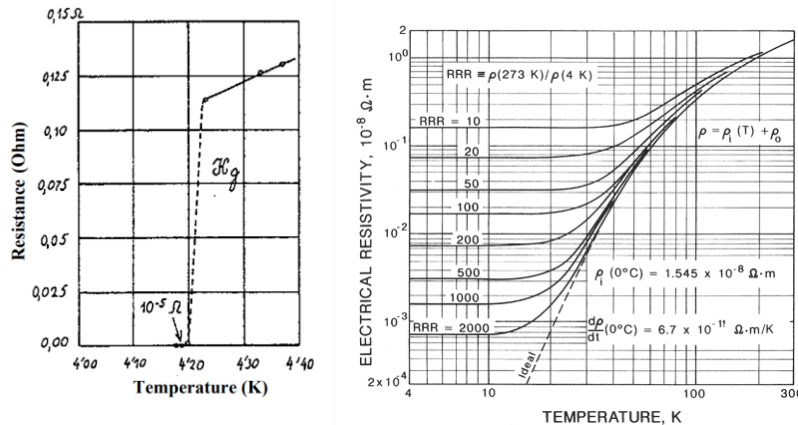
Fig. 2: The historical measurement of electric resistance of Mercury by Onnes in 1911 (left) and the *RRR* contribution to the electric resistance of the copper at cryogenic temperatures (right).

When the conductor reaches the perfect-conducting state with resistance $R(T) \sim 0\ \Omega$ is possible to transport high currents I_{DC} without losses P_{Joule} [W] since no Joule effect occurs under an imposed voltage of V_{DC}, therefore:

$$P_{Joule} = V_{DC} \cdot I_{DC} = R \cdot I_{DC}^2 \rightarrow 0 \qquad (2)$$

The current can flow without dissipation in the perfect conductor, therefore the induced currents generated by a background magnetic field variation lead to the magnetization of the perfect conductor since magnetic flux lines are retained inside the bulk material thanks to the current loops on its surface.

The superconductor (SC) is a perfect conductor with diamagnetic properties: the magnetic field is $B = 0$ T in all the superconducting domain both with static and varying background magnetic fields thus no magnetization is found (Meissner effect). A conductive material can reach the superconducting state if the temperature is maintained below the critical value T_c; if T_c is lower than 23.2 K we have a Low Temperature Superconductor (LTSC) cooled with liquid or supercritical Helium (He) below $T_{c_{He}} = 4.6$ K, whereas if T_c is higher than 23.2 K we have a High Temperature Superconductor (HTSC) cooled with liquid Nitrogen (N_2) below $T_{c_{N_2}} = 77$ K. LTSC such as NbTi and Nb3Sn are suitable for application in which high field (up to 12 T) and high current (up to 100 kA) are required, such as the ITER magnet system, where SCs are employed for the ignition, confinement and sustainability of the plasma current in the vacuum chamber of the ITER tokamak. The advantage of the superconductive technologies is the reduction of power dissipations in respect of conducting magnets. Superconductors are designed to work in cryogenic environment with a cooling system that protect the ITER tokamak from undesired thermal instability which can lead to an uncontrolled transition of the SCs to the normal state (quench). In the normal state the dissipated power goes linear with the conductor resistance, therefore an operative margin is must be considered for SCs to prevent the quench of the ITER tokamak under critical operating regimes.

2.2. The London Theory

The force balance for the electron in the bulk material is described by the equation:

$$e^- \cdot \vec{E} = \vec{F_v} + m\frac{d\vec{v}}{dt} \tag{3}$$

where $e^- = -1.602 \cdot 10^{-19}$ C and $m = 9.11 \cdot 10^{-31}$ Kg are the charge and the mass of the electron respectively, $\vec{E}$ is the electric field and $\vec{F_v}$ is the friction force due to the impacts with the ions in the crystal structure. If we consider an ideal superconductor with no imperfection, hence with no resistivity due to the irregular pattern of the crystal structure, the friction force is null and we obtain the First London Law:

$$\frac{\partial \vec{J}}{\partial t} = \frac{\vec{E}}{\mu_0 \lambda} \tag{4}$$

that allow us to evaluate the current flowing in the SC with a penetration length λ [m]:

$$\lambda = \sqrt{\frac{m}{\mu_0 n_e e^{-2}}} \sim 10^{-8} \tag{5}$$

where n_e is the number of electric charges. Eq. 4 can be integrated in time for the determination of the current density J in a perfect conductor under the electric field E. If we consider a normal conductor the *E-j* characteristic (as the *V - I* characteristic) is linear and depends from resistivity (resistance) of the material $\rho(T)$: if J goes below a critical value J_c and the conductor is maintained at cryogenic temperature $T < T_c$ no electric field (or voltage) is detected, proving that the current density $J < J_c$ can flow in the conductor without any resistance and heat generation [W] occurs due to the Joule effect:

$$P = R \cdot I^2 \tag{6}$$

When a varying external magnetic field $B_{ext}(t)=B_{max}sin(\omega t)$ is applied to a conducting material in the normal state, eddy currents flow in the external region according to the Faraday's Law:

$$\nabla \times \vec{E} = -\frac{\partial \vec{B}}{\partial t} \tag{7}$$

where the electric field $\vec{E}$ is equivalent to the voltage around a closed loop; from the diffusion equation of the magnetic field:

$$\nabla^2 \vec{B} - \frac{\mu_0}{\rho}\frac{\partial \vec{B}}{\partial t} = 0 \tag{8}$$

we obtain the penetration length δ [m] of the current:

$$\delta = \sqrt{\frac{2\rho}{\mu_0 \omega}} \tag{9}$$

In a normal conductor the lower is the frequency the higher is the penetration of the eddy currents, therefore a higher power loss is expected in the conductor. We define the magnetization M [A/m] of the conductor as the difference between the average value of magnetic field in the conductor and the applied external field:

$$M = \frac{1}{\mu_0}[< B(t) > -B_{ext}(t)] \tag{10}$$

8

The magnetic characteristic of the conductor depends from its magnetic susceptibility:

$$X = \frac{\mu_0 M}{B_{ext}} < 1 \tag{11}$$

When a perfect conductor is subjected to the same field variation, a magnetization is observed in the material even if the external field is no more present; this is due to the eddy currents flowing in the external region without resistance, thus maintaining the shielding field also in the steady state regime. For a superconducting material the skin depth of the eddy current is not dependent from the excitation frequency ω therefore the expulsion of the external magnetic field is observed also in steady state regime with constant background field: this is called Meissner effect and can be described well by the Second London Law:

$$\mu_0 \lambda^2 \nabla \times \vec{J} = -\vec{B} \tag{12}$$

The magnetic susceptibility of the superconductor is $X = -1$ thus having:

$$\mu_0 M = -B_{ext} = -\mu_0 H \tag{13}$$

This characteristic explains the expulsion of external magnetic field from the superconductor also for a constant background field because of the shielding currents flowing without any resistance. The diamagnetic properties of superconductors are present until external magnetic field does not exceed the critical value H_c: for higher background field the penetration length fulfill the conductor and $M = 0$ producing current flow and transition to the normal state.

2.3. The Critical State Theory

According to the "BCS Theory" (1950-1957) the current in the superconductors is due to super-electrons (Cooper duplet) flowing without any interaction with the crystal structure and thus not dissipating ohmic loss. Two types of superconductors can be identified considering the value of surface energy at the interface with a normal state domain of the conductor derived from the Ginzburg-Landau constant:

$$\Psi = \frac{\lambda}{\xi} \tag{14}$$

where ξ [m] is the coherence length of the superconductor.

Superconductors of Type 1 have $\Psi < 1/\sqrt{2}$. The density of super-electrons is considerable over $\xi \gg \lambda$ thus giving a positive surface energy in the superconducting domain: the superconducting state is favorite and the transition to the normal state is delimited in a few domains of large dimension (Fig. 3).
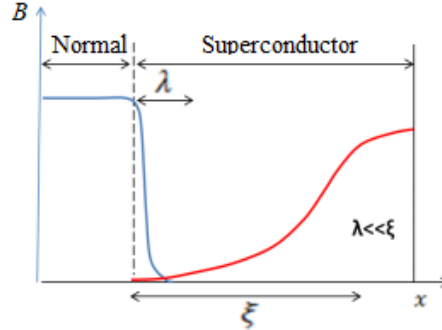

Fig. 3: Super-electrons distribution in a Type 1 SC.

Lots of pure elements, such as Li, Be, Hg, Al, Sn, Pb, Nb and Ti (Tab. 1.) are Type 1 LTSC with $\Psi \sim 0.02$ and T_c below 10^{-4}-10 K at atmospheric pressure: these materials are not interesting for industrial application because their low H_c (from 10 mT to 200 mT) which requires a very low temperature $T \ll T_c$ for the maintenance of the superconducting state. Type 1 SC are not affected by ohmic loss neither in DC nor in AC regime if $H < H_c$ and $J < J_c$.

Material	T_c(K)	λ_o (nm)	ξ_o (nm)	Δ_o (meV)	$\mu_o H_{co}$ (mT)
Al	1.18	50	1600	0.18	10.5
In	3.41	65	360	0.54	23.0
Sn	3.72	50	230	0.59	30.5
Pb	7.20	40	90	1.35	80.0
Nb	9.25	85	40	1.50	198.0

Tab. 1: Type 1 SC characteristics at 0 K [2].

Superconductors of Type 2 have $\Psi > 1/\sqrt{2}$. The density of super-electrons is considerable over $\xi \ll \lambda$ thus giving a negative surface density in the superconducting domain: the normal state is favorite and the transition occurs in a lot of domain with small dimension (Fig. 4)
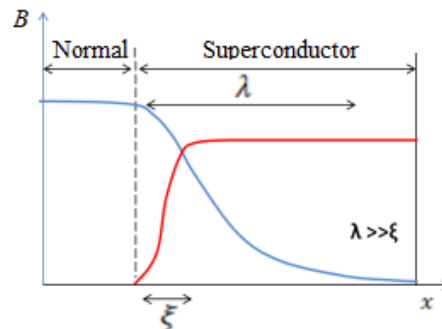

Fig. 4: Super-electrons distribution in a Type 1 SC.

Most of alloys and intermetallic compounds shown in Tab. 2, such as NbTi and Nb3Sn, are Type 2 LTSC with $\Psi \sim$ 10-100 and T_c between 7 K and 23 K.

Material	T_c(K)	$\lambda_{GL}(0)$(nm)	$\xi_{GL}(0)$(nm)	Δ_o (meV)	$\mu_o H_{c2,o}$(T)
Pb-In	7.0	150	30	1.2	0.2
Pb-Bi	8.3	200	20	1.7	0.5
Nb-Ti	9.5	300	4	1.5	13
Nb-N	16	200	5	2.4	15
PbMo$_6$S$_8$	15	200	2	2.4	60
V$_3$Ga	15	90	2–3	2.3	23
V$_3$Si	16	60	3	2.3	20
Nb$_3$Sn	18	65	3	3.4	23
Nb$_3$Ge	23	90	3	3.7	38

Tab. 2: Type 2 SC characteristics at 0 K [2].

Superconducting material of Type 2 are subjected to the penetration of a quantized magnetic flux called *fluxon*, defined as:

$$\Phi_0 = \frac{h}{2e^-} = 2.07 \cdot 10^{-15} \text{ Wb} \tag{15}$$

where $h = 6.626*10\text{-}34$ J·s is the Planck constant. If $T < T_c$ and $H < H_{c1}$ the Type 2 SC is in the Meissner State, therefore no magnetic field is found inside the superconductor. If the external field is $H > H_{c1}$ the superconductor enters in the Mixed State, which can be considered as a bi-phase system with normal and superconductors in equilibrium. Even if normal domains are present, there are still super-electrons carrying current with ohmic loss increasing as the number of fluxons in the superconductor increases, displacing themselves following the Abriskov hexagonal structure. When $H > H_{c2}$ the normal state saturates the superconductor and the transition of phase is detected (Fig. 5).
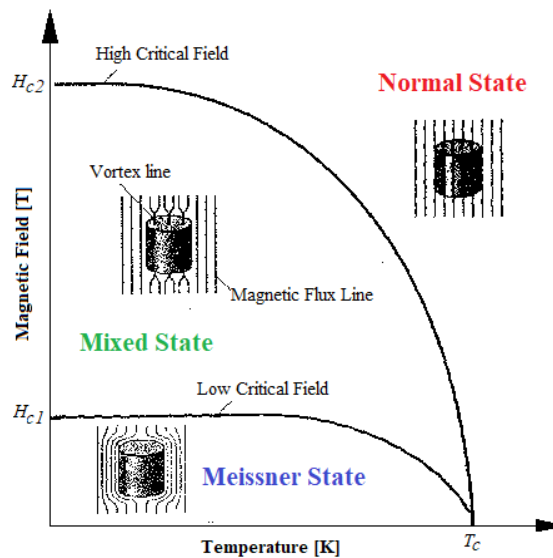

Fig. 5: Critical fields and transition regimes of a Type 2 SC in function of the temperature.

When a superconducting material in the Mixed state is subjected to an imposed transport current the interaction of J and B generates a transversal displacement of the fluxons, thus dissipating energy due to the induced resistance. In order to minimize those power losses the superconducting material should contain imperfections and impurities acting as pinning centers for fluxons, thus limiting their movements in the superconductor. Thanks to the impurities in the intermetallic superconductor, such as NbTi and Nb$_3$Sn, high pinning forces are imposed and superconductors can withstand to high magnetic field up to 10 T and high currents up to 100 kA.

The pinning force intensity determinates two different types of superconductors:

- Soft SC: weak pinning force and *Flux-Flow* loss due to a collective displacement of fluxons at constant velocity
- Hard SC: strong pinning force and *Flux-Jump* loss due to continuous and individual displacement of fluxons under thermal, mechanical and electrical disturbances of the superconductor.

We can say that Type 2 SC are not affected by ohmic loss neither in the DC nor in the AC regimes until $H < H_{c1}$, where the Meissner effect is guaranteed, but dissipation occurs when $H > H_{c1}$ because of the penetration of quantized magnetic flux.

The relation between critical current density and applied magnetic field can be expressed with different models exposed in Tab. 3.

$J(B) = J_c$	Bean (1962, 1964)
$J(B) = \dfrac{J_c}{\|B(x)\|/B_K}$	Fixed Pinning (Ji *et al.*, 1989; Le Blanc and Le Blanc, 1992)
$J(B) = \dfrac{J_c}{\|B(x)/B_K\|^{1/2}}$	Square Root (Le Blanc and Le Blanc, 1992)
$J(B) = \dfrac{J_c}{1 + \|B(x)\|/B_K}$	Kim (Kim *et al.*, 1962, 1963)
$J(B) = J_c \exp[-\|B(x)\|/B_K]$	Exponential (Fietz *et al.*, 1964)
$J(B) = J_c - J_c'\|B(x)\|/B_K$	Linear (Watson, 1968)
$J(B) = \dfrac{J_c}{1 + [\|B(x)\|/B_K]^2}$	Quadratic (Leta *et al.*, 1992)
$J(B) = J_c(1 - \|B(x)\|/B_K)\Theta(B_K - \|B(x)\|)$	Triangular Pulse (Dersch and Blatter, 1988)
$J(B) = \dfrac{J_c}{[1 + \|B(x)\|/B_K]^\beta}$	Generalized (Lam *et al.*, 1990; M. Xu *et al.*, 1990)

Tab. 3: Expressions of critical current density as function of magnetic field according to different authors.

The critical current density J_c of the superconductor can be estimated with the Four Contact Method shown in Fig. 6 by the measurement of the voltage generated in a conductor sample laying in a cryogenic environment with $T < T_c$.
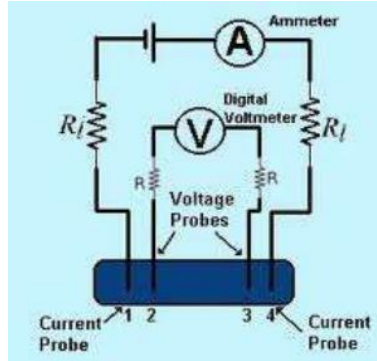

Fig. 6: Four Contact Method for the critical current evaluation of a superconducting sample.

Since $I_t < I_c$ no voltage is found in the sample, thus no resistance is present therefore no power is dissipated; when $I_t \rightarrow I_c$ the voltage becomes to raise thus evidencing the initiating of resistive behavior of the sample.

We can assume that the transition to the normal state occurs when $E(J) > E_0 = 10^{-4}$ V/m.

2.4. Stability of superconductors

Superconductors always works with an adequate operating margin thus allowing negligible perturbations of J, T and B around the design operating scenario. If the local current density J exceeds the critical value J_c due to electric, thermal and mechanical perturbations, a resistivity $\rho > 0$ appears thus generating local temperature increasing (Hot Spots) that must be removed with the cooling Helium mass flow ensuring $T_{op}<T_c$ in the SC. If the heat load is well distributed in the SC a fast removal of the dissipated power is possible and the local transition to the normal state is reversible (*recovery*), but if the Hot Spot is concentrated in a small region and the refrigerating power is not sufficient the thermal instability propagates in the SC and the transition to the normal state cannot be avoided (*quench*). The energy balance equation used for the quench energy evaluation is:

$$\frac{\partial e}{\partial t} = c_p \frac{\partial T}{\partial t} = q_k + q_j + q_d - q_c \tag{16}$$

where q_k is the convective power, q_j is the ohmic loss, q_d is the periodic or permanent thermal perturbation and q_c is the cooling power density; all quantities are expressed in [W/m^3].

2.4.1. The Current Sharing regime

If we consider that $q_k = q_j$ at the steady state regime, with:

$$q_k = -k \cdot \nabla T = 2k \cdot \frac{A}{l}\left(T_c - T_{op}\right) \tag{17}$$

$$q_j = R \cdot I^2 = \rho \cdot A \cdot l \cdot J_c^2 \tag{18}$$

where A [m^2] is the SC cross section with length l [m] and k [W/m$^3 \cdot$K] is the thermal diffusivity, we obtain the recovery length l_{rec} [m] which is the maximum length of the Hot Spot that allows to avoid the quench of the conductor:

$$l_{rec} = \sqrt{\frac{2k\left(T_c - T_{op}\right)}{\rho \cdot J_c^2}} \tag{19}$$

In a pure SC we have $l_{rec} = 0.5$ μm and for thin SCs a very low dissipation (less than 10^{-9} J) can initiate the quench, therefore a stability support of resistive material, such as copper or silver, must be considered for the superconductor in order to limit the current and prevent local instabilities: the composite SC can operate in the "current sharing" mode in the temperature range between current sharing temperature T_{cs} and critical current T_c, as we can see in Fig. 7a,c.
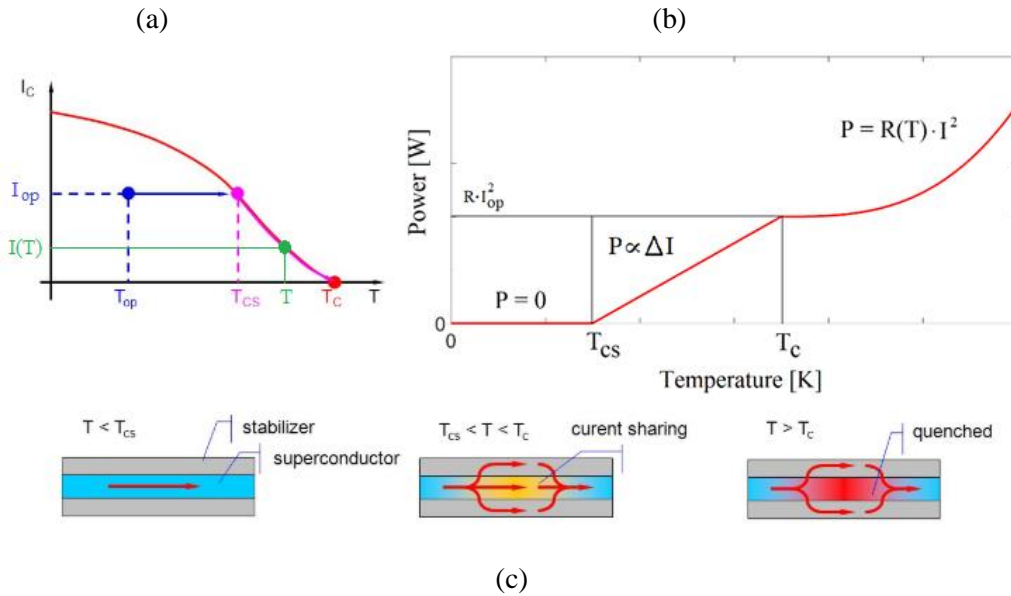

Fig. 7: (a) Current value in the "current sharing" mode, (b) power evolution in a composite superconductor and (c) visual description of the "current sharing" regime, from the superconducting state to the quench phase.

If $T > T_{cs}$ the SC carries only the $I_{op} = I_c$, whereas the exceeding current $\Delta I = I_{op}$-$I(T)$ is carried by the stability copper support: since copper resistance is constant the power dissipation will increase linearly with the temperature, and thus proportionally with the current flowing in the composite superconductor. When $T > T_c$ the quench of the SC forces the current to flow only in the stability support, thus dissipations increase depending from the resistance, varying with the temperature, and the square of the current. The dissipated power profile with temperature is shown in Fig 7b.

The composite SC equivalent electrical circuit is a parallel of short circuit for the superconductor and a non linear resistance $R_{Cu} = f(T)$ representing the stability copper support. If the magnetic field B increases, $T_c = f(B)$ decreases due to the magnetoresistance of the stability copper and the operative regime is restricted: the current sharing regime is initiate at lower temperature, therefore operating currents must be decreased in order to prevent the SC quench.

2.4.2. Cryogenic stabilization

A solution for the safe removal of thermal load in SCs consists of the permitted quench of all the superconducting domain, whose temperature is maintained constant by the adequate cooling helium mass flow: considering $q_c \geq q_j$ at the steady state, with:

$$q_c = \frac{h \cdot p \cdot f}{S_{tot}} \cdot (T - T_{He}) \tag{20}$$

where h [W/m^2] is the thermic exchange coefficient of the Helium bath, p [m] is the perimeter of the SC, f is a reduction factor and S_{tot} is the cross section of the composite SC, we can safely recover the whole SC before Joule loss initiate the quench.

This stability method is possible only if the SC has a specific geometry and the temperature of the helium is low enough, resulting in a Stekly parameter's value of:

$$\alpha = \frac{h \cdot p \cdot f \cdot S_{Cu}}{\rho_{Cu} I_{Cu}^2} (T - T_{He}) > 1 \tag{21}$$

2.4.3. Active protection

If we assume that a quench has propagated along the SC and the operating current exceed the critical value, we can dissipate the power in two different ways:

- an internal resistance (ohmic heater) able to induce the transition of the whole SC thus preventing local Hot Spots and distributing the dissipation in a larger volume;

- an external resistance (dumper) connect the SC to the ground dissipating the power loss and preventing the fusion of the superconducting material at the temperature $T_f \sim 500$ K if the following relation is respected:

$$\int_{T_{op}}^{T_f} \frac{c_p(T)}{\rho_{Cu}(T)} dT > \frac{S_{Cu}}{S_{tot}} J_{op}^2 \int_0^\infty e^{-\frac{2t}{\tau}} dt \qquad (22)$$

where $\tau = L_m/R_d$ [s] is the time constant of the dumping circuit in Fig. 8.

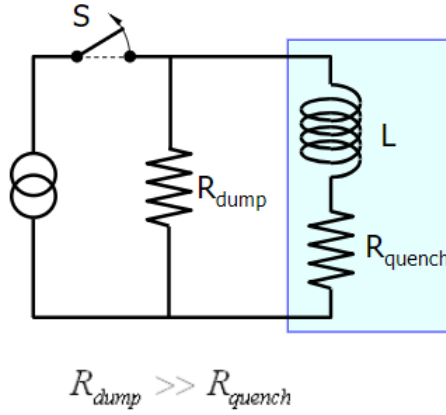
$$R_{dump} \gg R_{quench}$$

Fig. 8: Electric circuit of an active protection with external dump resistance.

From the previous equation we can obtain the characteristic parameter for the composite SC:

$$\Gamma(T_{op}, T_f) > \frac{S_{Cu}}{S_{tot}} J_{op}^2 \frac{\tau}{2} \qquad (23)$$

where the time constant τ depends on the stored energy and voltage in the SC and is defined considering the voltage V_d over the dumping resistance and the energy E_m stored in the coil until the quench detection:

$$\tau = \frac{2E_m}{V_d I_{op}} \qquad (24)$$

The maximum operating current in the SC is then:

$$J_{op}^{max} < \sqrt{\frac{V_d I_{op} S_{tot}}{S_{Cu} E_m} \cdot \Gamma(T_{op}, T_f)} \qquad (25)$$

16

3. Superconductors for Fusion Magnets

3.1. Superconducting materials

The ITER magnet system requests tons of NbTi and Nb_3Sn conductors for stabilization and control of the plasma current in the tokamak. These materials, which properties are exposed in Tab. 4, have been chosen as conductors in superconducting coils with multi-staged twisted cables transporting very high currents in background magnetic fields up to 11 T for NbTi ad up to 20 T for Nb_3Sn.
The development and industrial manufacturing of such these SCs must withstand some characteristics:

- superconducting materials should have good mechanical and workability properties that allow for the manufacturing of long unit length with uniform characteristics, thus optimizing the production process obtaining high quality SCs at a sustainable cost;

- cables must be realized with multi-filamentary twisted superconductors with very small size (less than 1 mm in diameter) to reduce hysteresis losses;

- the stability copper matrix must have high electrical and thermal conductivity, resulting in a very pure conductor with high value of *RRR* to reduce ohmic loss and protect the superconducting filaments from quench in case of temperature or current increasing; it also ensures good mechanical stability during the manufacturing process of the twisted cable

Properties	Unit	Nb47%Ti	Nb3Sn
Tc at 0T	K	10	18,3
Magnetic field	T(max)	11	25
Critical current density	A/mm2	3300 (5T), 400 (9,5T)	12000 (5T), 3000 (12T)
Structure		Solid solution alloy	Intermetallic compound
Ductility		Ductile/tough	Ductile, brittle (after reaction)
Manufacturing methods		Co-process, hot/cold	Internal-Tin
		Precipitation HT	Bronze
			Power-In-Tube
Max unit length	km	50 - 270	10 - 40
Max unit weight	kg	200-450	50-100
typical final diameter	mm	0,4 - 2,0	0,6 - 1,5
Cu/Sc-ratio		1- 14	0,3 - 1,5
Filament size	micrometer	2,5 - 120	2 - 6
Filament number		1- 40 000	3000 - 40 000
Price	EUR/kg	50-200	500 - 1000
Technical price	EUR/kAm	1-4	10-20

Tab. 4: Properties and manufacturing characteristics of NbTi and Nb_3Sn superconductors.

3.1.1. NbTi

The NbTi is a Type 2 superconducting intermetallic alloy with typical Nb content up to 40-50% (β-phase) that is found in solid state after heat treatments up to 800 °C for 40-160 h for the stabilization of pinning centers located at the α-phase NbTi, with low content of Nb up to 5%; adding a low percentage of Tantalium (Ta) the operative margin can be raised by ΔT=0.5 K and ΔH_{c2}= 1-2 T, thus improving the conductor performances for engineering applications. This SC is able to withstand to critical high field H_{c2} up to 11 T with a critic temperature T_c = 9.5 K.

The manufacturing process of NbTi SC consists of two phases, starting from a "powder-in-tube" manufactured NbTi cylindrical ingot with diameter d = 20 cm, height h = 76 cm and weight of 136 kg to create the superconducting rods (Fig. 9); after the heat treatment for the omogeneization of pinning centers the cable is assembled by twisting multi-filamentary superconductor strands in a multi-staged pattern (Fig. 10); the number of superconducting wires, the layout of the cable and the purity of the copper matrix can be adjusted depending from the application of the SC.
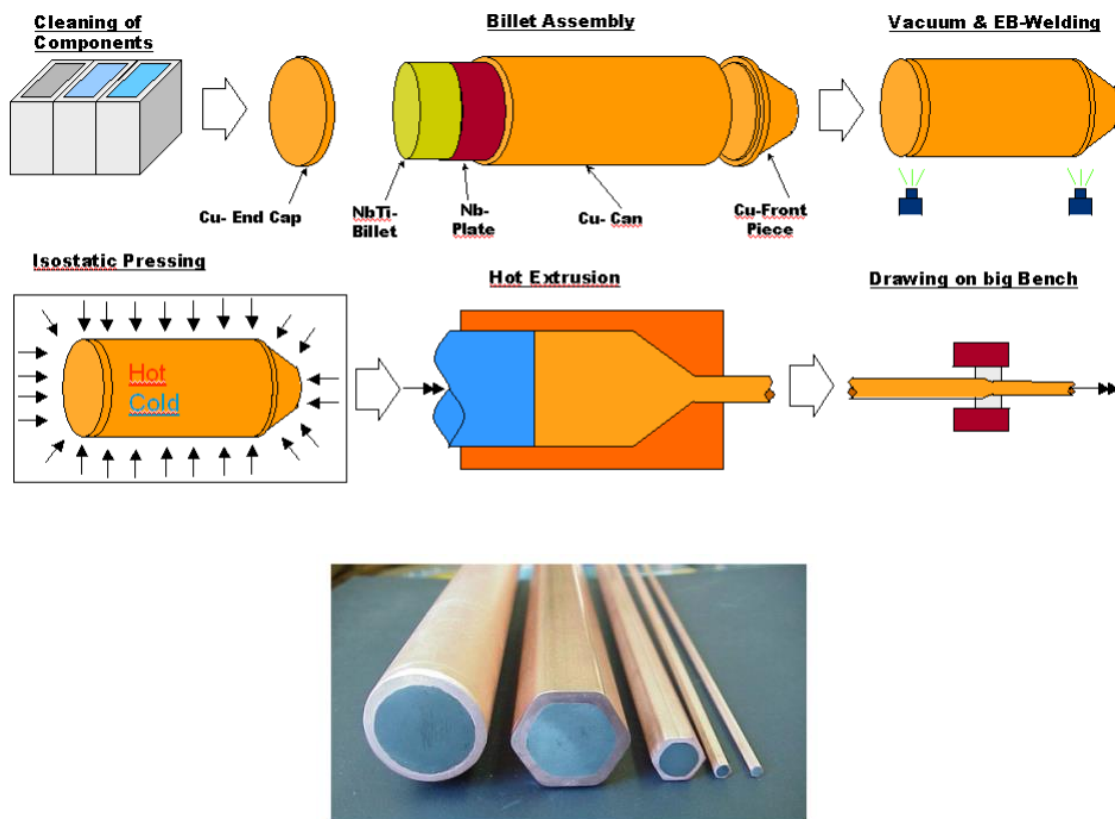

Fig. 9: Manufacturing process of a single superconducting filament (top) and comparison between superconducting filaments of different dimension and shape (bottom) [3].
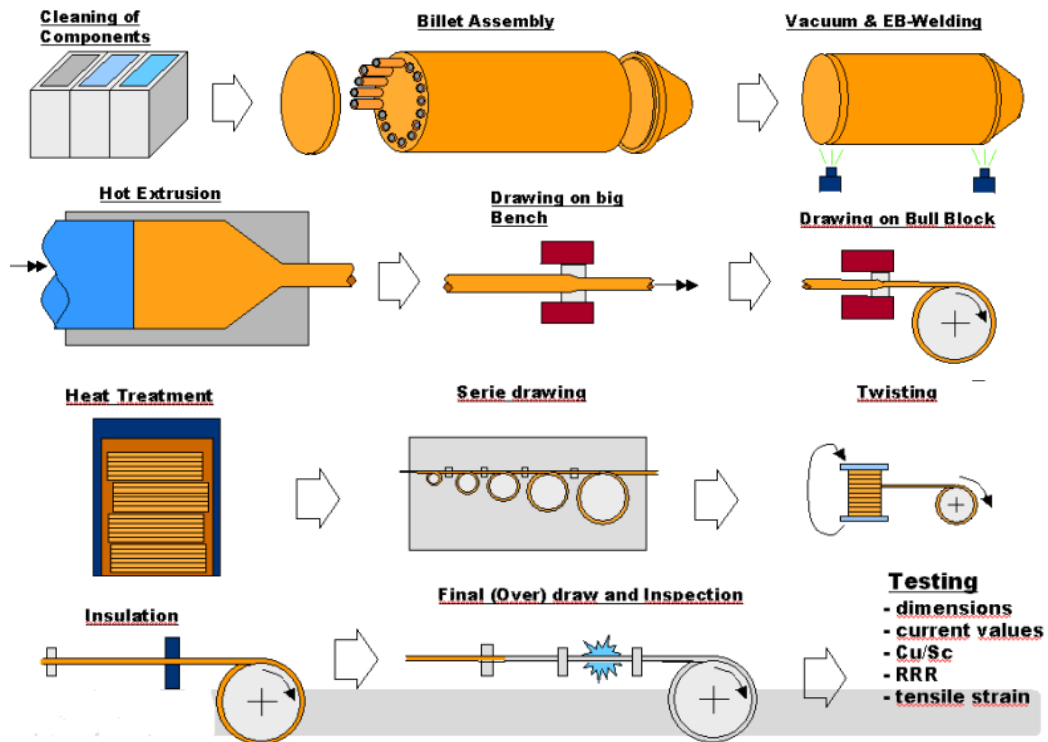
Fig. 10: Manufacturing process of the twisted multistrand composite superconductor [3].

3.1.2. Nb₃Sn

Nb$_3$Sn is an intermetallic compound found in the stable suoerconducting phase only if is subjected to a high temperature treatment up to 1000 °C: pinning center are located at the interfaces of the crystal structure thus heat treatment is needed to improving the operatig regime; however the superconducting state is distinguished by a very low mechanical resistance thus leading to an easy degradation of the conductor performances. In addiction the intrinsic fragility of Nb$_3$Sn SC takes to a strong dependence of the critical field and current density from the mechanical deformation (effective strain) of the wires during mechanical and electromagnetic loads.

If the Nb$_3$Sn SC is wounded in coils after the heat treatment (*react & wind*) the risk of a breakage in the multistrand cable is high; it is preferred to produce the superconducting phase after the winding process (*wind & react*) but the coil structure must be designed considering high thermal loads. Nb$_3$Sn SC can be obtained in three different ways (Fig. 11):

-   With the "Bronze" process a single wire is realized inserting various Nb filamets in a α-Bronze matrix (Cu+Sn) that diffuses in the copper during the heat treatment, producing Nb$_3$Sn; the stabilization copper is protected by an antidiffusion barrier made of Ta or Ta/Nb maintaining copper high purity.

19

- With the "Internal Sn" process a Sn core diffuses in the copper matrix containing Nb filaments and enclosed in an antidiffusion barrier, thus producing Nb_3Sn and bronze; this method is suitable for the *wind & react* process since precursors of the matrix bronze are more ductile than the bronze itself.
- With the "Powder-In-Tube" process a mixture of powdered $NbSn_2$ and Cu is inserted in a Nb tube in which the excessive Sn diffuses during the heat treatment producing Nb_3Sn and ensuring high values of *RRR*.
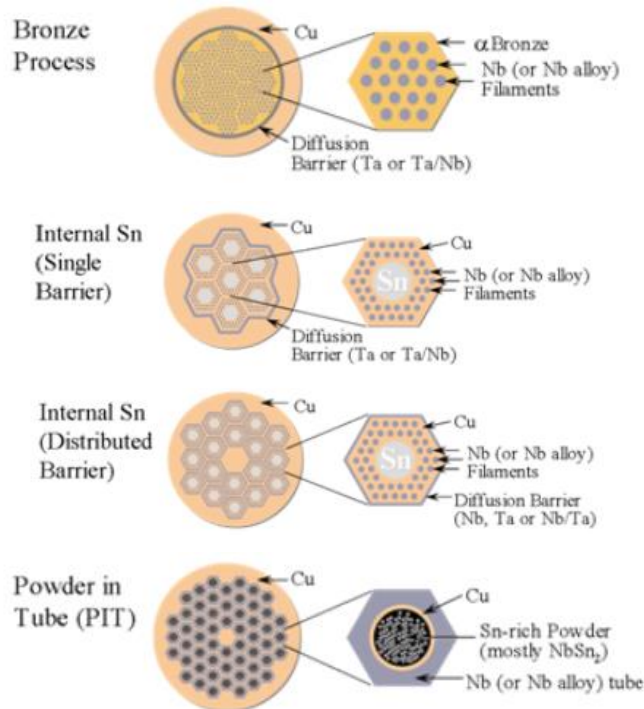
Fig. 11: Different manufacturing processes for Nb3Sn superconducting wires.

3.2. The ITER conductors

Superconducting coils of ITER magnet system are specifically designed to operate at different maximum values of magnetic field and current depending from the function and the position in the tokamak. Each coil consists of a superconducting cable wound in racetrack (TF) or circular (PF, CS) configuration.

The mechanical stability is ensured by rigid jackets made of high resistive materials, such as stainless steel or Incoloy, in which superconducting multi-stage twisted cable is embedded: this configuration is typical of Cable-In-Conduit conductors (CICC). Electrical insulation must be taken in account due to the high voltages induced between coil terminal during normal operations.

Because of the limited length of SC coming from the production industries, the coil is wounded considering different superconductor unit lengths that must be connected in series using superconducting joints.

Joints between two superconductors have always been a very sensitive issue in superconducting magnets, which in the past have underperformed due to problems or failure in the electrical connections. The high transport current in the conductors must flow through the whole coil: the connection must be low resistive and must operate under temperature margins to prevent the quench of the coil due to the redistribution of the ohmic heating from the joint to the cables, however the AC losses generated by the eddy current occurring during a time variation of the background magnetic field must be acceptable, thus requiring a more resistive electrical connection. A simplified sketch of an electrical connection (copper sole) between two superconducting cables is shown in Fig. 12.
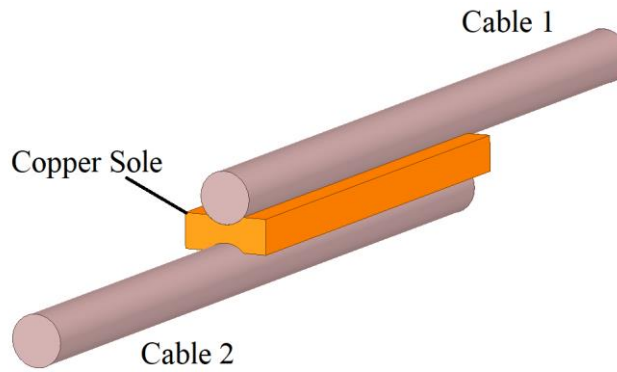

Fig. 12: Sketch of the electrical connection of two superconducting cables through a copper sole.

3.3. DC resistance

The DC resistance R [Ω] of a solid conductor in the normal state with regular geometry (Fig. 13) depends from geometrical parameter and from resistivity ρ [$\Omega \cdot$m] following the equation:

$$R = \rho \cdot \frac{h}{A} \tag{26}$$

where $A = L \cdot w$ [m^2] is the cross section perpendicular to the current path and h [m] is the length of the current path. In the superconducting joints current paths can interest both copper and stainless steel with an intensity proportional to the bulk conductivity c [S/m] defined as the inverse of metal resistivity.
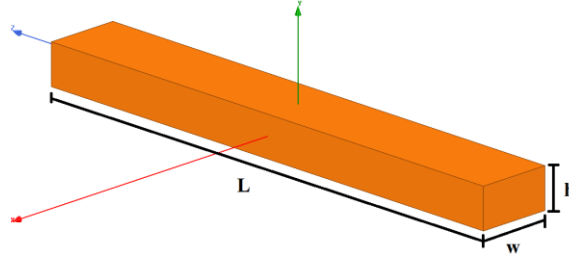
Fig. 13: Regular copper domain.

Stainless steel resistivity ρ_{SS} is a function of temperature T [K] only, according to the fit of data quoted by J. Davis [4]:

$$\rho_{SS}(T) = 76.2063 + 0.071375 \cdot (T - 273.15) - 2.3109 \cdot 10^{-5} \cdot (T - 273.15)^2 \tag{27}$$

Copper resistivity ρ_{Cu} is a function of temperature T [K], applied magnetic field B [T] and RRR, according to J.Simon, E.S.Drexler and R.P.Reed [5]. We first evaluate the following resistivities:

$$\rho_1'(T) = \frac{1,171 \cdot 10^{-17} \cdot T^{4.49}}{1 + \left\{ 4.5 \cdot 10^{-7} \cdot T^{3.35} \cdot \left[e^{-\left(\frac{50}{T}\right)^{6.428}} \right] \right\}} \tag{28}$$

$$\rho_2'(RRR, T) = \frac{1.69 \cdot 10^{-8}}{RRR} + \rho_1' + 0.4531 \cdot \left(\frac{1.69 \cdot 10^{-8} \cdot \rho_1'}{RRR \cdot \rho_1' + 1.69 \cdot 10^{-8}} \right) \tag{29}$$

If $B \leq 1$ T the copper resistivity is:

$$\rho_{Cu} = \rho_{Cu}(RRR, T) = \rho_2'(RRR, T) \tag{30}$$

If $B > 1$ T we need to define the following parameters, thus taking in account the magnetoresistive effect:

$$A(RRR, T, B) = log\left(\frac{1.553 \cdot 10^{-8} \cdot B}{\rho_2'(RRR, T)} \right) \tag{31}$$

$$a = -2.662 + 0.3168 \cdot A + 0.6229 \cdot A^2 - 0.1839 \cdot A^3 + 0.01827 \cdot A^4 \tag{32}$$

Then the copper resistivity is:

$$\rho_{Cu} = \rho_{Cu}(RRR, T, B) = \rho_2'(RRR, T) \cdot (1 + 10^a) \tag{33}$$

22

As a first indication we assume that the joint with copper $RRR = 6$ is placed in a cryogenic environment with $T = 4.5$ K under a background field of $B = 3$ T, therefore $\rho_{Cu} = 2.88 \cdot 10^{-9}$ $\Omega \cdot$m and $\rho_{SS} = 5.53 \cdot 10^{-7}$ $\Omega \cdot$m: the copper is 100 times less resistive than the stainless steel, therefore a higher current density is expected in the copper sole during the current transfer between superconducting cables. Considering a simplified model of the copper sole, as that in Fig. 13, having $L = 450$ mm, $w = 64$ mm and $h = 35$ mm, a first order approximation of the joint resistance could be:

$$R_{joint} = \rho_{Cu} \cdot \frac{h}{L \cdot w} \tag{34}$$

with $R_{joint} = 3.5 \cdot 10^{-9}$ Ω. When a difference of potential is imposed on the conductor, a DC current I_{joint} [A] flows across the copper sole with uniform current density along the sole length in contact with the cable. The PF joint operates in pulse mode thus dissipating the ohmic power:

$$P_{joint} = R_{joint} \cdot I_{op}^2 \tag{35}$$

The electric resistance of the joint in DC regime is a crucial parameter for the stability of the conductors since the ohmic heating of the copper sole has to be removed with the cooling helium mass flow $\dot{m}$, with inlet temperature of $T_{in} = 4.5$ K to ensure a constant temperature in the joint, preventing local quench of the conductor; in order to limit the impact of the joint resistance to the conductor temperature margin, ΔT_r is set lower than 0.05 K.

The DC resistance is obtained from both voltmetric and calorimetric method according to the following equations:

$$R_{joint} = \frac{V_{joint}}{I_{op}} \tag{36}$$

$$R_{joint} = \frac{2\dot{m} \cdot \Delta H}{I_{op}^2} \cdot \Delta T_{He} \tag{37}$$

Joints are always in current sharing mode since current flows from a superconducting cable to the other crossing the joint copper sole: since the joint is located in low field region, the stability margin at the joint is much higher than in the conductor, in which current path is found to be more homogeneous [6].

To limit DC resistance the contact surface between cable and copper sole can be adequately treated by removing of resistive barrier of the cable (de-wrapping external petal surface and mechanical brushing of Ni-coated strands) and silver coating of the copper and cable contact

surfaces. Low resistive joints can be obtained also compacting the cable in the joint to reach a local void fraction of less than 25% and soldering the strands in contact with the copper sole.

3.4. AC losses

When an electric component with resistivity ρ [$\Omega \cdot$m] is subjected to a time variation of the background field, an electromotive force (*e.m.f.*) appears, producing current loops according to the Faraday's law (eq. 7). Eddy currents generate a shielding field, opposite to the external varying field, decaying with a characteristic time constant and saturating at the steady state regime until the end of the magnetic transient when $dB/dt = 0$. In a pure resistive material ohmic heating occurs when the energy of the current loops is released, producing power dissipation (AC loss) and temperature rising that can be transferred to the superconducting cable inducing local instabilities. Each strand in the cable represents a complex spiral with several twist pitches: when the magnetic flux linked to that conductor changes in time, an *e.m.f.* is induced and the shielding current returns through the copper block thus closing the loop (see Fig. 16). The total AC loss per cycle [J/cycle] can be expressed as the sum of three components according to [7]:

$$E_{AC} = E_h + E_c + E_{ec} \tag{38}$$

3.4.1. Hysteresis losses

Hysteresis losses E_h occur in superconducting filaments of Type 2 with diamagnetic properties due to presence of the eddy currents penetrating in the SC with a skin depth λ [m] and depends on the filament radius a [m], the critical current density $J_c(B,T)$, the operating current and the magnetic field ramp amplitude [8].
Consider the generalized Kim model for the critical state, for which the critical current density J_c depends from the background field:

$$J_c(B) = \frac{J_{c_0}}{1 + \left(\frac{B}{B_k}\right)^{\beta}} \tag{39}$$

where B_k is the induced field that takes the J_c to be halved without external field (determined from the fitting of experimental data for the SC, as β and J_{c_0}).

In this case the superconductor (supposed with infinite length) subjected to a varying background field B_a with $\Delta B = B_{max} - B_{min}$ and a transport current I_t will be interested by an energy loss per cycle proportional to:

$$E_h \sim a\Delta B \cdot J_c(B)\left[1 + \left(\frac{I_t}{I_c(B)}\right)^2\right] \tag{40}$$

Hysteresis loss dramatically decreases with cycling EM loading in Nb$_3$Sn filaments whereas remains the same for NbTi, thus allowing us to consider this contribution as a constant in NbTi SCs. In Fig. 14 we can see a typical hysteresis cycle for a SC in which the area of the cycle is numerically equivalent to the energy loss per cycle. This value is independent from both the frequency and the shape of the magnetic field variation and only depends from ΔB and the maximum penetrating field B_p.
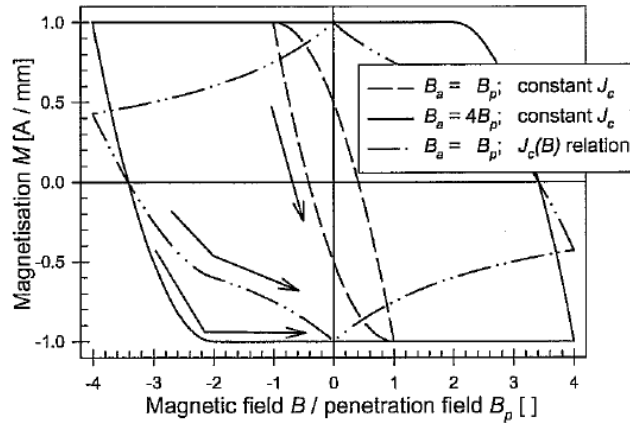

Fig. 14: Hysteresis cycle for superconductors in function of the critical current.

We can say that taking in account the relation between Jc and B given by the Kim model where $Jc = f(B)$ the hysteresis loss is lower than in the Beam model, where Jc is constant with the magnetic field and hysteresis loss evaluation is more conservative due to a higher total area of the magnetization cycle.

3.4.2. Coupling losses

Coupling losses E_c are related to the shielding current transfer from a superconducting element (strand, bundle, petal) through the resistive material closing the current loop generated by a background field variation in the twisted cables; coupling losses depend on the geometrical characteristics of the cable, such as radius and length, the resistivity of the conductor, the field

ramp rate and amplitude, whereas are independent from the Cu/non Cu ratio in the cable and from the number of SC strands in a bundle.

If shielding currents flow only in the surface of superconducting filaments (Fig. 15 left) the magnetic field in the matrix remains equal to the applied external field and only hysteresis losses in SC domain are detected; when superconducting filaments are coupled (Fig. 15 right) the shielding current flowing in the copper matrix is dominant in respect of the current in the SC, flowing without resistance in the longitudinal direction, and the induced voltage generate losses due to the non null resistivity of copper matrix. The twisted layout allows for a reduction of coupling currents between superconducting filaments in the strands.
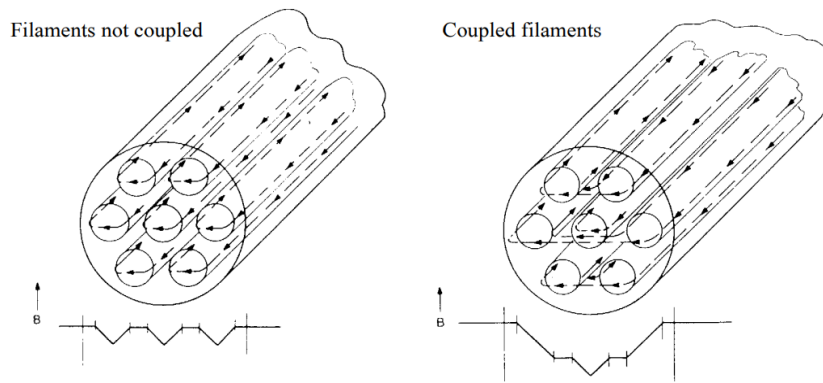

Fig. 15: Magnetic field profile inside a simplified composite SC strand without (left) and with (right) coupled filaments; the first is related to the hysteresis losses whereas the latter is related to the coupling losses.

In a simplified model proposed by N.N. Martovetsky [6] the *e.m.f.* E [V] imposed on a twisted cable for a field variation along joint transversal section is:

$$E = \frac{l_p}{2\pi} \cdot \frac{\partial B}{\partial t}$$

(41)

and the coupling loss per unit cable space volume [W/m^3] is:

$$P = \frac{n\tau}{\mu_0} \cdot \frac{\partial^2 B}{\partial t^2}$$

(42)

where $n\tau$ is the coupling loss parameter with $n=2$ for round cable and τ [s] is the coupling time constant. The $n\tau$ value increases if low void fraction is found in the cable, less than 35% [10], however a high compaction is necessary to guarantee low DC resistance but it results in higher AC loss.

26

In Fig. 16 we can see the projection of the full twist pitch loop generated by the single strand in a cable with radius $r = 5$ mm and pitch length $l_p=120$ mm, both in the transversal and longitudinal cross sections:
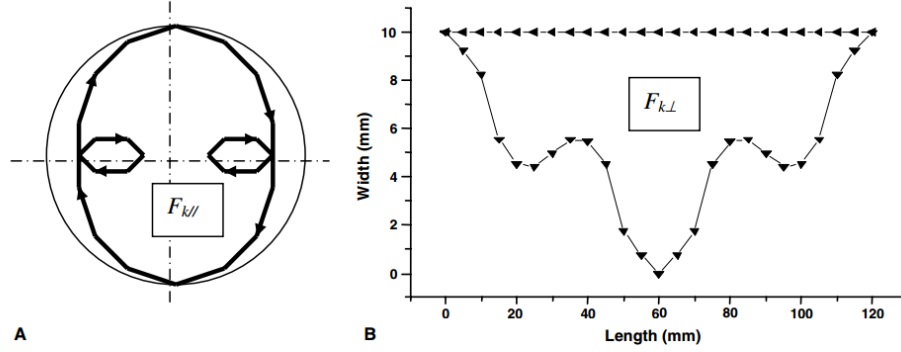

Fig. 16: Projection of the full twist pitch loop of a single strand (a) in the transvers cross section and (b) in the parallel cross section of the cable [9].

The respective electric circuits are shown in Fig. 17 considering independently a field variation on the longitudinal direction $B_{/\!/}$ and on the transversal direction $B\perp$; in this case the current transfer in the resistive domain has opposite directions and interest a half of the resistive cross section. Is known that in the superconducting domain no resistance is found, therefore the SC line comprises only the inductance of the loop and the *e.m.f* due to the magnetic field variation.
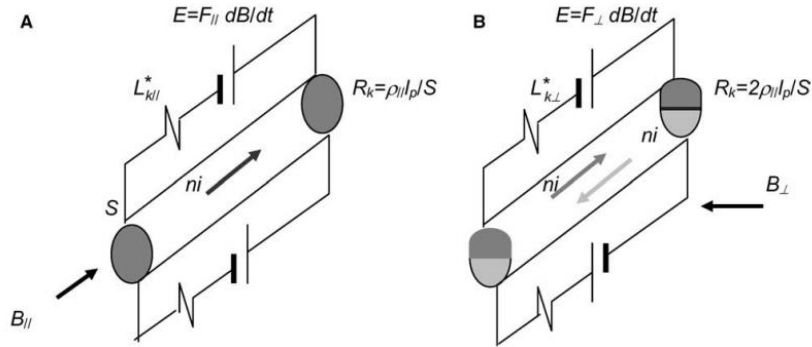

Fig. 17: Equivalent electrical circuits for coupling currents in case of (a) parallel field variation and (b) transversal field variation [9].

In accordance with [9] a CICC bundle (sub-cable) can be considered as a monolithic and porous non-superconducting copper matrix with m superconducting full twist pitches embedded within the matrix. The equation to determinate the current i_j generated in every twist pitch formed loop of the *j*-th cable stage is:

$$L_j \frac{di_j}{dt} + m_j R_j i_j = F_j \frac{dB_{ext}}{dt} \tag{43}$$

27

As shown in Fig 18 the layout of a PF6 conductor is 3×4×4×5×6 NbTi strands twisted around a hollow channel with five different twist pitches evidencing 5 possible staging of coupling currents. Each circuit has its resistance R_j, its cross section square F_j, depending on the twist pitch l_{pj} and the radius r_j, and its inductance L_j given by the sum of auto and mutual inductances. If the field variation is $B_{ext}=\Delta B_m \cdot sin(2\pi ft)$ the current in each cable stage can be written as:

$$i_{kj} = \frac{F_j}{m_j R_j} \cdot \frac{\omega \cdot p_j}{\omega^2 + p_j^2} \cdot \Delta B_m \cdot \left(p_j \sin \omega t + \omega \cos \omega t\right) \tag{44}$$
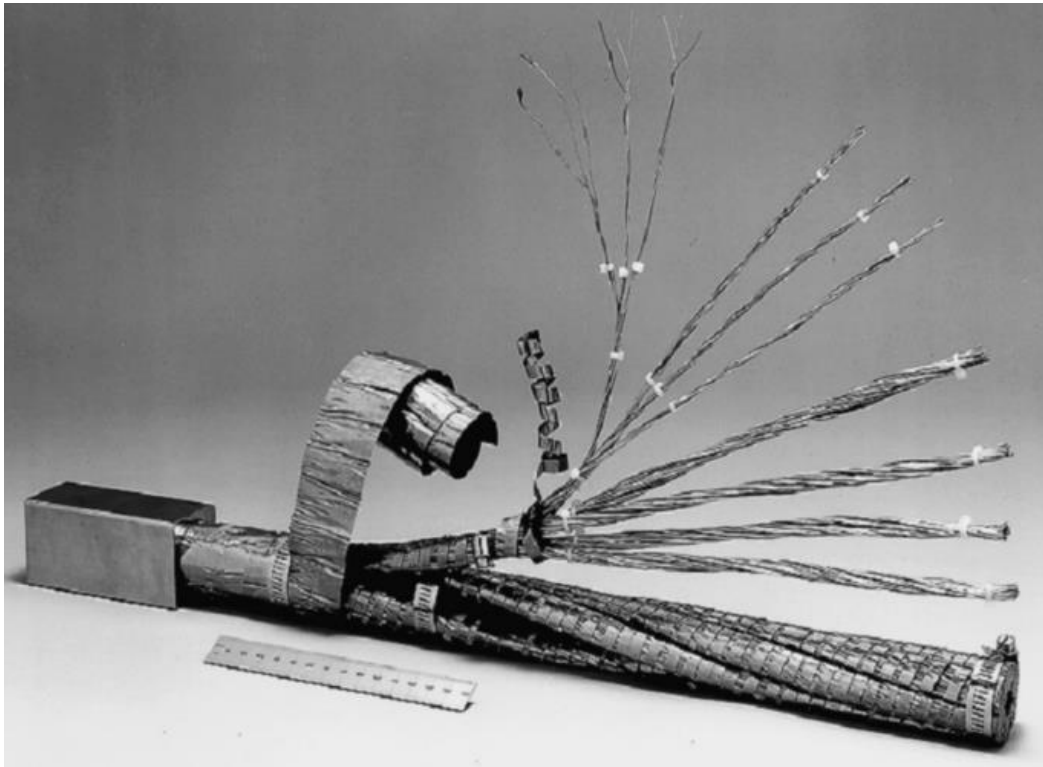

Fig. 18: View of the multistage cable layout of PF6 conductor [11].

The coupling currents can be added to or subtracted from the transport current flowing in the SC, that is simultaneously affected by a temperature increasing due to the coupling and eddy current losses: this means that the operating temperature margin of the cable can be increased (in case of opposite currents direction, a→b→d) or can be exceeded (summing coupling, eddy and transport currents, a→b→c) leading to the instability of the SC if the operating temperature exceeds the T_c value (Fig. 19). The additional current produced by the AC loss reaches its maximum value almost immediately after the temperature peak, in case of a varying background field with exponential decay [9]; induced currents decay during the heat transfert to the helium mass flow.
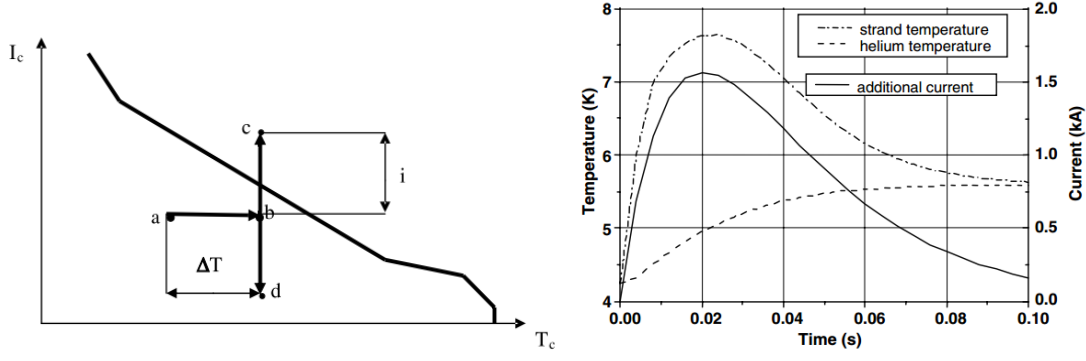
Fig. 19: Operative margin variation due to the additional current (left); temperature and current distributions due to a decaying magnetic field (right) [9].

The energy per cycle [J/cycle] generated in the conductor matrix piece with a full twist pitch length l_{pe}, equal to the last cabling stage (petal twist pitch) and twist radius r_e is:

$$E_c = 2\pi l_{pe}^2 r_e^2 \cdot \frac{\Delta B_m^2 \cdot R_e \cdot \omega}{R_e^2 + L_e^2 \omega^2} \tag{45}$$

Where p_c is the reciprocal of the coupling Electric Time Constant τ_c [s]:

$$\tau_c = R_e / L_e \tag{46}$$

The last stage resistance R_e is the sum of the matrix resistance R_m and the contact resistance R_c [$\Omega \cdot m^2$]:

$$R_c = \frac{V}{I} \cdot l \tag{47}$$

that appears when superconducting strands are subjected to the Lorentz force generated by the mechanical cycling on the conductor; this load compacts the cable elements one another along the contact length l changing material properties due to strands' micro-sliding and compressive strain. The contact resistance R_c plays a major role in the reducing of AC loss and permit a more uniform current redistribution between superconductive strands.

This has been demonstrated by A. Nihjus *et al.* [12] with experimental analysis on two NbTi CICCs with different strands (Ni-coated or with internal CuNi barrier) with the same staging layout but different final twist pitch (450 and 420 respectively), relevant for the PF coil of the ITER magnet system. The contact resistance reaches the maximum value within the first 10-100 EM cycles for the two samples, then decays at 10^6 cycles saturating at a constant value below the original contact resistance with null EM load.

The coupling loss increase with the frequency of the field variation and the analytic value of the coupling parameter $n\tau$, representing the initial slope of the AC loss curve, can be obtained from four different contributions:

$$n\tau = n\tau_{strand} + \frac{\beta_1}{R_{c1}} + 4\frac{\beta_2 l_{p2}^2 r_2^2}{R_{c2}} + 4\frac{\beta_3 l_{p3}^2 r_3^2}{R_{c3}} \tag{48}$$

where β is a fitting parameter for the time constant of the inter-strand, bundle and petal contact resistances, respectively R_{c1}, R_{c2} and R_{c3}. The initial single time constant $n\tau$ fits quite well the measured coupling loss at low background field frequencies but is not well representative of the high frequency regime where the contact resistance decreases.

A low AC loss value can be obtained increasing the sub-cable contact resistance with a stainless steel wrapping around the final twist stage, thus cutting down transvers current loops among the six petals [13]
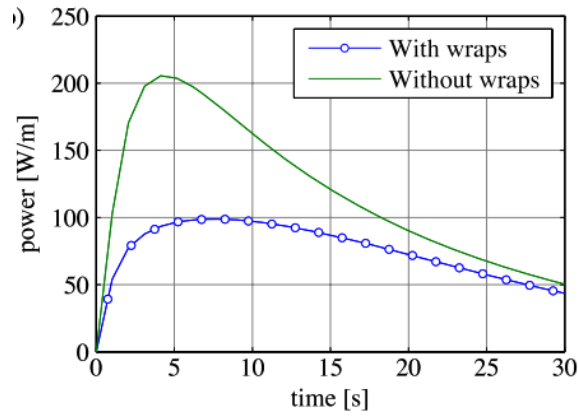

Fig. 20: Power dissipation versus time in a 1 m long TF CICC under a decaying background field [13].

The inter-filament transverse resistance R_{IF} of NbTi wires can be directly measured with a Four Probes voltage-current method [14] and is found to be 0.2-0.6·10^{-6} Ω at 4.2 K, increasing with the background magnetic field due to the magnetoresistance effect of the copper matrix [15]. Since R_{IF} is much higher than the resistivity of the stabilization copper matrix, the current density is higher in the matrix than in the filaments, thus proving that the filament-to-matrix contact resistance Rc (in the order of 10^{-14} Ω·m^2) is dominant with respect to the matrix resistance in the AC loss determination.

30

$$n\tau = n\tau_{strand} + \frac{\beta_1}{R_{c1}} + 4\frac{\beta_2 l_{p2}^2 r_2^2}{R_{c3}}$$

3.4.3. Eddy current losses

Eddy current losses E_{ec} are generated by screening currents that appear in conducting materials such as copper and stainless steel of the PF joint exposed to the varying magnetic field. In accordance with [9] eddy current losses per cycle induced by a sinusoidal field $B_{ext}=\Delta B_m \cdot sin(2\pi f t)$ in a hollow cylinder with external radius r_e and internal radius r_i can be determined as:

$$E_{ec} = \frac{\pi^2(r_e^2-r_i^2)l_{pe}}{4\rho_{Cu}} \cdot \frac{\Delta B_m^2 \omega^3}{p_{ec}^2+\omega^2} \tag{49}$$

where p_{ec} is the reciprocal of the eddy current Electric Time Constant τ_{ec} [s]:

$$\tau_{ec} = \frac{(r_e^2-r_i^2)\mu_0}{4\rho_{Cu}} \tag{50}$$

Eddy currents have negligible effects at low frequency, becoming consistent for applied field pulses with $f > 3$ Hz. The AC loss generated by current loops depends on the joint orientation: the major contribution to energy dissipation under a generic field ramp is found with the component perpendicular to the joint plane since the current loops are generated in the copper sole, that is the most resistive domain comparing with the cable in the joint. The inductive effects of the field ramp in parallel direction interest a smaller cross section thus inducing smallest loops and smallest eddy current losses. According to the stability criterion:

$$P = 2h \cdot p \cdot l \cdot (T_{cs} - T_{op}) \tag{51}$$

where h is the heat transfer coefficient [W/m²K] and p and l are the perimeter and the length of the superconductor respectively, a large peak power from AC losses can be tolerated at the joint, however a high peak power can cause a hot helium slug at the joint helium inlet, with the possibility of heat transfer towards the high field region in the conductor creating unacceptable thermal instabilities. For these reasons the temperature margin in the joint due to AC losses is set at 0.2 K, 10% of the design temperature margin of the conductor [16].

The total energy per cycle dissipated in the joint will be then:

$$E_{tot} = E_{AC} + E_m \tag{52}$$

where E_m is the mechanical loss associated with the plastic deformation of the cable within its jacket due to cyclic mechanical loading; this contribution saturates after the initial cycles [17] being negligible at low frequencies and independent from the magnetic pulse rate.

As reported in [18] the hysteresis loss is constant at low frequencies and can be subtracted from the AC loss measurements as an offset for the energy per cycle evaluation.
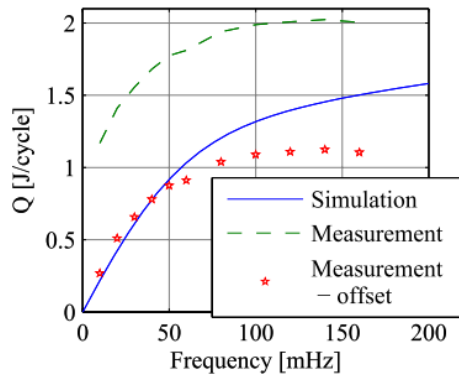

Fig. 21: Comparison between numerical results and experimental measurements, with and without offset, of a mock up joint [18].

If we consider a decaying magnetic field of $B(t) = B_0 e^{-\frac{t}{\tau_0}}$ with $B_0 = 1$ T, we found that the energy losses depend from the time constant τ_0: coupling losses have a negligible contribution in total losses in case of a magnetic field variation applied along the cable axis, whereas coupling loss and eddy current loss are comparable for transversal background field variations, as we can see in Fig. 22. The ratio between coupling current and eddy current losses depends on the matrix specific resistance and the time constant of the transversal background field variation, as is shown in Fig. 23.
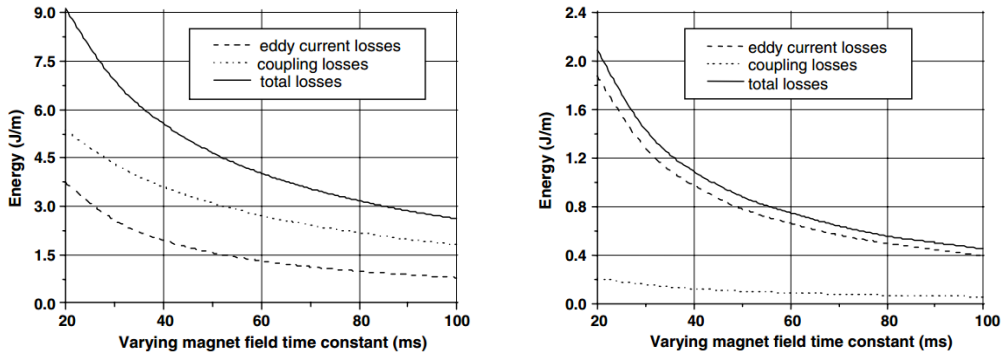

Fig. 22: AC loss contribution in function of background field variation time constant in case of (left) transvers and (right) parallel field [9].
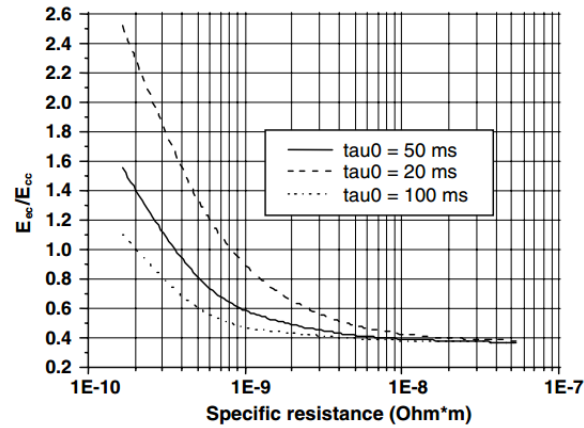
Fig. 23: Eddy current/coupling current loss ratio as function of the copper matrix resistivity and time constant of transvers magnetic field variation [9].

3.5. The SULTAN test facility

The SUpraLeiter Test ANlage (SULTAN) test facility at the Centre de Recherches en Physique des Plasma (CRPP) in Villigen, Swizerland (Fig. 24), is a unique tool to test superconducting components of the ITER magnet such as CICCs and joints over a broad range of operating conditions.

The SULTAN magnet system is composed by a split solenoid for the B_{DC} field and a split coil for the transversal pulsed B_{AC}; the superconducting magnets can operate with static field up to 12 T in cryogenic environment, with magnetic pulses up to 4 T with field ramps up to 65 T/s for the characterization of a sample (Fig. 25) made up by two short conductor length (up to 3 m), electrically insulated, connected at the bottom with a superconducting joint in the "praying hands" configuration and fed with transport currents up to 100 kA injected in the sample from the upper terminations. The operative positive curret from the left leg to the right leg of the sample generates a repulsive force F which displaces the superconducting strands in the cable toward the external region of the sample, whereas with the reverse current an actracting force is found between conductors, therefore the sample is compacted in a stainless steel clamping in order to withstand the high Lorentz forces without deformation of the sample. The characteristics of the strands, such as the critical current and the effective strain, are dependent from the electro-mechanical cycling load.

The High Field Zone of the SULTAN magnet system is found only in a restricted region of the solenoid bore and the maximum magnetic field is considered constant only in a 450 mm length; the joint can be tested under high field by lifting up the sample.

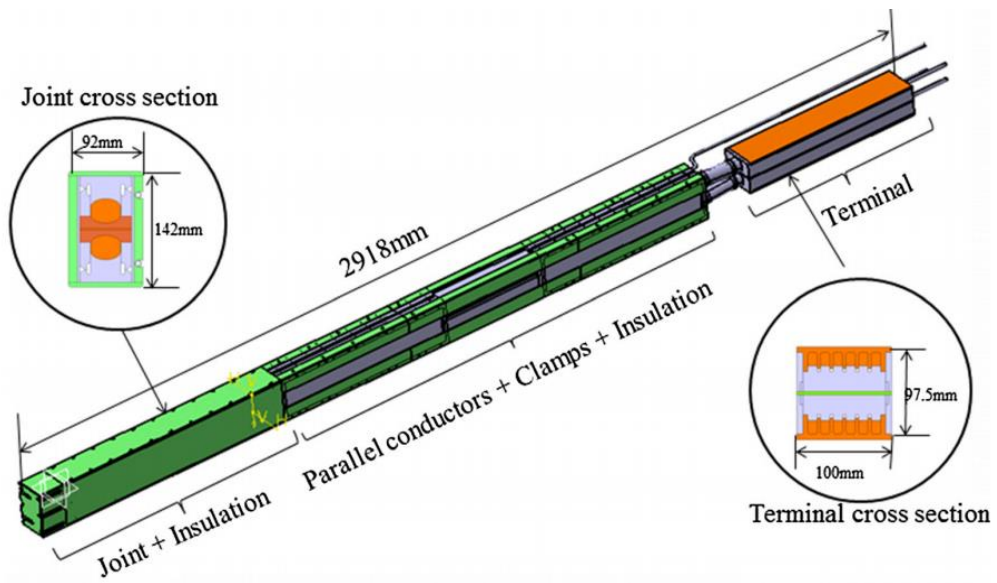Fig. 24: SULTAN facility with full size sample to be tested [19].

Fig. 25: Full size joint sample [20].

4. Poloidal Field Joints in the ITER Magnet System

4.1. Design and operating regime of PF coils

The ITER Poloidal Field (PF) magnet system is shown in Fig. 26: it consists of six PF coils, ranging in diameter from 8 m to 24 m, operating in pulsed regime to provide the position equilibrium of plasma current and the plasma vertical stability during the operating condition of the ITER tokamak.
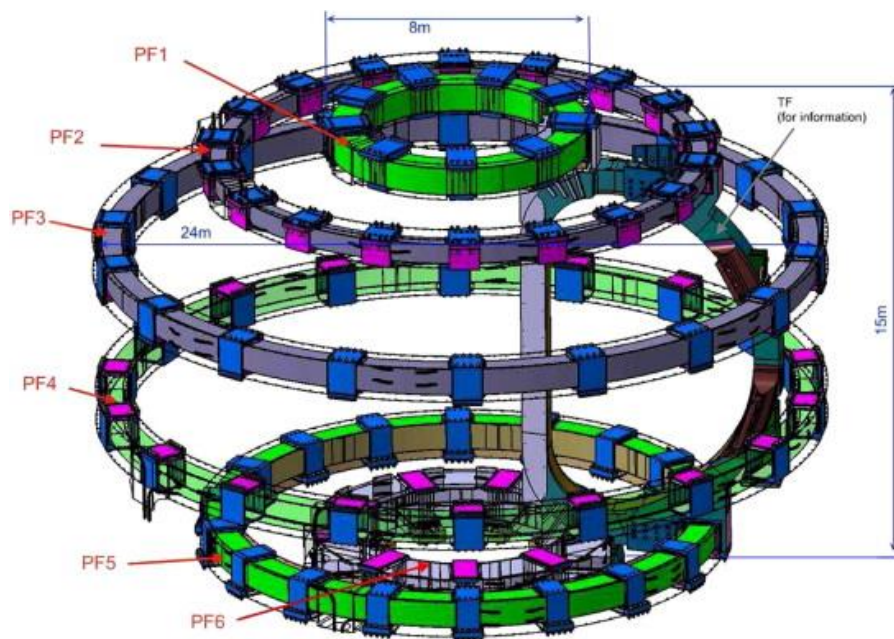

Fig. 26: The ITER Poloidal Field (PF) magnet system [21].

All PF coils are built by stacking 6 to 9 double-pancake (DP) windings wound with NbTi cable-in-conduit conductors (CICC) by two-in-hand winding scheme from "outside-in" to "inside-out". Two cables are connected in series with a pancake joint (PJ) and the double pancakes are connected by DP joints; all the joints are in the "shaking hands" configuration and are located at the outer radius of the coil to ensure a low magnetic load and maximize the temperature margin of such a critical component. The ends of the conductor of the top and the bottom pancake are the coil termination and are joined to the terminations of the superconducting bus bars of the feeders. The six PF coils are attached to the TF coil cases through flexible plates or sliding supports made of low friction material to allow spatial displacement of the coil due to the high Lorentz force in radial and axial direction. PF coil and DP layout are shown in Fig. 27 and the final design parameters of PF coils layout are given in Tab. 5.
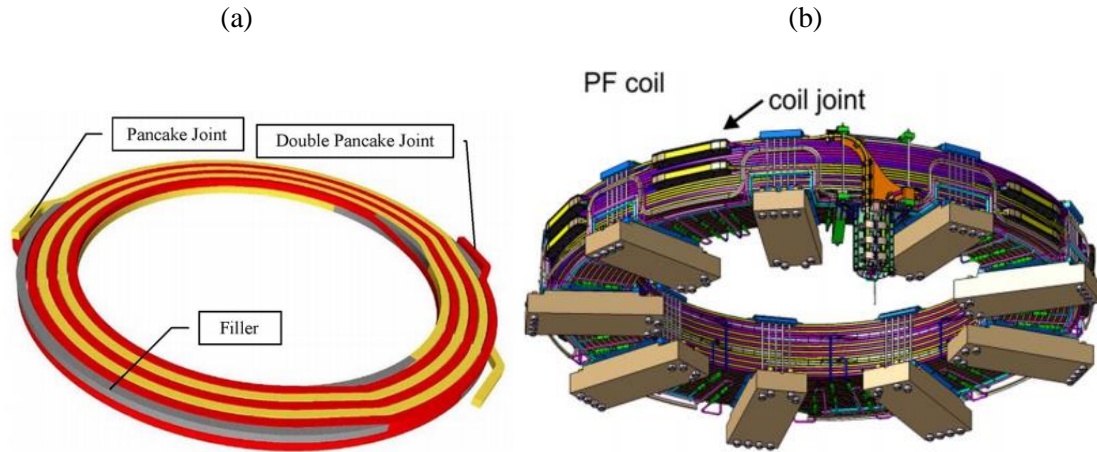
Fig. 27: (a) General sketch of PF Double Pancake [22] and (b) PF coil with joint positioning [23].

Coil	PF1	PF2~5	PF6
Maximum current (kA)	48	55(52 for PF 5)	48(52 for sub-cooling)
Bath temperature (K)	4.2	4.2	4.2(3.8 for sub-cooling)
Peak magnetic field (T)	6.4	4.8(5.7 for PF5)	6.4(6.8 for sub-cooling)
Maximum operating terminal voltage (including fast discharge, kV)	10	14	10
Turn-to-turn (radial) maximum operating voltage (kV)	0.63	1.17	0.56
Maximum terminal voltage (kV) in faulted operation	28	28	28
Maximum test DC Voltage (kV) Ground to Terminal	29	29	29

Tab. 5: Design operative parameters of PF coils [24].

The stacked DP design allows for easy bypassing of a pancake with a superconducting jumper bus in case of failure to avoid a major disassembly of the tokamak in order to extract a PF coil and repair a failed DP: in this case the total number of turns decreases, so as the Ampere-turns in the coil, therefore two ways for ensuring the operating current are proposed: increasing the operating current and/or decreasing its operation temperature by 0.3-0.4 K [25]. PF6 and PF5 are located at the bottom of the tokamak, therefore are the first coil assembled in the machine.

PF1 and PF6 are the most loaded coils and their conductor design has been especially selected to be more stable and powerful than the other larger coils: the PF1&6 NbTi strands characteristics (Fig. 28) and cabling layout (Fig. 29) are given in Tab. 6 and Tab. 7 respectively.
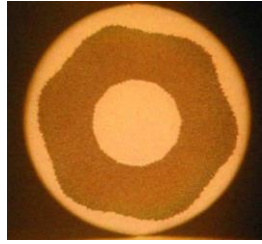
Fig. 28: Section view of a NbTi strand for PF1&6 coil (left) [26].

Characteristics	ITER specification	Average values during production
Outer diameter (mm)	0.730 ± 0.003	0.730
Cu/non-Cu ratio	1.60 ± 0.05	1.64
Filament diameter (μm)	≤ 8.0	6.7
Distance between the filaments (μm)	≥ 1.0	1.1
Critical current at 4.2 K,6.4 T (A)	≥ 306.0	324.8
n-value	> 20.0	40.1
RRR	≥ 100	130

Tab. 6: Design characteristics of NbTi strands for PF1&6 coil (right); comparison between ITER specifications and average value during the production phase [26].
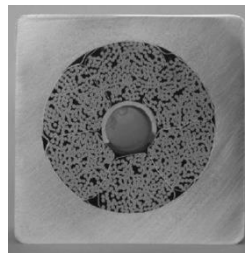

Fig. 29: Section view of a NbTi CICC for PF6 coil (left) [1].

Cabling layout	3 sc x 4 x 4 x 5 x 6
Twist direction	Right hand
Cable twist pitches	45/85/145/250/450 mm
Sub-cable and cable wrap thickness	0.05 and 0.1 mm
Central spiral OD/ID	12/10 mm
Spiral and wraps material	304L or 316 L
Jacket material	316 L
Final conductor outer dimension	53.8 mm

Tab. 7: Design cabling layout for PF6 NbTi CICC (right) [1].

PF coils are produced by EU and RF domestic agencies (DA) under ITER organization (IO) guidelines [27]; after the final rearrangements of PF coils design, PF conductors layout and updating of several coil components in 2009 [28], the manufacturing phase started in 2011 in the separates DAs but the design and validation of some critical items, such as helium inlets, joints and termination supports, is still ongoing. Because of their enormous dimensions, PF coils are manufactured and assembled in a dedicated facility built up in 2010 next to the ITER construction site: the PF coils production process is shown in Fig. 30.
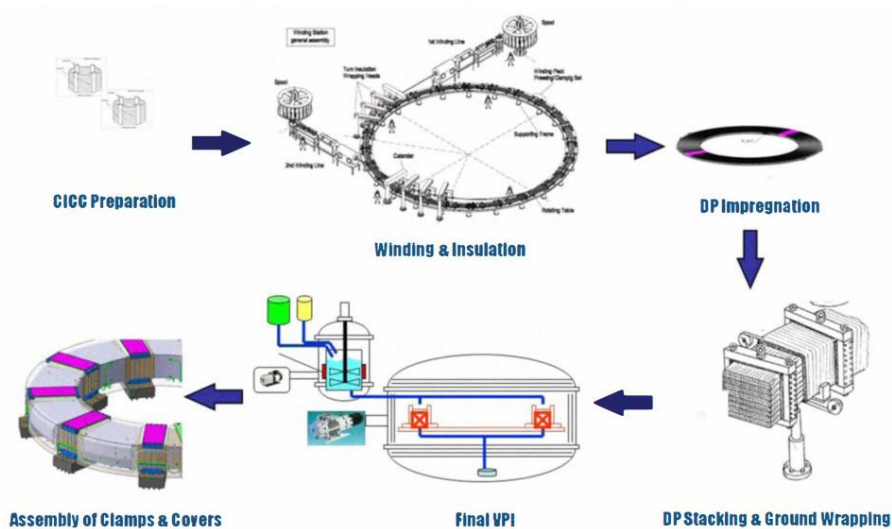
Fig. 30: In site production process of the ITER PF coils.

4.2. Development of superconducting joints design

One of the purposes of the Engineering Design Activity (EDA) for ITER is to develop, manufacture and test joints to be used as electrical connection for superconducting cables of ITER coils. A R&D task has been launched in 1993 and four ITER parties, that are Japan (JA), European Union (EU), United States (US) and Russian Federation (RF), are involved. After theoretical and experimental works [29-30] the European Union proposed a specific design of superconducting joints for TF and CS coils [31]. After a set of common design and manufacturing criteria has been chosen, according to the ITER Joint Central Team (JCT) recommendations, a series of sub-size joint samples is built in laboratory considering variations of layout parameters for the investigation of the best fabrication techniques; analysis campaigns have been carried out in laboratory for the electrical, thermo-hydraulic and mechanical characterization of these lab-scale samples. The last stage of the R&D task is to realize full-size joint samples to be tested in the PTF [32] and SULTAN test facility to verify that all components respect the ITER specification for a safe and controlled operating regime of the whole machine.

Joints are necessary to electrically connect two Cable-In-Conduit Conductors (CICCs) unit lengths, ensuring current transfer in the whole coil between the two terminals. Because of their limited length, wounded cables must be connected in series according to the lap-type concept using a low resistive copper in between, with an overlapping length equal to the last stage cabling twist pitch (400-500 mm). Two possible configurations, shown in Fig. 31, can be considered for the cable junction in the joint: the "praying hands" configuration (PHC) and the "shaking hands" configuration (SHC), depending on the coil geometry and space constraining.
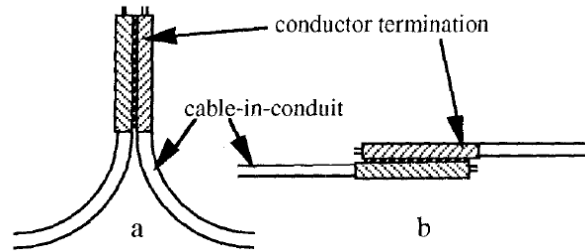
Fig. 31: Different cable junctions: (a) "praying hands" configuration and (b) "shaking hads" configuration [16].

As a general indication, the conductor design should not be driven by the joint performances: electrical connection must ensure a stable and safe operating conditions since a failure of a joint (leak of helium, short circuit, mechanical stresses) may lead to the conductor quench producing thermal instability in the whole machine. After the activation of ITER tokamak there will be no possibility to access or repair any component of the superconducting coil so the joint design must withstand the operating loads with adequate margin without affecting the connected cables by extra thermal loads. The main joint requirement is then a low resistance limiting ohmic loss generated by very high currents up to 68 kA. Low resistive material can be affected by high inductive effects during background magnetic field variations thus generating unacceptable eddy current leading to high AC losses.

Due to limitations of PF coil tests prior to the ITER tokamak assembly, joints design and manufacturing process must be qualified and validated. The stainless-steel full-size joint sample SS-FSJS is the first joint design [31] proposed by EU for both CS and TF in 1995 and finally fabricated in 1998. The cable is composed of 1152 twisted Nb_3Sn strands of 0.8 mm in diameter with internal tin produced by Europa Metalli (Italy); no pure copper strands are present in the bundle. The cable (38.7 mm in diameter) is divided into six sub-cables (petals) around a central stainless steel spiral for the cooling helium flow (outer diameter of 12 mm and 2 mm thick) and inserted in a stainless steel square jacket with outer size of 51 mm, with a cable local void fraction of 36.1% and a final stage twist pitch of 440 mm. The joint is made according to the "twin-box" concept proposed by CEA, consisting in two independent lap termination, each one inserted in a bimetallic box machined in a pre-bended copper-steel plate welded by explosion (Fig. 32): the electrical connection is ensured by the soldering of the two flat contact surfaces of the copper soles.
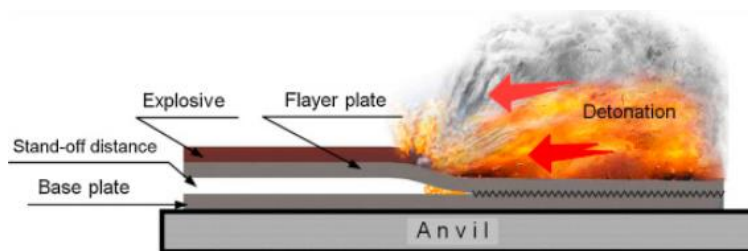

Fig. 32: Sketch of the explosive welding technique for the bimetallic box manufacturing [33].

This peculiar design allows for easy preparation and assembly of the joint, easy dismantling and reconnection of the joint as a component of ITER coils and ensure an independent cooling circuit for the joint. The joint is manufactured in three phases:

- At each cable end the jacket is removed over a length of 500 mm and sub-cable wrapping are removed only in their periphery, whereas they are preserved between petals to reduce pulsed field losses. The chrome plating is mechanically removed from the strands by jet abrasion using glass beads to increase the active contact surface performances, The cable is inserted in the bimetallic box and compacted by a stainless steel cover to reach a local cable void fraction of 20-30% inside the joint; the cover is finally welded to the box, which is welded to the jacket of the conductor end. A leak test is performed.

- The heat treatment of the Nb_3Sn CICC is operated in argon atmosphere (1.1 bar and 0.4 l/min) following four steps: 100 h at 210 °C, 24 h at 340 °C, 50 h at 450 °C and 200 h at 650 °C [34].

- The compacting tool is removed and the copper sole surface is cleaned, deoxidized and machined to make the active contact surface as flat as possible. The two copper surfaces are tined and the two bimetallic boxes are tightened together and heated in order to realize the PbSn soft soldering in between thus eventually connect the two conductor bars in the PHC.

Sub-size joint samples (EU-B1/2/3/4 and EU-SBx/y) have been manufactured to be as much as possible relevant to a full-size joint to carry out a characterization of the joint varying parameters such as copper *RRR*, void fraction and field direction [16]. This low-scale joints connect two sub-sized CICCs with six twisted sub-cables are pressed in a stainless steel square jackets with a final outer size of 13.8 mm made with 144 twisted Nb_3Sn strands with a 2 µm thick chrome plating; the last stage twist pitch is reduced up to 160 mm.

The Japanese sub-size joint samples (JA-25/30) have been tested for results comparison considering different layout of the cable (192 strands with a final twist pitch of 300 mm in a round jacket) and geometry of the joint (round jacket connected to a round copper sleeve and a copper saddle with CuNi barriers). Sketches of both kind of joint are shown in Fig. 33 and samples characteristics are listed in Tab. 8.
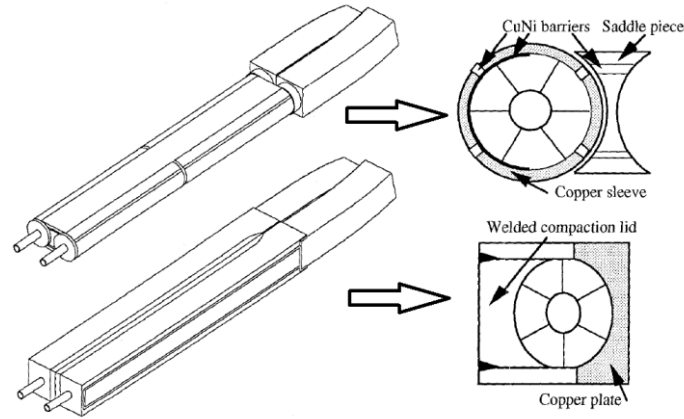
40

Fig. 33: Schematic view of Japanese sample with round joint section on a copper saddle (top) and European sample with square joint section on a copper plate (bottom) [16].

RESISTANCE RESULTS @ 2 T, 4.2 K FOR SUBSIZE JOINTS

Sample identity	Copper RRR	Cable void fraction	Bundle-Cu resistance $(p\Omega m^2)$	Joint resistance $(n\Omega)$
JA- 25	200	25%	6.3	5.0
JA - 30	200	30%	14.3	8.3
EU - B1/B4	320	20%	5.4 / 1.8	5.3 / 2.1
EU - B2	320	30%	8.3	8.0
EU - B3	5	20%	3.2	11.6
EU - SBx/SBy*	320	20%	2.1 / 1.9	2.1 / 1.9

* measured at 6 K

Tab. 8: Results of electric resistance measurements on Japanese and European sub-size joint samples [16].

DC resistance evaluation with voltmetric is operated with currents up to 3.5 kA under a background field of 2 T. Measurements confirm the order of magnitude of joint resistance $(2\sim6\cdot10^{-9}\ \Omega)$ predicted by theoretical models; therefore a scattering in DC resistance measurement is found in samples with the same parameters, thus proving that the joint performance is not perfectly predictable and the effective machining and manufacturing operations can induce substantial differences in the behavior of joints with identical designs. The scaling from sub-size to full-size joint samples depends on the transfer resistance R_s [$\Omega\cdot m^2$] between superconducting strands and the copper surface, considering all the contact resistances in between such as the intra-strand resistance and the strand-to-sole contact resistance. R_s is derived multiplying the difference between overall joint resistance and bulk metal resistance by the contact surface of the cable with the copper sole: the design value of joint resistance can be achieved maintaining $R_s < 10^{-11}\ \Omega\cdot m^2$.

AC losses are measured both with magnetization technique and calorimetric method, subjecting the joint to background field ramps up to 2 T/s: results show that the energy losses for a standard cycle (ΔB=1.2 T, dB/dt = 0.1 T/s) remains in the range of 1-10 J, with a time constant $n\tau < 2$ s and the full-size joint dissipation can be obtained scaling measured values with the copper volume and the square of the copper width.

The SS-FSJS is realized making use of the CS conductor developed by EU for ITER model coils and it is relevant to the inner joints of the Toroidal Field Model Coil (TFMC). The sample is tested after a classical heat treatment for Nb_3Sn followed by 13 thermal cycles from room temperature to 78 K: no significant deformations and helium leak have been detected at the end of both thermal loading, thus proving the feasibility and reliability of the sample to be tested in the SULTAN facility. The measured resistance of a full-size joint sample with round terminations is 6 nΩ: even if comparable with sub-size joint resistance, this value is yet too high and it is probably due to the lack of experience in manufacturing.

After the ITER JCA meeting held in Boston (11/1995) few modifications in dimensions and instrumentations layout of the full-size joint sample have been introduced; preliminary trials have been performed by Ansaldo on mock-ups in order to qualify the updated manufacturing process and ensure both mechanical stress and dimensions of the sample to be tested in the SULTAN facility [34]. The two conductor legs are electrically connected at the bottom by a lap-type termination in which two bimetallic boxes are soldered with a copper wedge in between; upper terminations have been realized following the same "twin-box" concept for the connection to the facility transformer. Specific adjustments of the manufacturing process are necessary to compensate the undesired deformation and misalignment of the two conductor bars during heat treatment and soldering phase.

Within the TFMC project two more full-size joint sample are developed following the same design of that proposed by EU (two conductors connected in the PHC with a "twin-box" lap termination): the TFMC-FSJS, relevant to the TFMC outer joints, and the TF-FSJS, relevant to the final design of ITER TF coil. Both samples have the same cable layout (720 Nb_3Sn and 360 pure copper strands, with cable diameter reduced up to 37.5 mm) in a round jacket, but differ in material and dimension (326LN stainless steel with outer diameter of 40.7 mm or Incoloy 908 with outer diameter of 39.5 mm) of the jacket and in the joint contact interface manufacturing (electron beam welding with copper pins for the TFMC-FSJS and PbSn soft soldering for the TF-FSJS).

These three full-size joints were fabricated in the industries after a preliminary R&D work for the development or upgrading of the industrial facilities in order to qualify the fabrication process. Samples characteristics are reported in Tab. 9.

As reported in [36-37] satisfying results have been reached in terms of manufacturing and performances of both joints and conductors, proving that this technology was ready to be available for the real ITER coils. All the three FSJS show a low energy loss value during AC pulses at different frequencies and an acceptable electric resistance, linearly increasing with the background magnetic field up to 11 T and transport current up to 80 kA, as shown in Fig. 34.

	SS-FSJS	TFMC-FSJS	TF-FSJS
Conductor			
Number of Nb$_3$Sn strands	1152	720	720
Number of pure copper strands	0	360	360
Cable twist pitch (mm)	440	440	440
Central spiral (mm)	10×12	10×12	10×12
Cable diameter (mm)	38.7	37.5	37.5
Jacket shape, outer size (mm)	Square, 51	Circular, 40.7	Circular, 39.5
Jacket material	316LN	316LN	Incoloy 908
Joint			
Joint box material	316LN–copper	316LN–copper	Incoloy–copper
Joint interface	Tapered wedge	Copper pins	None
Jointing technique	PbSn solder	Electron beam weld	PbSn solder

Tab. 9: Conductor and joint characteristics of three full-size joint samples [35].

It can be notice that the difference in initial resistance (with $B = 0$ T) between SS and TFMC FSJSs is two times higher than that expected from tests on sub-size joint, probably because of the degradation of contact between the strands and the copper sole during the electron beam welding process.

The joints operate at their theoretical current sharing temperature T_{cs} with only slight increase of electric resistance; the conductors are tested and a good agreement of the evolution of critical current with both temperature and transport current has been observed between experimental and theoretical analysis.
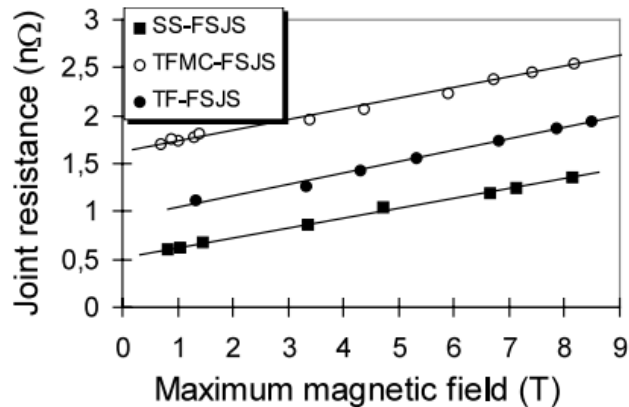

Fig. 34: Joint resistance of three full-size joint samples as a function of background magnetic field [37].

A clear influence of the joint on the conductor critical current measurements is due to the vicinity of the connection to the high field zone, determining current transfer and current redistribution among strands: since the joints are placed in low-field region in the ITER coils to reduce its electromagnetic load, those results cannot be extrapolated to a real ITER coil.

Starting from the reliable overlap joint concept proposed by CEA and successfully tested for three FSJSs relevant to TF and CS coils, the "twin-box" design has been adopted for the PF joints [38]. The terminations of two NbTi cables with six petals in square stainless steel jackets are compacted in two bimetallic boxes, soldered in the SHC with PbSn through the copper active contact surface to allow the electrical connection. The central spiral for helium mass flow in the cable is replaced with a rigid tube inside the joint and a local void fraction of 25% is achieved by pressing and soldering the steel cover. After a preliminary metallic brushing of the Ni coated strands, cable-to-sole contact surface is silver coated to decrease contact resistance.

To gain experience on these conductor and joints, two sub-size joint samples have been tested in the Joint Sub-size Experimental Facility (JOSEFA) located at CEA/Cadarache (France) [39] for the measurements of DC resistance up to 10 kA and AC losses under trapezoidal pulse with fast and slow field ramps along cable axis [40]. These tests are operated considering two cables with different strands type, divided in six sub-cables with the same twisting pattern (108 strands 3x3x3x4). PF1-SSJS is made with external Ni plated strands, whereas PF2-SSJS is made with strands with internal CuNi barrier; the respective measured resistance at 2 T are 8.1 nΩ and 3.5 nΩ. This result is opposite to the expectation because the removal of the Ni coating should have led to a decreasing of the joint resistance. Further investigation showed that this high resistance is related to the Ni coating removal procedure or to the silver-plating method. The magnetoresistance is two times higher in PF1 (0.6 nΩ) then in PF2 (0.3 nΩ) and a strong degradation of the sample can make it more sensitive to the high field, thus resulting in a higher resistance. The scaling of result at a full-size joint sample depends on the ratio between contact area: since $R_{SS}/R_{FS} = 8$ an electric resistance of 1 nΩ and 0.4 nΩ of the FSJS can be expected, remaining in the range of the minimum requirements for PF joints (2 nΩ at 2 T and 48 kA). The AC tests on sub-size joints samples show no significant influence by the maximum field in AC losses, that are substantially dependent from the temperature. When field ramp exceeds 0.15-0.2 T/s rapid magnetic instabilities occurs: they are induced by the saturation of the current loops crossing through the joint and their relaxation leads to a decreasing of the energy loss per cycle (J/cycle), as shown in Fig. 35. The main contribution in losses with longitudinal field pulses comes from the inter-cable current loop closing through the joint plane; experimental results are in good agreement with the previous analysis of the electrical resistance.
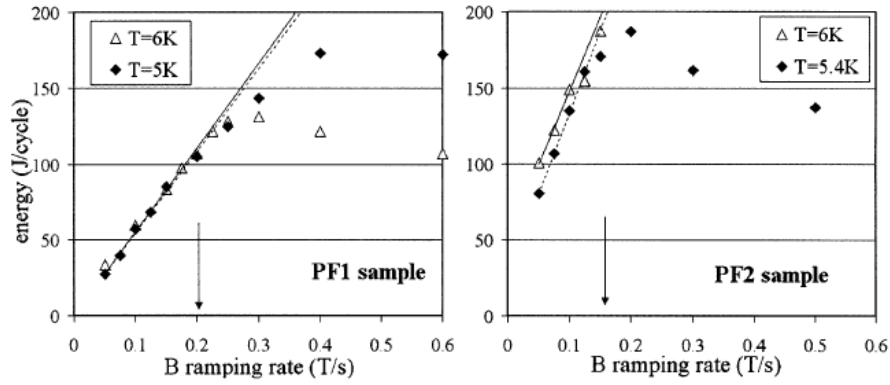
Fig. 35: Energy loss per cycle as function of magnetic field rate for PF1-SSJS (left) and PF2-SSJS (right); after a first linear increasing the current loops saturate and dissipations decrease for higher frequencies [40].

The first NbTi full-size joint sample for ITER PF coils (PF-FSJS) is manufactured and tested in the SULTAN facility in relevant operating conditions [41, 42]. The two conductor legs are similar to those previously considered, differing only in the type of strand (Ni coated made by Alstom or with CuNi internal barrier made by Europa Metalli), in the Cu/non Cu ratio in the strand matrix (1.54 and 1.9 respectively) and in the final stage cable twist pitch (395 or 410). A comparison between the two types of strands is shown in Fig. 36. and in Tab. 10.
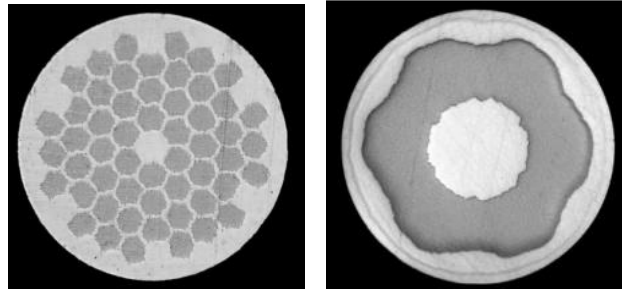

Fig. 36: Section view of NbTi strands made by Alstom (left) and Europa Metalli (right) for the PF-FSJS [42].

Strand manufacturer	Alstom	Europa Metalli
Strand o.d. (mm)	0.81	0.81
Cu/non Cu	1.54	1.9
Strand barrier	Int. Cu–Ni	Ni coating
Cable pattern	$3 \times 4 \times 4 \times 4 \times 6$	$3 \times 4 \times 4 \times 4 \times 6$
Nb–Sc strand	1152	1152
Nb–Cu strand	0	0
Cable o.d. (mm)	38.7	38.7
Spiral i.d. × o.d. (mm)	10×12	10×12
Last stage pitch (mm)	395	410
Conductor external dimensions (mm)	51×51	51×51
Jacket material	AISI 316LN	AISI 316LN

Tab. 10: PF-FSJS strands characteristics [41].

45

The main difference between the full-scale concept based on the SS-FSJS is the position of the TIG welding, located at the lateral surface of the bimetallic box, thus transferring the mechanical load from the conductor to the steel clamping system without crossing the weld, as shown in Fig. 37. The machining and the assembly of the termination have been updated: the stainless steel box is chamfered for the joint clamping and the copper soles are tinned with electrolytic process, silver coated and soldered by pressing the 0.3 mm thick 40/60 tin/lead at 210°C to create the electrical connection.
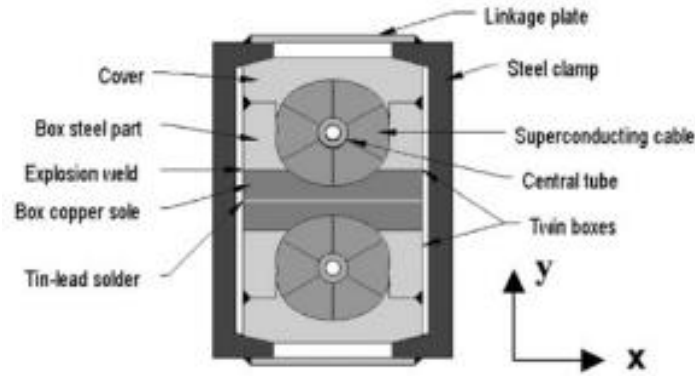

Fig. 37: Schematic view of PF-FSJS cross section [42].

The measured joint DC resistance is given as a linear function of the SULTAN magnetic field, independent of current up to 60 kA at 4.5 K, ranging from 1.1 nΩ at 0 T to 2.2 at 10 T, thus remaining below the reference maximum value of 2 nΩ under operating condition; the voltmetric measurements has been confirmed by the calorimetric method. The voltage drop is much more uniform in the right half joint (CuNi barrier) but is higher in the left half joint (Ni coated), since mechanical brushing method cannot ensure a uniform removal of Ni barrier, thus resulting in a DC resistance value that is higher than expected. The experimental value of AC losses under sine pulse is compared with the numerical model based on [38] showing a good fit at low frequency, with a peak at 0.2 Hz in all the simulation regarding critical operating conditions of the joint in ITER PF coils (plasma ignition, operating regime and plasma disruption).
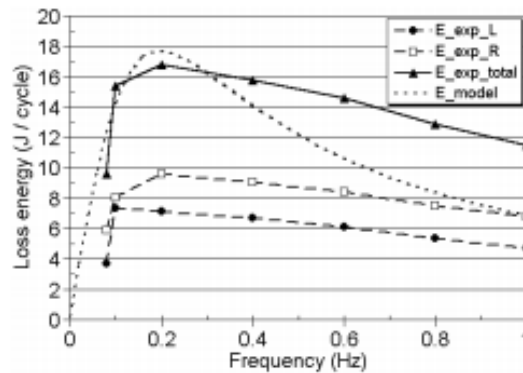

Fig. 38: Comparison between experimental and numerical results of AC loss analysis of the PF-FSJS [42].

Russian Federation has gained experience in technology and tooling to manufacture low-resistive electrical joints, especially regarding PF1 and PF6 coils, that are the most demanding in terms of stability margin and electromagnetic loads during their operating conditions in the ITER magnet system. They develop a reliable machining process for the preparation of mock-up joints to be tested [43] obtaining an electrical resistance of 1.92 nΩ with current up to 20 kA.

In 2015 the Institute of Plasma Physics in the Chinese Academy of Science (ASIPP) has develop a full-size joint sample that is relevant to the final design of the PF6 DP joint. A dummy joint was fabricated to verify the manufacturing process whereas the FSJS (Fig. 25) has been tested in order to qualify its electromechanical performances in the SULTAN test facility. An exhaustive description of the ASIPP-FSJS can be found in [20]. The electromagnetic load on the stainless steel clamps at the conductor section under a transport current of 55 kA with a background field of 2 T at 4.2 K is measured, showing that the self-field provided by the driving current generates a negligible repulsive force in the conductors, that is mainly due to the external magnetic field applied in the joint region.

4.3. Final design of the PF6 DP joint

After almost 20 years of R&D works a qualification program of lap joints for ITER coils has been developed by Y. Ilyin *et al*. [44, 45]. Several mock-ups have been produced according to the final design of TF, CS, CC, CB, MB and PF joints (Fig. 39) in order to establish robust manufacturing procedure during the qualification phase; the differences between joint designs arise from functional requirements and experience on manufacturing a specific type of conductor coil. Design parameters and manufacturers of ITER lap joints are shown in Tab. 11 and Tab. 12.
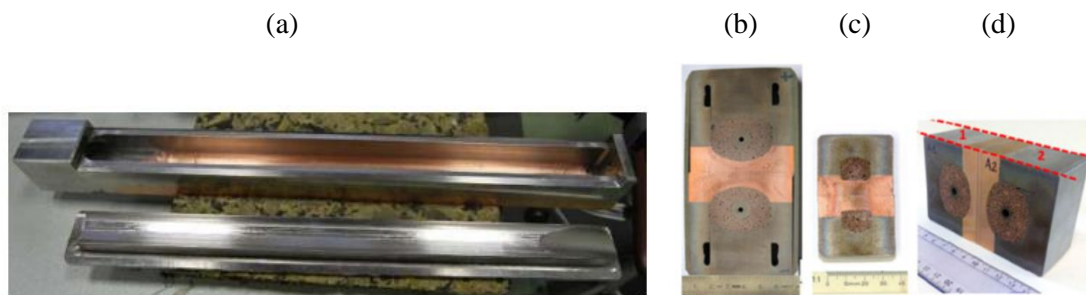

Fig. 39: (a) Manufactured PF/MB joint; cross sections of the assembled (b) PF/MB, (c) CC and (d) TF/CS joint mock-ups [45].

The ITER magnet system comprises hundreds of electrical lap joints interconnecting superconducting cables both in the SHC and the PHC; they cannot be tested once that the assembled coils are placed in the cryostat of the machine, hence a periodic test program for the joint in parallel with the coil fabrication is foreseen to control the reproducibility of the joint electrical performances. The objective of the qualification program aims at demonstrating that the manufacturing procedures, operators, tools and quality system are mature to minimize the production risks and guarantee successful performances of the component.

	PF	Feeder MB/CB	CC	TF	CS
Void fraction, %	19 ± 1	21 ± 1	22 ± 1	21 ± 1	22 ± 1
Ni/Cr removal method	brush/PF6 reverse plating	Reverse plating	brush	brush	brush
Box annealing prior to use	no	no	no	4 h at 400 C	no
SS wraps btw petals	preserved	n/a	n/a	removed	preserved
Outermost strands plating	pure tin	Silver	Silver	no	no
Cu sole inner side plating	pure tin	silver + In tinned	Silver	no	no
Cable-sole interface	soldered Sn96Ag4	pressed	Pressed	pressed, sintered	pressed, sintered
Box-box interface	soldered Pb60Sn40 (In wires to feeder)	pressed, In wires	pressed, In wires	soldered Pb60Sn40 (In wires to feeder)	pressed, In wires
Central pipe id/od, mm	3/12	MB: n/a CB: 3/6	n/a	6/10	3.5/9
Sole RRR at 0 T, after bonding and HT (CS/TF)	5 ÷ 6 Copper C12200	70 ÷ 100 Copper C10200/ C12200	70 ÷ 100 Copper C10200	450 ÷ 500 Copper C10100/ C10200	170 ÷ 230 Copper C10200
Jacket-box/ cover-box welds	FP/FP	MB: FPB, CB: FT/FPB	FPB/PP	FT/PP	FT/ PP
Joint clamps, connected by	side plates, weld	brackets, weld	brackets, weld	brackets, weld	brackets, weld

The flat side of the copper sole is either electroplated (PF) or hot tinned (TF) with Pb60Sn40 prior to soldering. All terminal boxes are silver plated on the flat side. The feeder boxes for the TF and CS terminals will be with copper C12200. The TF EU coil boxes will be with copper C10200. PP is partial penetration weld, FPB – full penetration butt weld, FT – fillet weld.

Tab. 11: Design parameters of ITER lap joints [45].

Coil	Copper	316L/LN Stainless steel	Cladding
PF1	MKM, GmbH, Germany	Forgiatura Morandini Srl, Italy	"Energometall", Russia
PF2–5	KME Germany AG & Co KG	Fomas Group, Italy	High Energy Metals, USA
MB/CC/PF6	Aurubis, Finland	Guizhou Aerospace Xinli Forging & Casting, China	Nanjing LeiHui New Material China
TF EU	Aurubis, Finland	316L, Outokumpu Stainless AB, Sweden	High Energy Metals, USA
TF JA	Mitsubishi Shindoh, Japan	316LN, Daido Steel Co. Ltd., Japan	Asahi Kasei Corp., Japan
CS	CSN Carl Schreiber, Germany	VDM Metals GmbH, Germany	Nobelclad, France

Tab. 12: Manufacturers of materials for joint bimetallic boxes [45].

The qualification items concern materials, strands-copper and box-box interfaces and welds; mock-ups and full-size joint samples are tested in suppliers' facilities for the evaluation of mechanical loads and the reliability of fabrication techniques with fatigue tests at 77 K. Each coil supplier manufactured at least one qualification full-size joint to be tested in the SULTAN facility to verify the electrical performances of the joint. The acceptance criteria for DC resistance in the qualification program depend on the type of conductor:

- TF: 3 nΩ at 68 kA and 2 T

- CS: 4 nΩ at 45 kA and 4 T

- MB: 2 nΩ at 70 kA and 0 T

- CC/CB: 5 nΩ at 10 kA and 2.5 T

- PF: 5 nΩ at 55 kA and 3 T

As we can see in Fig. 40 the PF joints are intentionally [46, 47] the most resistive ones, with the calculated copper contribution to resistance of 70-80%; the low *RRR* value (6-100) of copper in PF joints ensure a low influence from the applied magnetic field and variation of resistance with the transport current is negligible for all joints. All the tested joints relative to the PF coil respect the limit value of 5 nΩ after all the mechanical and thermal cycling loads.
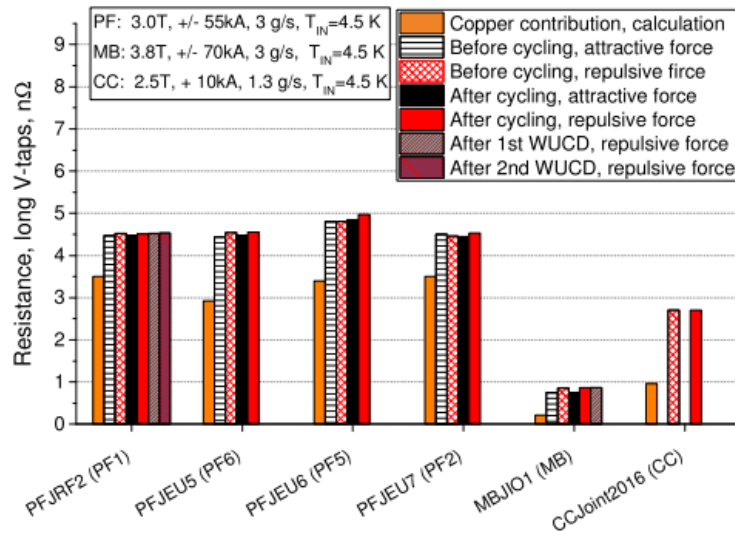

Fig. 40: Resistance of the NbTi joints tested in the SULTAN facility [45].

The coupling losses per volume per cycle (J/cm^3·cycle) measured for a few joint samples, differing in the number of NbTi strands of the conductors, are compared with numerical results in Fig. 41 and several considerations can be done. The increasing of copper *RRR* leads to a decreasing of the time constant *nτ* (see PF loss profile with *RRR* = 6 versus TF/MB with *RRR* = 100-500); the contribution of well compacted cable to the loss is not negligible and leads to bigger *nτ* and earlier saturation of the loss curve in the PF joints compared to the predicted value of 0.15 s [46].

Even if AC losses are higher than expected in all PF joints, no quench is detected in case of the plasma ignition scenario, corresponding to a 55 W peak power and total 70 J energy released in the joint.
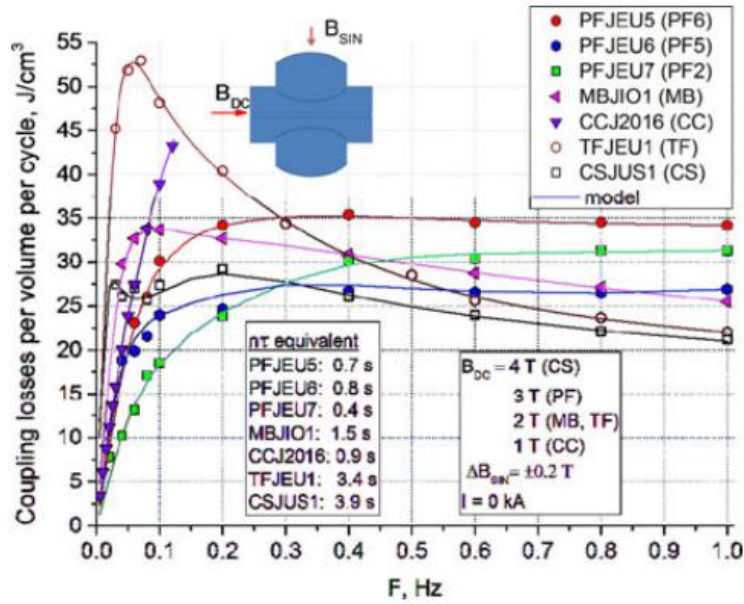
Fig. 41: Energy loss per unit volume per cycle under sinusoidal field pulse of 0.2 T [45].

The stability run considers a trapezoidal field pulse of 0.4 T/s ramp followed by a plateau at 6 K, with a background field of 3 T and transport current of 55 kA in the sample. The quench of the conductor occurs only if the current sharing temperature T_{cs} is reached in the region of the termination: despite only the 50-60% of the strands are in contact with the copper sole, this result proves the good quality of the final joint design and the manufacturing process, ensuring a good stability and current sharing of the PF joints. Prequalification samples have been manufactured considering different geometries and *RRR* of the copper soles and the copper shim: the electrical analysis aimed at confirming the role of copper resistance in AC losses [48]. The PF1 qualification joint manufactured by Russian Federation shows an acceptable DC resistance in the range of 4.6 nΩ in the joint, confirmed by the calorimetric measurements at 55 kA: since the temperature margin is found to be 2.5 K in the PF1 operating condition, the QA documentation has been issued by the NIIEFA test facility and approved by the IO, so that the manufacturing of PF joints can finally begin [44].

50

5. Experimental Analysis of PFJEU1 SULTAN Sample

5.1. Experimental setup

The PFJEU1 sample (Fig. 42) is relevant to the PF6 coil and it is representative of the double pancake (DP) joint, located outside the coil in the "normal direction", with the joint plane parallel to the conductor winding and assembled in the SHC. This full-size joint sample has been tested in the SULTAN facility in October 2016 and measurements of dimensions and electrical characteristics after testing have been performed by Swiss Plasma Center (SPC) [49] and CERN [48]. As we can see in Fig. 43 the PFJEU1 is placed in the center of the reference system of SULTAN SMS, where the High Field Zone (HFZ) is found.
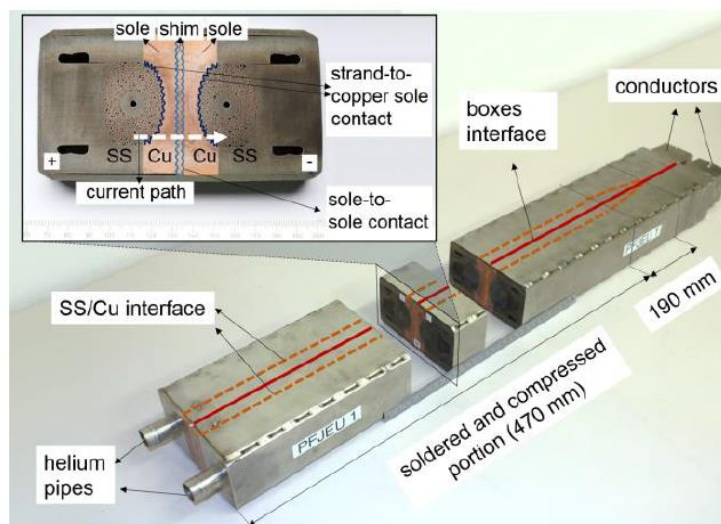

Fig. 42: PFJEU1 SULTAN Sample tested and subjected to electrical and geometrical measurements; the continuous line is the contact interface between the two boxes, whereas the dashed line is the contact interface between copper and stainless steel [48].

Inlet temperature of helium is measured in both legs (T0L and T0R at the helium pipes inlet) and two couples of sensors are placed respectively in the near section (T1 and T2) and in the far section (T3 and T4) along the joined cables. Both T1 and T2 are measured by only one temperature sensor (T8 and T7 respectively) while T3 and T4 are considered as the moving average value of three different temperature sensors located in three different surfaces of the squared jacket for each one of the two joined CICC (T3-T4-T6 and T1-T2-T5 respectively).

Voltage signals VN and VF are acquired from two voltage taps crowns in both legs at the far and near sections of the sample; each signal is the mean average value of raw signals recorded by voltage taps, located at the CICC jacket; voltage signal V1-V2 is used for the evaluation of total resistance in PFJEU1 sample.
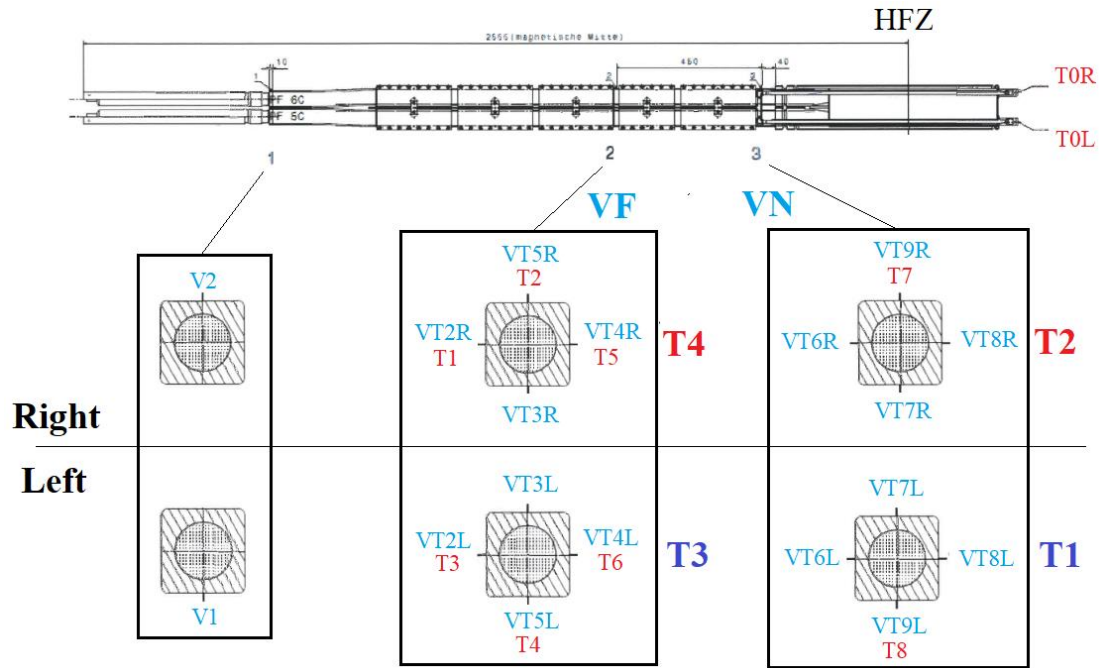
Fig. 43. : Instrumentation setting and layout in PFJEU1 sample tested in SULTAN. Near sensors are located at 40 mm from the joint inlet (near section 3) while far sensors are located at 490 mm (far section 2).

5.2. DC Resistance Analysis

We want to evaluate the electric resistance of PF6 Joint and check if the value found in the 3D FEM model is reliable and comparable with the one obtained with SULTAN DC Test Reference Run PFJEU1D171002 where R_{joint} = 1.82 nΩ, R_+ = 0.18 nΩ and R_- = 0.08 nΩ for the positive and negative sample terminals respectively.

We consider three SULTAN DC Tests Runs:

- PFJEU1D171002 with T = 4.5 K, B_{DC} = 0.5 T and I_{PF} = 0 - 55 kA with reversed polarity before EM cycling;

- PFJEU1D181001 with T = 4.5 K, B_{DC} = 3 T and I_{PF} = 0 - 55 kA with normal polarity before EM cycling;

- PFJEU1D191001 with T = 4.5 K, B_{DC} = 3 T and I_{PF} = 0 - 55 kA with normal polarity after EM cycling.

Using the Matlab code "ICAS 2018", developed by UNIBO for the post-processing of the experimental data recorded in the SULTAN Test Facility and specifically updated for the DC resistance analysis of joints, we obtain the resistance values of both upper terminations (Top Joint with R_+ and R_-) and PF6 Joint in the HFZ, using both near voltage taps (VN) and far voltage taps (VF) located at 40 mm and 490 mm from the joint's cable inlet respectively. PF6 Joint resistance has been calculated using two different methods and results are compared to check the reliability of the experimental analysis.

Using the Voltmetric Method the PFJEU1 DC resistance is calculated with eq. 52:

$$R_{volt}(I) = \frac{V(I)}{I} \tag{52}$$

The time index of every current step I (0-10-20-30-40-55 kA) is found at the end of each current plateau (when the transient regime is supposed to be over) and a corresponding value of voltage $V(I)$ is found, both for VN and VF, considering the mean value of the moving average value of the voltage signal in the last 50 seconds of each current plateau.

Using the Calorimetric Method the PFJEU1 DC resistance is calculated with eq. 53:

$$R_{cal}(I) = \frac{P(I)}{I^2} \tag{53}$$

where *P(I)* is the power transferred to helium during the DC Test, calculated with eq. 54:

$$P = \dot{m}_{He}(h_{out} - h_{in}) \tag{54}$$

where the inlet enthalpy h_{in} is calculated with T0L and T0R for left and right leg respectively, at the same pressure (9 bar) and temperature (4.5 K), while h_{out} depends from the temperature sensors chosen for the calculation.

The energy deposited in the PFJEU1, due to the current flowing in the sample is completely transferred to the helium mass flow (considering an adiabatic system made up of joint and cables), in which an increasing temperature is detected in both legs by various temperature sensors, starting from the measurement of a constant helium inlet temperature of 4.5 K. We consider the two temperature signals recorded both at the near section (T1 and T2) and at the far section (T3 and T4) as the downstream PFJEU1 temperatures; the inlet (upstream) temperature in PFJEU1 before the HFZ is T0, the mean value of T0L and T0R.

Results of DC resistance analysis with the two methods are shown in Fig. 44; the calorimetric measurement is not reliable at low currents, therefore inconsistent experimental data, given in Tab. 13, Tab. 14 and Tab. 15, are not considered in the plots.
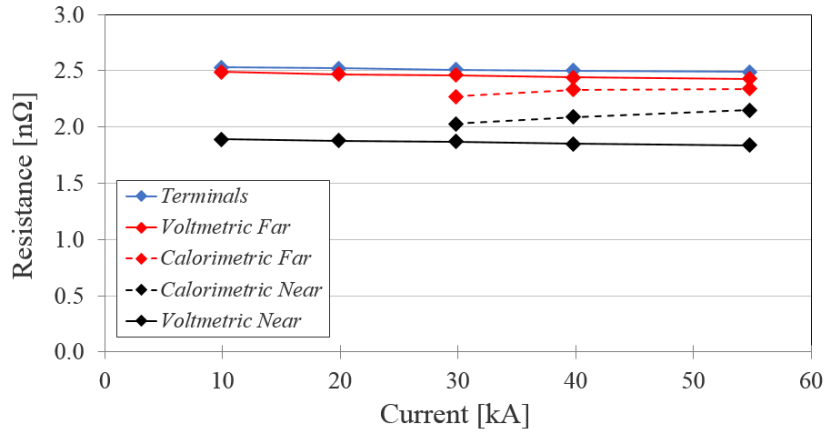
Fig. 44: Elaboration of experimental data for Test Run PFJEU1D171002 at 0.5 T before cycling.

PFJEU1D171002 @ B = 0.5 T, I = 0-55 kA before cycling				
Cur_s [kA]	$R_{volt\_}$FS [nΩ]	$R_{cal\_}$FS [nΩ]	$R_{volt\_}$NS [nΩ]	$R_{cal\_}$NS [nΩ]
9.75	2.49	~~1.18~~	1.89	~~1.41~~
19.74	2.47	~~2.06~~	1.88	~~1.90~~
29.72	2.46	2.27	1.87	2.03
39.70	2.44	2.33	1.85	2.09
54.66	2.43	2.34	1.84	2.15

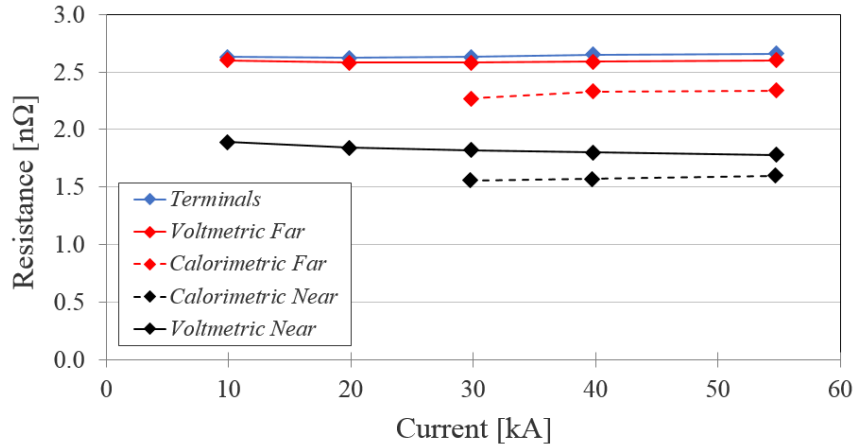Tab. 13: DC resistance value in each current step for SULTAN DC Test Run PFJEU1D171002.

Fig. 45: Elaboration of experimental data for Test Run PFJEU1D181001 at 3 T before cycling.

PFJEU1D181001 @ B = 3 T, I = 0-55 kA before cycling				
Cur_s [kA]	$R_{volt\_}$FS [nΩ]	$R_{cal\_}$FS [nΩ]	$R_{volt\_}$NS [nΩ]	$R_{cal\_}$NS [nΩ]
9.75	2.60	~~2.10~~	1.89	~~1.47~~
19.74	2.58	2.45	1.84	1.58
29.72	2.58	2.41	1.82	1.56
39.70	2.59	2.43	1.80	1.57
54.66	2.60	2.47	1.78	1.60

Tab. 14: DC resistance value in each current step for SULTAN DC Test Run PFJEU1D181001.
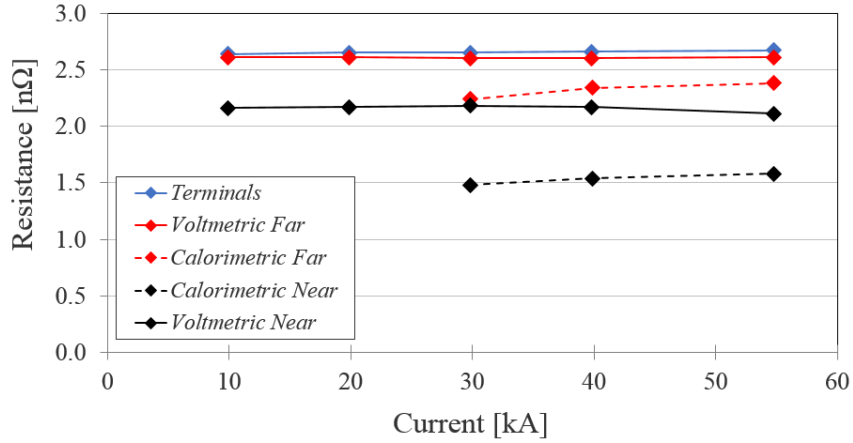

Fig. 46: Elaboration of experimental data for Test Run PFJEU1D191001 at 3 T before cycling.

PFJEU1D191001 @ B = 3 T, I = 0-55 kA after cycling				
Cur_s [kA]	R_{volt}_FS [nΩ]	R_{cal}_FS [nΩ]	R_{volt}_NS [nΩ]	R_{cal}_NS [nΩ]
9.88	2.61	~~0.91~~	2.16	~~0.65~~
19.87	2.61	~~1.96~~	2.17	~~1.32~~
29.84	2.6	2.24	2.18	1.48
39.82	2.6	2.34	2.17	1.54
54.79	2.61	2.38	2.11	1.58

Tab. 15: DC resistance value in each current step for SULTAN DC Test Run PFJEU1D181001.

The reference DC resistances are the voltmetric measurements in three different test conditions, as shown in Tab. 16.

	Electric Resistance R_{volt} [nΩ]					
	PFJEU1D171002 @ B = 0.5 T, I = 0-55 kA		**PFJEU1D181001** @ B = 3 T, I = 0-55 kA		**PFJEU1D191001** @ B = 3 T, I = 0-55 kA	
Sensors Section	Average	@ 55 kA	Average	@ 55 kA	Average	@ 55 kA
Far	2.46	2.59	2.59	2.43	2.61	2.61
Near	1.87	1.83	1.83	1.84	2.16	2.11

Tab. 16: Voltmetric DC resistance reference values at both far and near sensors sections in three different Test Runs.

We can see that the voltmetric DC resistance measured with far voltage sensors is always higher than that obtained with near voltage sensors since electrodynamic phenomena such as current redistribution in the CICC between superconducting cable and stainless steel jacket occur along outside the joint, thus leading us to take in account two different possible values of joint resistance. Low currents and tensions do not allow us to have a reliable

evaluation of electric resistance with the calorimetric method, whereas at higher current the calorimetric resistance appears quite uniform and stable.

As we can see in Fig. 47 [50] the background magnetic field is barely influent on the PFJEU1 DC resistance and any variation of the resistance with the field is only due to mechanical degradation of the cable. The dependence of DC resistance with EM cycling is shown in Fig. 48 where the PFJEU1 SULTAN Sample is indicated as SJ#1 [48]; we can see that the joint resistance increases with EM cycling and the copper contribution is only a half of the total resistance of PFJEU1.
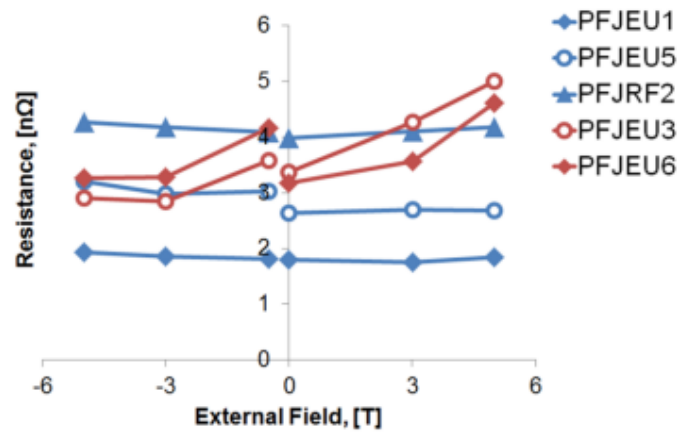

Fig. 47: DC resistance as function of background field for different PF joint samples [50]
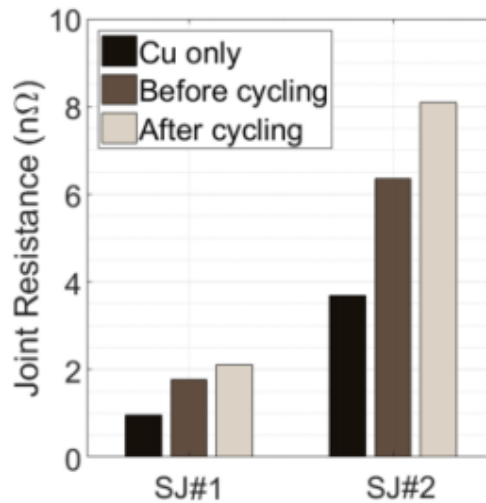

Fig. 48: DC resistance of PFJEU1 and PFJEU2, named SJ#1 and SJ#2 respectively [48].

5.3. AC Losses Analysis

The dependence of AC Loss from the frequency of the AC pulsed field in PF6 Joint has been investigated at the SULTAN test facility considering various operating scenarios, taken from the PFJEU1 Test Program and exposed in Tab. 17. We can study the behavior of PF6 Joint under a constant magnetic load of $B_{DC} = 3$ T due to the DC Coils and a magnetic oscillation of $B_{AC} = \pm 0.2$ T generated by an excitation current $I_{pulse} = \pm 230\sin(2\pi f t)$ A in each turn of the AC Coils; both legs operate at 4.5 K, with or without transport current I_{sample}.

AC Loss Measurement Tests									
File	B_{DC}	I_{Sample}	**T Left**	**T Right**	**dm/dt L**	**dm/dt R**	I_{pulse}	f	**NOTE**
	T	kA	K	K	g/s	g/s	A	Hz	**±0.2T**
PFJEU1A191005					10	10		1	40 s
PFJEU1A191006					10	10		0.8	40 s
PFJEU1A191007					10	10		0.6	40 s
PFJEU1A191008					10	10		0.4	50 s
PFJEU1A191009	3.0	0	4.5	4.5	5	5	±230sin	0.2	80 s
PFJEU1A191010					5	5		0.1	80 s
PFJEU1A191011					5	5		0.08	75 s
PFJEU1A191012					5	5		0.06	83.33 s
PFJEU1A191013					5	5		0.04	75 s
PFJEU1A191014					5	5		0.02	100 s
PFJEU1A191015					5	5		0.04	75 s
PFJEU1A191016					5	5		0.06	83.33 s
PFJEU1A191017					5	5		0.08	75 s
PFJEU1A191018	3.0	55	4.5	4.5	5	5	±230sin	0.1	80 s
PFJEU1A191019					5	5		0.2	80 s
PFJEU1A191020					8	8		0.4	50 s
PFJEU1A191021					8	8		0.6	50 s
PFJEU1A191022					8	8		0.8	50 s - QUENCH

Tab. 17: AC Loss measurement tests of PFJEU1 in the PF6 FSJS Test Program.

Using the Matlab Code "ICAS 2018" we can obtain the AC loss evaluation in PFJEU1 applying the calorimetric method using eq. 54.

Considering the first AC Test Run PFJEU1A191005 at 1 Hz we can see that temperature profiles in left leg and right leg obtained with far temperature signals T3-T4 (Fig. 49a) are comparable because the fluid-dynamic profile of helium in both legs is more uniform far from the joint helium outlet: if we use the near signals T1-T2 (Fig. 49b) we observe a difference of 0.3 K between left leg and right leg and the temperature is also lower than that measured far from the joint.
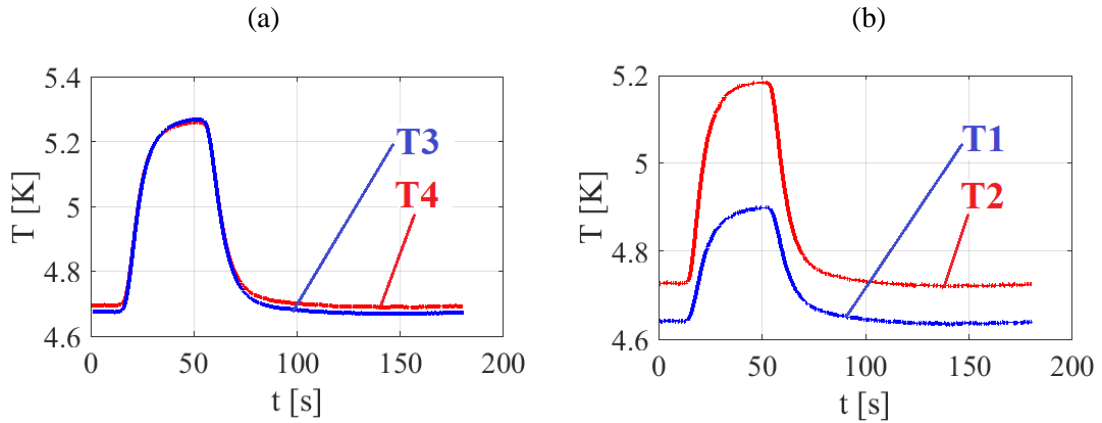
Fig. 49: Temperature profiles (a) far from the joint with temperature sensors T3-T4 and (b) near the joint with temperature sensors T1-T2 for a field pulse of 0.2 T at 1 Hz.

The power transferred to the helium is plotted in Fig. 50 for two different couples of temperature sensors.
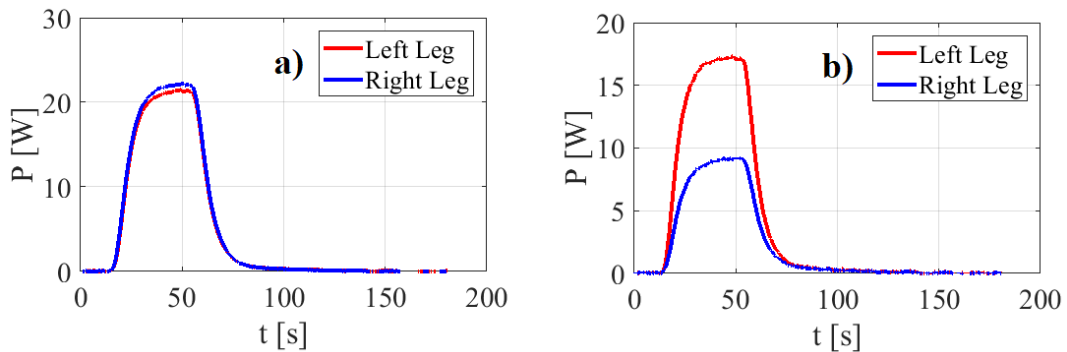

Fig. 50: Power dissipation profiles in both legs considering (a) far temperature sensors T3-T4 and (b) near temperature sensors T1-T2 for a field pulse of 0.2 T at 1 Hz.

The integration of the power loss in time for each leg allow us to find the total energy (J) dissipated in each leg of the PFJEU1 sample; summing the results for each leg and dividing this value by the number of current cycles (depending from the frequency and the duration of the magnetic field variation) we can find the energy (J/cycle) dissipated in PFJEU1 sample. In the following plots (Fig. 51 and Fig. 52) we expose the experimental results of AC losses analysis in case of null transport current (AC Test Runs from PFJEU1A191005 to PFJEU1A191014) and in case of a transport current of 55 kA (AC Test Runs from PFJEU1A191015 to PFJEU1A191021) showing how the choice of temperature sensors influences the total energy values and the shape of the experimental curve of the dissipated energy per cycle.
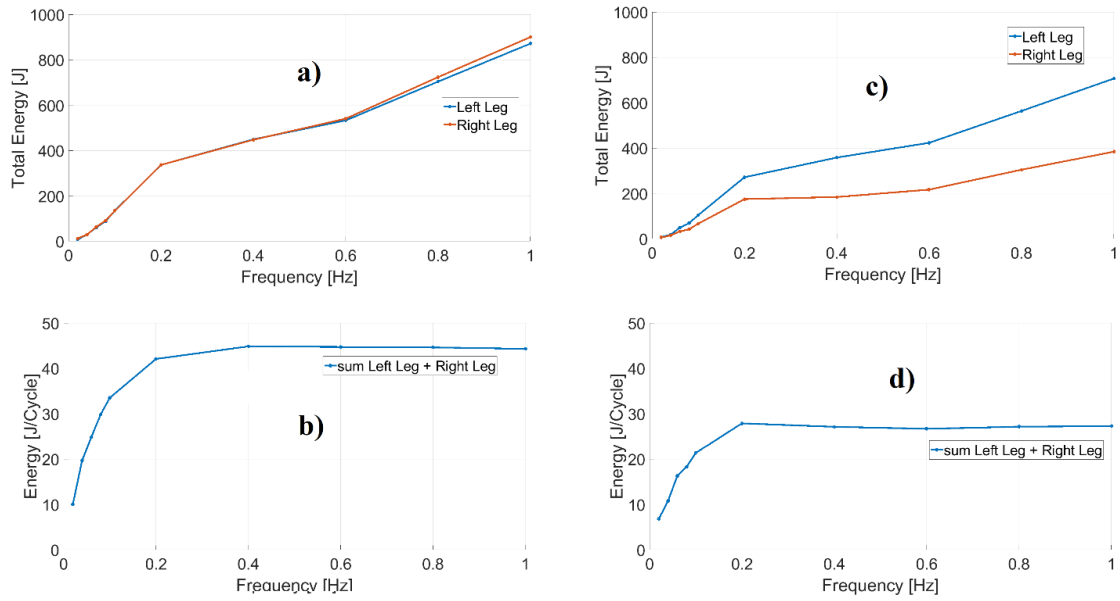
Fig. 51: (a)-(c) Total energy and (b)-(d) energy per cycle at null transport current considering the far temperature sensors and the near temperature sensors respectively.
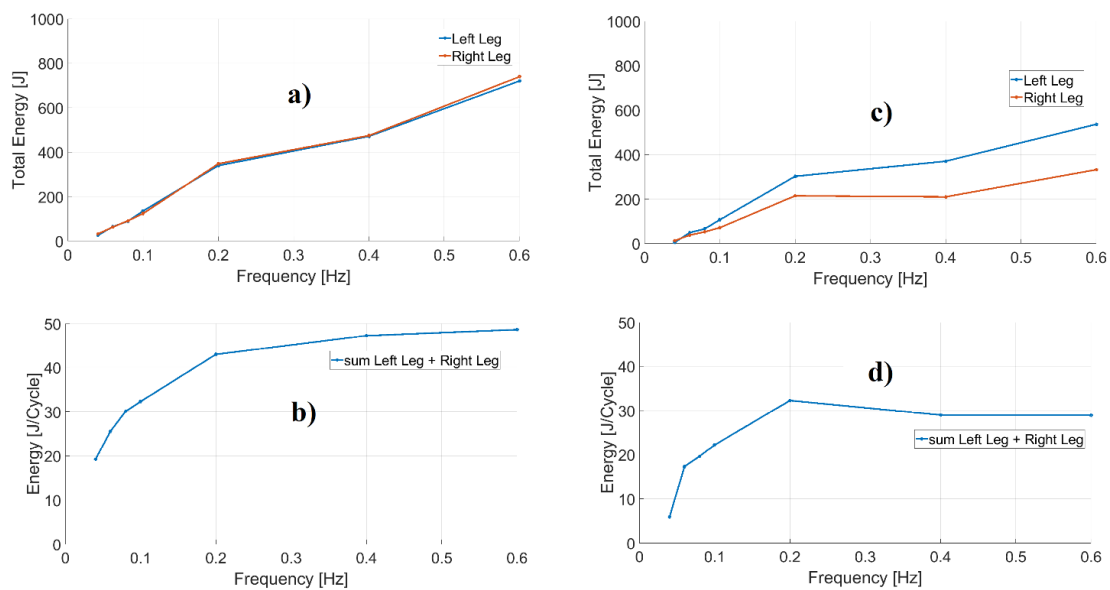

Fig. 52: (a)-(c) Total energy and (b)-(d) energy per cycle with 55 kA transport current considering the far temperature sensors and the near temperature sensors respectively.

We can compare our results of AC losses analysis campaign (Fig. 53) with those given in the PFJEU1 SULTAN Sample Test Report [49] in Fig. 54. These two sets of data are well in line whereas UNIBO investigation is a bit different concerning the peak value of AC loss with transport current, occurring at higher frequency, and the saturation of energy loss at high frequency.
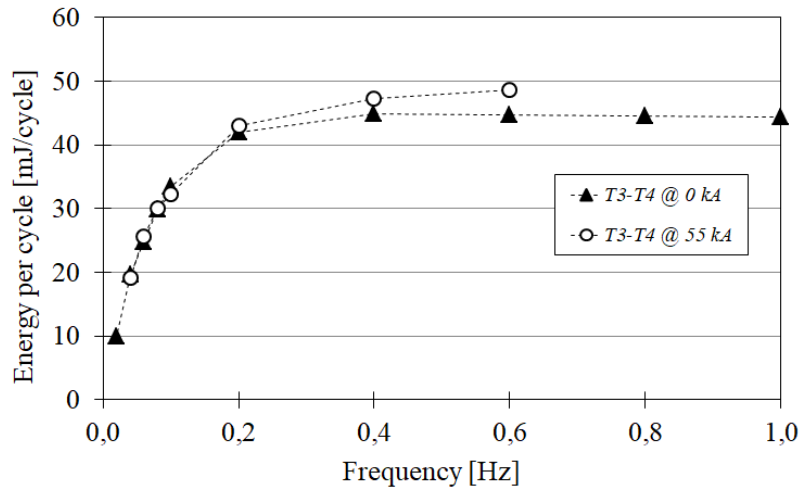
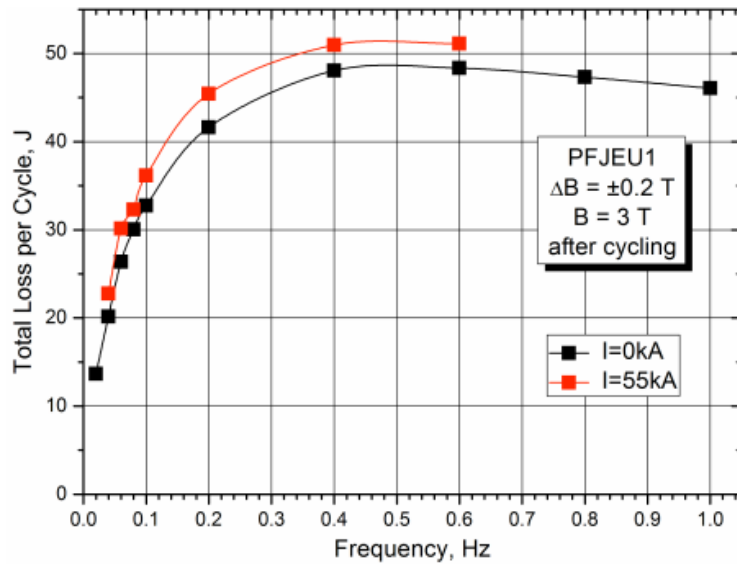Fig. 53: AC losses evaluation of PFJEU1 SULTAN Sample performed by UNIBO.

Fig. 54: AC losses evaluation of PFJEU1 SULTAN Sample performed by SPC [49].

Those differenced may be due to the different equation used for the helium enthalpy evaluation in the postprocessing of experimental data: UNIBO analysis uses a polynomial function of the temperature and pressure, whereas SPC analysis is done with Helium Pack.

6. Numerical Models for Transient Analysis of PFJEU1

6.1. 3D FEM Models

A 3D FEM code allows one to obtain numerical resolution of AC losses in a discretized spatial and time domain under specific boundary conditions. In this work we use ANSYS Maxwell 3D FEM code for the numerical evaluation of the electric resistance and AC losses of geometrical models of the PF joint, where different material properties are found (superconducting domain, copper and stainless steel). The computational burden depends on both dimensions and accuracy of the model, increasing with the number of tetrahedrons of which the mesh is composed: finer space and time discretization lead to a more accurate result but request lot of calculation time.

The real PF6 DP joint in the SHC (Fig. 55) is implemented in the 3D FEM code following the final design with nominals dimensions, before any machining of the twin-box assembly: TIG welding has not been implemented since its contribution to AC losses is considered negligible. The copper domain is divided in two soles with a shim in between, ensuring a contact length of the joint $l = 450$ mm where the current transfer between the two superconducting cables (not implemented) in ensured; the current density distribution is not uniform in the joint and the inductive effects are considered in case of current flowing in any direction.
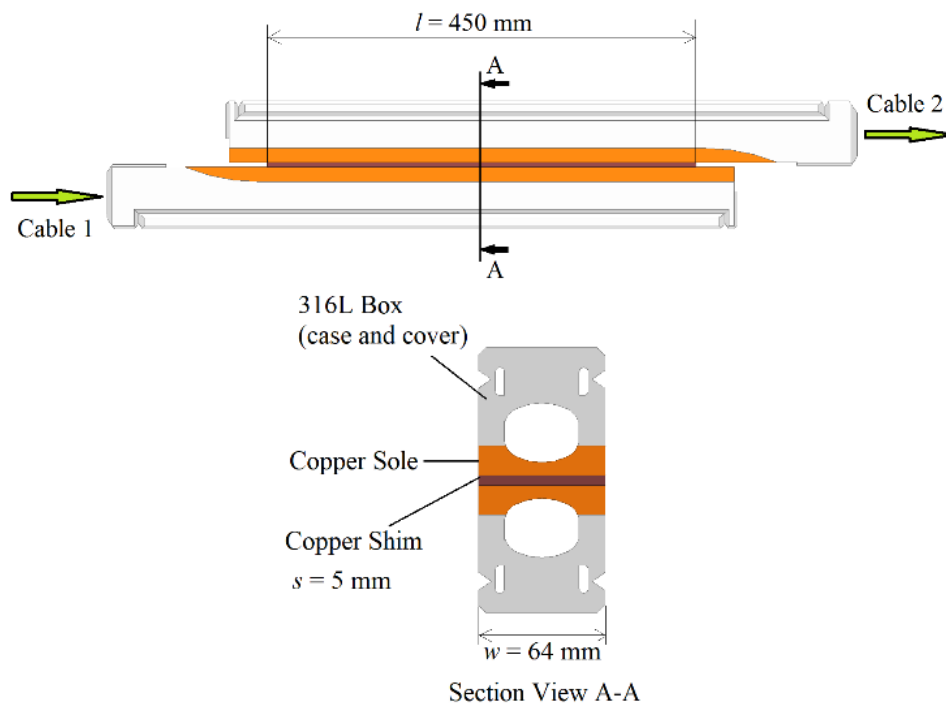

Fig. 55: Real PF6 DP joint implemented in 3D FEM code (top) and its section view in the transversal plane (bottom).

The PFJEU1 in the PHC (Fig. 56) is implemented in the 3D FEM code following the final design with nominal dimensions before any machining and testing campaign of the SULTAN sample, nevertheless few modifications of the model should be taken in account since last measurements on the tested PFJEU1 [48] show a reduction of copper thickness, as is shown in Tab. 18. The two CICCs are modelled as a uniform NbTi hollow cable in a square stainless steel jacket in contact with the joint, placed at the very center of the two AC coils; perfect contact between different materials is ensured and no contact resistance is implemented. To enhance the superconducting behavior of the cable we impose an isotropic conductivity of NbTi domain using 10^{15} S/m both in longitudinal and transversal direction; further parametric analysis will take in account a lower transversal conductivity c_t [S/m] in the range of $10^6 - 10^9$ in order to consider an equivalent transversal resistance R_s [Ω] due to the contact resistances along the current path from left leg to right leg (NbTi filament, matrix, superconducting strands, wrapping, copper connection and reverse). No twisted cabling layout has been considered, thus the AC loss evaluation will be affected by errors due to the rough model of the cable. The numerical results of DC resistance is compared with experimental results, fitting different parameters, such as cable transversal conductivity and copper RRR, in order to obtain a reliable numerical model of the SULTAN sample.
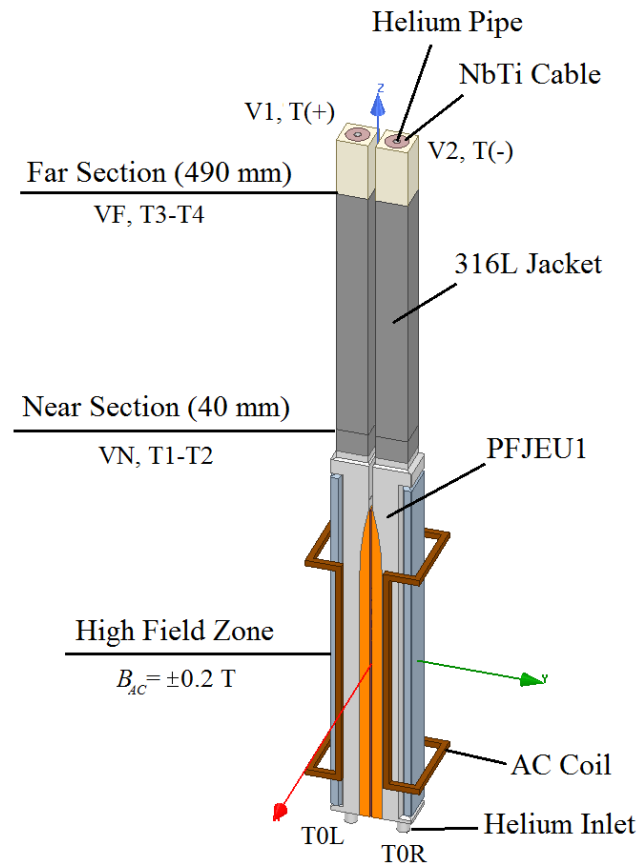

Fig. 56: PFJEU1 model in the 3D FEM code representing the SULTAN sample; sensors are not implemented.

Dimensions [mm]	Design PFJEU1	Measurement SJ#1
Cu sole max thickness	17	14.6
Cu sole min thickness	8.5	6.4
Cu shim thickness	3	2

Tab. 18: Difference between design dimensions and measured dimensions of PFJEU1 [48]: the length of SJ#1 is considered equal to that of PFJEU1 (570 mm) even if it might be lower (470 mm), as we can see in Fig. 42.

A simplified model of the PFJEU1 SULTAN Sample (Fig. 57) is implemented in the 3D FEM code for the comparison between numerical results with a different method; a 570 mm long copper domain with uniform cross section represents the electrical connection between the two NbTi cables (not implemented).
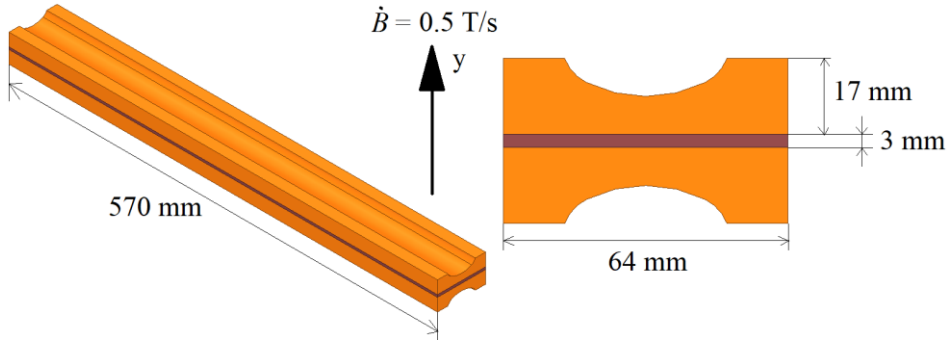

Fig. 57: Simplified model of PFJEU1 in the 3D FEM code for the comparison between results obtained with two different numerical codes.

Since the PF6 Joint is tested in presence of a background field $B_{DC} = 3$ T we have to consider the magnetoresistance in the copper domain (eq. 8) thus reducing the bulk conductivity of the electric connection between two joined superconducting cables.

In Tab. 19 the electromagnetic characteristics of PF6 Joint are reported; we can see that the stainless steel resistivity is not affected by the external magnetic field.

Domain	Resistivity [nΩ·m]		Bulk Conductivity [S/m]		Relative Permeability
	0 T	3 T	0 T	3 T	
Copper RRR=6	2.82	2.88	$3.55 \cdot 10^8$	$3.47 \cdot 10^8$	1
316L Stainless Steel	553.4	553.6	$1.80 \cdot 10^6$	$1.80 \cdot 10^6$	1

Tab. 19: Electromagnetic characteristics of PF6 DP joint and PFJEU1 at 4.5 K evaluated according to the previous equation for resistivity $\rho_{Cu}(T,B,RRR)$ and $\rho_{SS}(T)$.

6.2. THELMA Models

The THELMA code has been developed by UNIBO to model the electromagnetic (EM) characteristics of the ITER CICCs and joints [51, 52] in order to evaluate the AC losses in the PFJEU1 SULTAN sample. The electromagnetic model of the joint in THELMA code is based on a distributed parameter circuit approach. The equations of the model are derived from the Magneto-Quasi-Static formulation of the Maxwell equations. The cross section of the joint is discretized in Cable-Elements (CEs) that are the conductive domains of the model: each CE can represent a single NbTi strand or a composite domain made up of NbTi and copper wires wound in triplets or petals. A sketch view of the cable discretization is shown in Fig. 58.
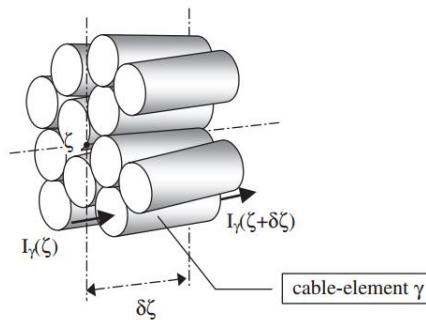

Fig. 58: Segments of superconducting twisted CEs [52].
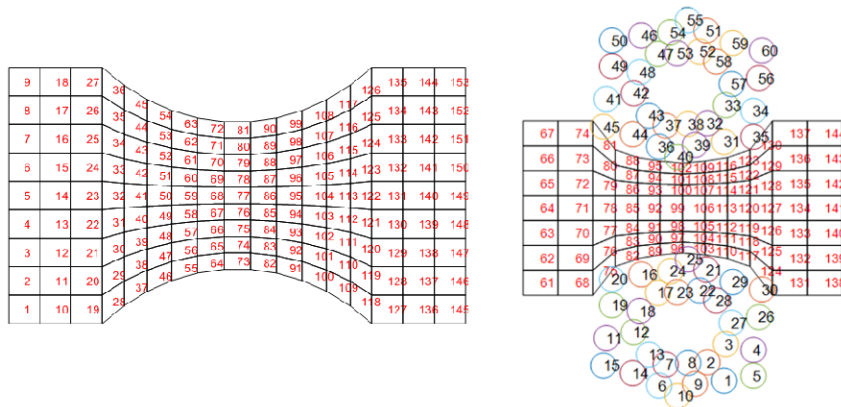

Fig. 59: Two different THELMA models of PF joint: simplified PFJEU1 model for validation of the two numerical codes (left) and PFJEU1 model for comparison between calculated and experimental results (right).

Two different models of the PF joint have been implemented: a simplified model of the PFJEU1 sample for the comparison between numerical codes (Fig. 59 left), with the same geometries of the corresponding 3D FEM model, discretized in 153 copper CEs, and the PFJEU1 sample tested in SULTAN for the DC resistance and AC losses analyses (Fig. 59 right), which dimensions are the nominal values before any machining of the joint, considering the change in cross section due to the twisted layout of the compressed cable, discretized in 60 NbTi CEs and 84 copper CEs.

64

The total length of both joints is discretized in 100 segment of length $\delta\zeta$; the stainless steel domain is neglected for simplification since the computational time increases with the bulk resistivity of the conducting domain.

The unknowns of the problem are the values of the difference currents of the cable elements, that are function of the longitudinal coordinate ζ along the joint, considering a uniform current distribution in the CE cross section:

$$i_\gamma = I_\gamma - \frac{I}{N_{CE}} \quad \text{with } \gamma = 1, \ldots, N_{CE} \tag{55}$$

where I_γ is the current in the γ-th CE and I is the total current of the cable given by the sum of the current in each CE. The scalar electrical potential and the magnetic vector potential are solved. The current density continuity condition is added to compute the current density in each discretized CE according to the following equation derived from the induction law:

$$\vec{E}(\boldsymbol{P}, t) = -\nabla V - \frac{\partial}{\partial t}\left[\frac{\mu_0}{4\pi}\int_\Omega \frac{\vec{J}(\boldsymbol{Q}, t)}{|\boldsymbol{P} - \boldsymbol{Q}|}d^3\boldsymbol{Q}\right] \tag{56}$$

$$\nabla \cdot \vec{J} = 0 \tag{57}$$

where $\boldsymbol{P}$ and $\boldsymbol{Q}$ are the location of the CE centers in the discretized joint domain of volume Ω of length $\delta\zeta$. The closure of equations is obtained by the Power Law as a constitutive law of the superconducting material according to:

$$E = Ec\left[\frac{J}{J_c(T,B)}\right]^{n(T,B)} = \rho_{eq}(J, B) \cdot J \tag{58}$$

where the equivalent resistivity ρ_{eq} depends on the contribution of normal matrix and SC resistivities and $n(T,B)$ is the order of the power law.

The self and mutual per-unit-length induction coefficients are numerically calculated from geometrical parameters of the cable such as twist pitches and cable-axes trajectory. From the geometrical parameters is also computed the per-unit-length conductance between CEs as a function of the longitudinal coordinate, that is defined in two different ways:

- When the CEs are two different object in contact, as the strand in the cable or the soldered interface between strands and copper sole, the cross section of the CEs is amplified by a factor of G_F, usually set to 1.7; a contact length L_c is found, and the transverse per-unit-length conductance $G_{\gamma,k}$ [S/m] is computed by multiplying the per-

unit-surface conductance $\sigma_{\gamma,k}$ [S/m^2], that is the fitting parameter of the model, by the contact length, obtaining:

$$G_{\gamma,k} = \sigma_{\gamma,k} \cdot L_c \tag{59}$$

-   When two CEs are resulting from the discretization of a solid, as the CEs modeling the copper soles or the NbTi cables, the transverse per-unit-length conductance $G_{\gamma,k}$ is defined as:

$$G_{\gamma,k} = \sigma L_c \cdot \frac{d_{\gamma,k} \cdot \hat{n}}{d_{\gamma,k} \cdot d_{\gamma,k}} \tag{60}$$

where σ [S/m] is the bulk conductivity of the material in the γ-th CE, $\hat{n}$ is the unit vector perpendicular to the contact surface and $d_{\gamma,k}$ is the distance between the two CE centers. The maximum value of $d_{\gamma,k}$ can be chosen in order to neglect magnetic coupling between far NbTi strand, saving computational time.

The magnetic field generated by the current flowing in transvers direction in the copper saddle from one superconducting cable to the other is neglected thus underrating the inductive effects occurring in the joint when a variation of the background field is applied: the total inductance of the joint will consider only the eddy and coupling effects due to the longitudinal currents in the CEs. The electric characteristics of the copper in the THELMA model are the same used for the 3D FEM models, shown in Tab. 17.

The solution of the numerical analysis is obtained by solving the following equation:

$$A\frac{dY_{EM}}{dt} = F(t, Y_{EM}, T_{EM}) \tag{61}$$

where A is the matrix which takes in account the magnetic coupling between the currents at the nodes of the 3D mesh, Y_{EM} is the vector containing the current differences i_γ and F is the non-linear function which takes in account the external magnetic field effects, the Joule effects, the transverse conductance effects depending from the temperature of the conductors T_{EM}.

The solution of eq. 61 can be obtained by means of a fifth-order Runge-Kutta scheme or by an implicit scheme based on the trapezoidal rule [52].

66

6.3. The SULTAN SuperMagnet System Model

The PFJEU1 sample has been tested in the SULTAN facility under various operating scenario occurring in the ITER reactor. Both in 3D FEM and THELMA codes, the SULTAN SuperMagnet System Model (SMSM) is made up by three split superconducting DC Coils for the constant background field B_{DC} in the x direction and a pair of AC Coils, each one made by 100 turns, for the variable background field B_{AC} in the y direction. The PFJEU1 model is implemented inside the SMSM with the center located at the reference system origin, coinciding with the center of all coils (Fig.60). Each DC Coil is supplied with a constant excitation current I_{DC_Coil} for each B_{DC} value, as we can see in Tab. 20, which value is obtained from:

$$I_{DC} = n \times I_n \times \frac{B_{DC}}{11.2} \tag{62}$$

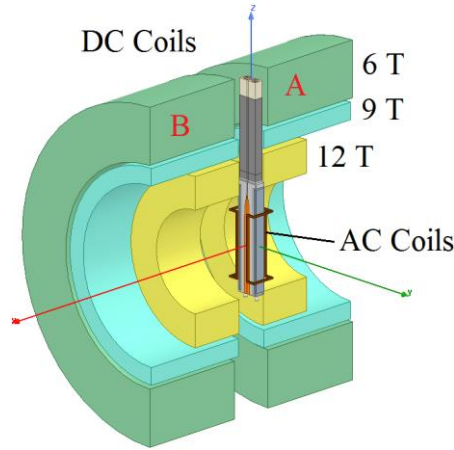where I_n is the current in each turn depending from B_{DC} value.

Fig. 60: The SULTAN SMSM with the PFJEU1 model inserted in the High Field Zone.

	SULTAN Coils								
	6T Coil			9T Coil			12T Coil		
		A	B		A	B		A	B
	Turns n	860	860	Turns n	240	192	Turns n	297	299
B_{DC} (T)	I_n (A)	I_{DC} (kA)		I_n (A)	I_{DC} (kA)		I_n (A)	I_{DC} (kA)	
0.5	215	184.9	184.9	550	132	105.6	284	84.384	84.916
3	1292	1111.12	1111.12	3299	791.76	633.408	1704	506.088	509.496
5	2154	1852.44	1852.44	5499	1319.76	1055.808	2840	843.48	849.16
10	4307	3704.02	3704.02	10997	2771.28	2217.024	6248	1686.96	1698.32
11.2	4842	4148.64	4148.64	12317	2956.08	2364.864	6362	1889.514	1902.238

Tab. 20: Total current in each DC Coil for different B_{DC} field values in the SULTAN SMSM.

In Fig. 61 we show respectively the magnitude and the vector distributions of maximum background field B_{DC} = 11.2 T in both X-Z and Y-Z planes.

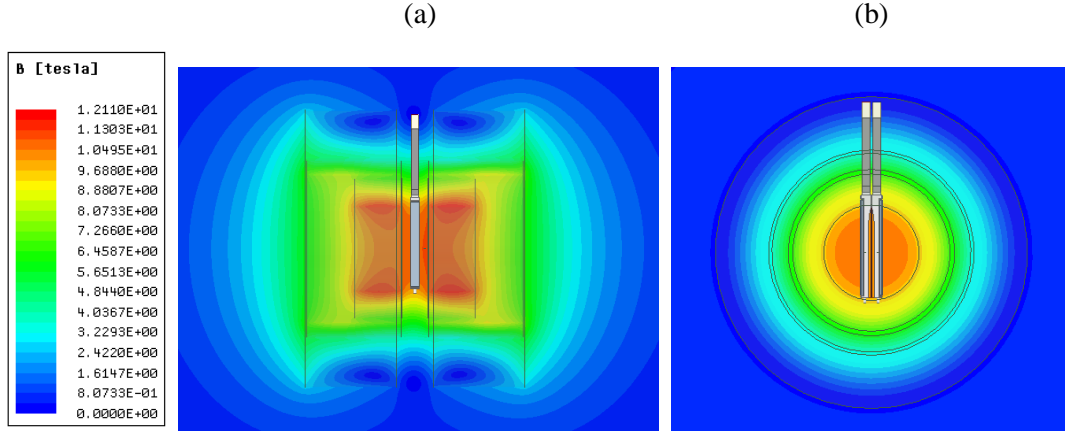(a)   (b)

Fig. 61: Magnitude distribution of B_{DC} in (a) X-Z and (b) Y-Z cross sections of the SULTAN SMSM.

The SMSM is implemented in THELMA Code and maximum field profiles (Fig. 62) are compared finding a maximum percentage error of less than 0.1% between 3D FEM and THELMA models. The DC Coils of SULTAN SMS can be neglected in the 3D FEM model of the SULTAN experiments for both DC resistance and AC losses evaluation since the background field effect is already taken in account in the copper resistivity, evaluated at 3 T according to eq. 33 (see Tab. 19); we can observe that the PFJEU1 sample is subjected to a uniform background field along x direction therefore a constant resistivity of the joint can be assumed.
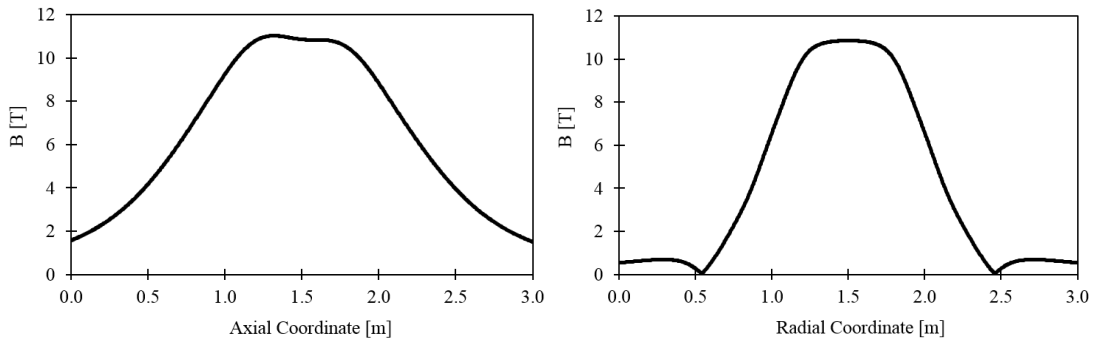

Fig. 62: Magnitude of axial (left) and radial (right) background DC field in the SULTAN SMSM obtained with the 3D FEM code.

The nominal pulsed B_{AC} = ±0.2 T along y axis is generated by AC Coils, each one fed with a total current of I_{AC} = 23sin(2πft) kA (Fig. 70a), that is 230 A for 100 turns in each coil. In Fig. 63b we can see that the nominal AC field pulse, produced by the nominal AC current pulse, is reduced to ±0.176 T and delayed of 0.1 s by inductive effects in the joint, where induced

68

currents are generated; after a first transient regime the AC field starts to follow the excitation current with the same frequency.
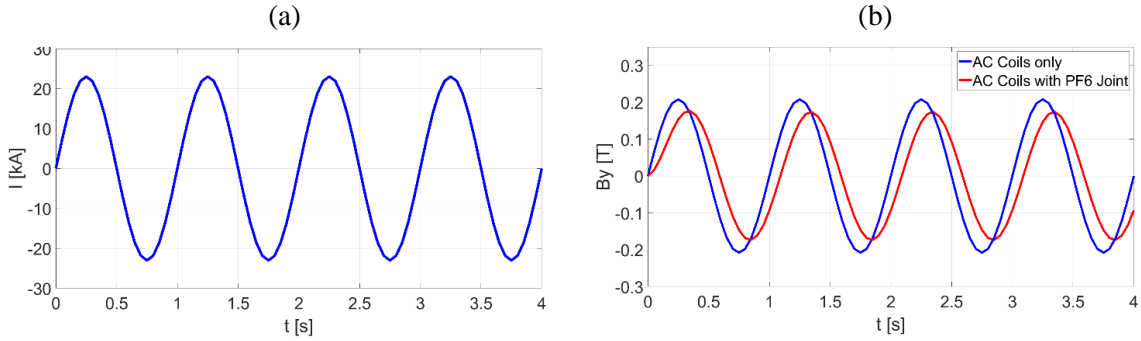

Fig. 63: (a) Input current in AC Coils and (b) AC field profile in the SULTAN SMSM.

6.4. DC Resistance Analysis

The numerical analysis for the DC resistance evaluation of the PFJEU1 model has been carried out with an "Electric Transient Analysis" in the 3D FEM code.

The unitary voltage drop of $V_{DC} = 1$ V is applied at the terminal superconductor cross section imposing 1 V at the right leg and 0 V at the left leg as boundary conditions; the initial voltage is set at 0 V and the 3D FEM code evaluates the current density distribution in all the PFJEU1 model after 10^{-5} s for which the convergence of result is ensured. The total current flowing in the sample is:

$$I = \int_{\Sigma} \vec{J} \cdot \hat{n} \, dS \tag{63}$$

where Σ is the cross section interested by the transport current density induced by the voltage V_{DC}. The current I should be the same if evaluated both at the inlet or outlet current terminals and in the joint, where the current distribution is not uniform, therefore the measure should be less reliable.

The DC analysis has been carried out considering different resistivity for the copper domain and geometries of the joint, taking in account the design dimensions and those measured after the testing campaign in the SULTAN facility, as we can see in Tab. 21.

The computed value of R_{joint} with different RRR in the copper soles and shim (taken from the resistivity measurements on the tested PFJEU1 sample that is SJ#1 in [48]) is well in line with experimental reference values before EM cycling and the magnetoresistance effect is well predicted by the numerical model. Using the measured resistivity of the copper we obtain a

low joint resistance: if the contact resistance is implemented a higher value of joint resistance could be expected.

DC Joint Resistance R_{joint} [nΩ]		Experimental and Numerical Parameters		SULTAN field B_{DC} [T]			
				0.5		3	
				Near	Far	Near	Far
Experimental		Before Cycling	55 kA			1.78	2.60
			-55 kA	1.84	2.43	1.89	2.55
		After Cycling	55 kA			2.11	2.61
			-55 kA			1.89	2.56
3D FEM	PFJEU1	RRR = 6 in copper sole and shim		2.22		2.68	
		RRR = 7.44 in copper sole RRR = 420 in copper shim		1.89		1.94	
	SJ#1	ρ_{Sole} = 1.94 nΩ ρ_{Shim} = 0.03 nΩ		1.44			

Tab. 21: Comparison between experimental and numerical results of DC resistance analysis. The copper resistivity of the PFJEU1 model with different RRR is evaluated with eq. 33, whereas for the SJ#1 the measured value is considered; isotropic bulk conductivity of 10^{15} S/m is adopted in the NbTi cable for each model.

The influence of the transversal conductivity c_t [S/m] of the NbTi cable is investigated in the SJ#1 model with a parametric analysis; results are shown in Fig. 64 and Fig. 65. It can be noticed that the voltage drop occurs mostly in the copper domain of the joint and the DC resistance R_{joint} decreases with high transverse conductivities approaching to the isotropic bulk conductivity condition in which $c_t = 10^{15}$ S/m.

A possible and reliable value of transverse conductivity of the NbTi cable is 10^8 S/m, that is related to a transverse resistivity of 10^{-8} Ω·m
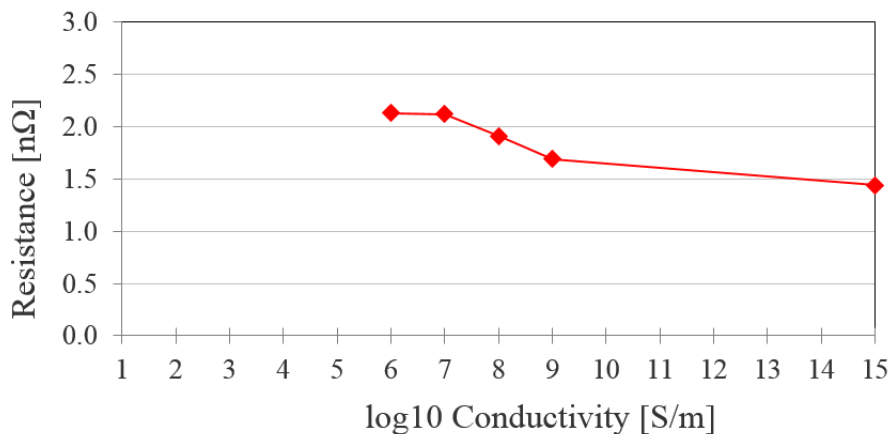

Fig. 64: Change in joint resistance with the transvers conductivity of the NbTi cables.
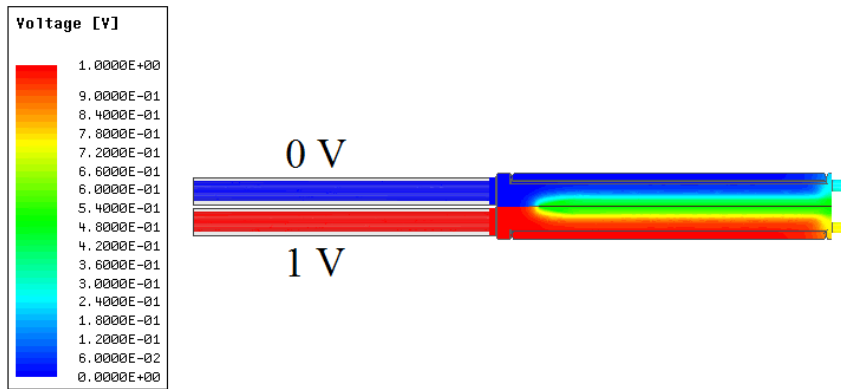
Fig. 65: Calculated voltage of PFJEU1 model in the 3D FEM code using a NbTi transvers conductivity of 10^8 S/m.

The fitting parameter c_t will be used in AC losses evaluation in the 3D FEM code with the updated geometry and *RRR* for the copper. The implementation of the twisted cabling layout with the insertion of the contact resistance domain is very expensive in terms of computational costs and will be performed in the future.

6.5. AC Losses Analysis

The numerical analysis for the AC losses evaluation of the PFJEU1 has been carried out with the THELMA code considering the joint model in Fig. 59 (right), where the copper sole and the two superconducting cables are implemented as 84 and 60 CEs respectively, in a 570 mm long electrical connection with uniform cross section. The AC pulsed field is applied on the transversal direction perpendicular to the joint plane. The copper *RRR* is set equal to 6. The comparison between experimental and numerical results is shown in Fig. 66; the experimental curve is representative of the dissipation evaluated with the far temperature sensors without transport current in the SULTAN sample (Fig. 51b).
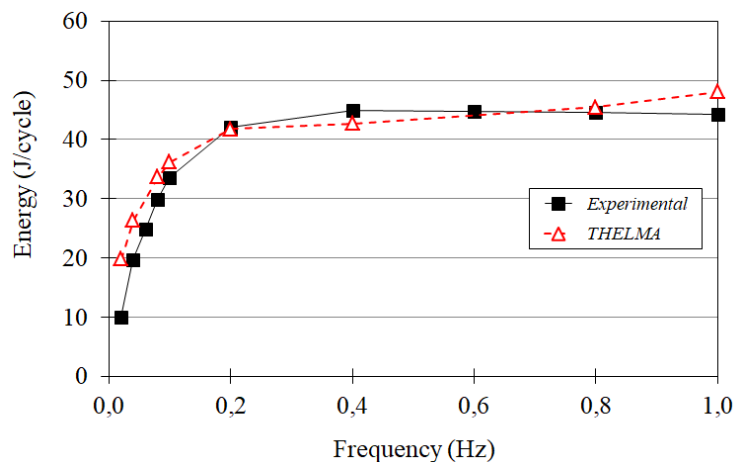

Fig. 66: Comparison between experimental and numerical results of AC losses analysis in PPFJEU1 sample.

We can notice that the calculated energy loss peak of 48 J/cycle is found at 1 Hz whereas the loss at 0.4 Hz is 42.7 J/cycle, which is lower than the experimental peak value of 44.8 J/cycle. The AC losses vs. frequency curve is always overrated at low frequencies in the THELMA code and the behavior of the calculated AC losses is not well defined at higher frequencies, therefore a further numerical analysis at higher frequencies up to 10 Hz has been carried out, finding the peak loss 69.3 J/cycle at 4 Hz. If we consider only the copper domain the increase of energy loss with frequency is slower and the peak value is 93 J/cycle at 2 Hz, whereas the AC losses of the NbTi cables, without any joint in between, reach the maximum value of 37.6 J/cycle at 0.2 Hz considering a per-unit-surface conductivity of $4 \cdot 10^{10}$ S/m^2. Results are shown in Fig. 67.

The transvers conductivity of the cable is the fitting parameter of the THELMA model and it has been chosen to obtain the minimum percentage error between computed and experimental results in the range of 0 – 1 Hz; however, for higher frequencies, the losses in the copper exceeds the expected value, thus generating a joint losses curve that is not representative of the experimental one.
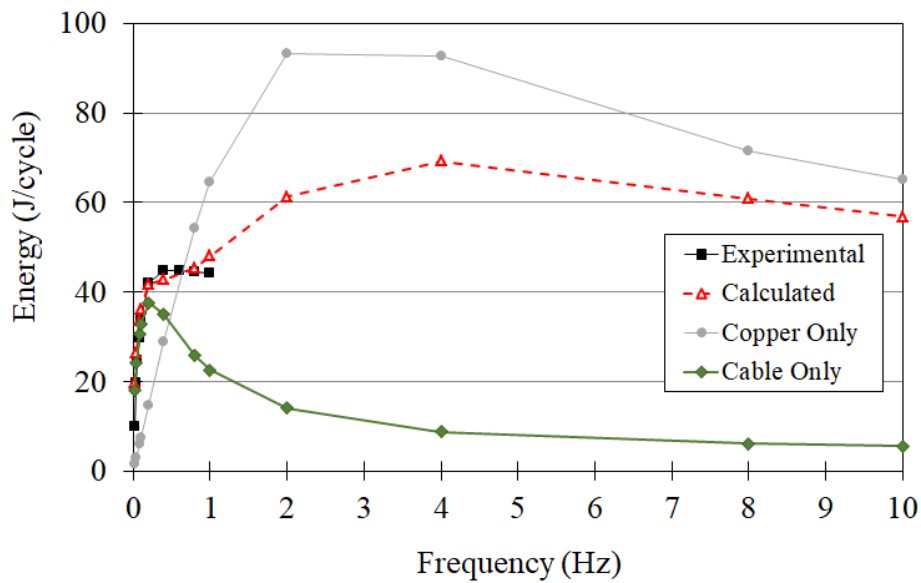

Fig. 67: Comparison between numerical results of AC losses in different domain for frequency up to 10 Hz.

Considering the frequency of 0.4 Hz, corresponding to the experimental maximum energy of 44.8 J/cycle, we evaluate the power loss evolution during the field pulse of the SULTAN AC coils: the transient regime ends after the first cycle and at 2.5 s the steady state regime is reached, with a constant maximum total of 27.2 W for the joint, with almost the 60% of the dissipation due to the coupling current losses in the NbTi CEs. The maximum loss value for the cables and for the copper are 2 W and 13 W respectively, as shown in Fig. 68.
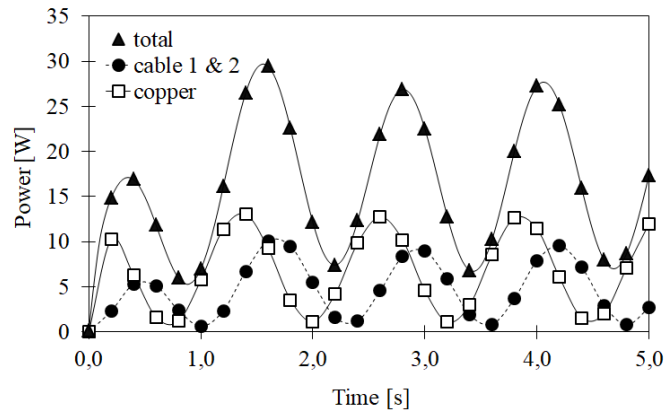
Fig. 68: Power loss evolution during the AC pulsed field of 0.2 T at 0.4 Hz: the total dissipation is the sum of the loss in NbTi cables and in the copper sole.

In Fig. 696 we show the current evolution in the superconducting CE at the central position of the joint during the AC field pulse at the maximum loss frequency of 0.4 Hz: a clear coherence between current oscillation in the two cables is found, being symmetrical in the "twin-box" joint configuration. The current distribution among superconducting CEs at 4 s along the joint length is plotted in Fig. 70. Even if only few CEs are represented for simplification, it is clear that the maximum current value in the CEs is more than 1.5 kA at the end of the transient regime.
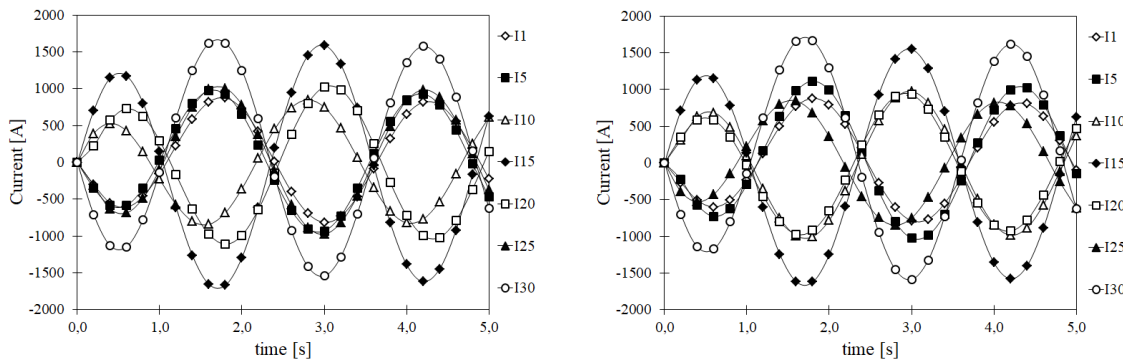

Fig. 69: Current evolution in the center position of Cable 1 (left) and Cable 2 (right) in the joint during the AC pulsed field of 0.2 T at 0.4 Hz.
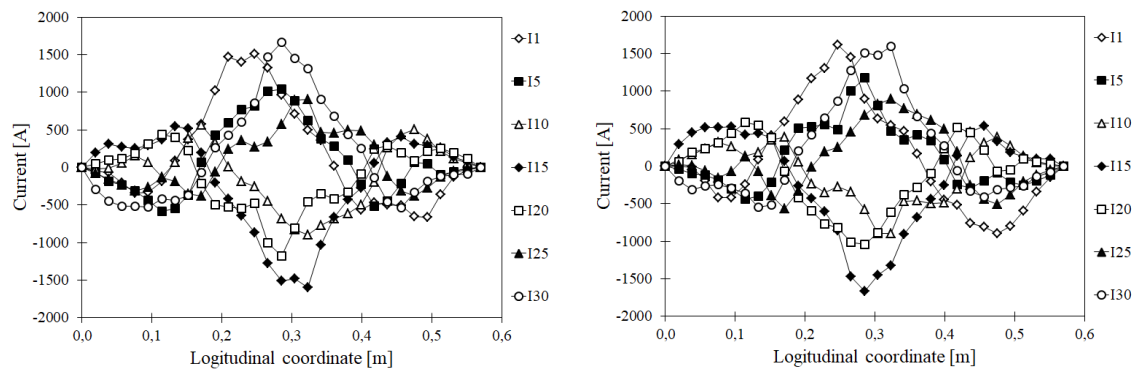

Fig. 70: Current distribution in Cable 1 (left) and Cable 2 (right) at 4 s due to the AC pulsed field of 0.2 T at 0.4 Hz.

6.6. Comparison between numerical models

A numerical analysis campaign has been carried out for the comparison between the two numerical codes in order to evaluate their reliability under the same geometrical and boundary conditions. At this purpose we evaluate the ohmic loss in the PF joint with both numerical codes using the simplified model of the PFJEU1 sample, considering the same excitations and geometry, after a previous transient analysis of the real PF6 DP joint model.

A "Magnetostatic Analysis" is carried out for the evaluation of a reference background field distribution in the joint region. A static background magnetic field $B_{ref} = 1$ T is generated at the center of an external copper coil with only one winding ($N = 1$), fed with a constant current $I_{ref} = 2710.5$ kA according to the following analytical equation used as a first estimation:

$$B_{ref} = \frac{\mu_0 N I_{ref}}{2} \cdot \frac{1}{\sqrt{\left(\frac{H}{2}\right)^2 + \left(\frac{R_{int}+R_{est}}{2}\right)^2}} \tag{64}$$

Coil's material is the copper in the ANSYS Maxwell library. The 3D FEM code evaluates the background field distribution in a vacuum region which dimension is set in order to respect well the boundary condition of $B = 0$ T at infinite distance from the coil. The magnetic field profile is evaluated in a more accurate way inside the coil where the joint will be further placed, so a vacuum cylinder is built around the solid model (Fig. 71). Dimensions of the model are given in Tab. 22.
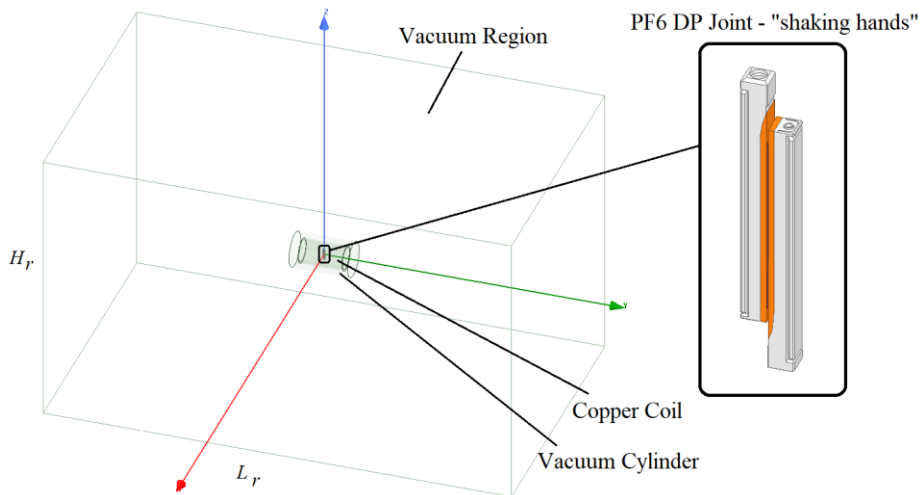
Fig. 71: Magnetostatic model in the 3D FEM code for background field modelling.

Domain	Dmensions [mm]		
Copper Coil	$R_{int} = 750$	$R_{est} = 850$	$H = 3000$
Vacuum Cylinder	$R_c = 1200$		$H_c = 4000$
Vacuum Region	$L_r = 19200$		$H_r = 32000$

Tab.22: Dimensions of the computational domains in the 3D FEM code.

We compare the axial component B_y [T] of background field along the axial and radial direction obtained with the two numerical codes, finding a very good agreement within a maximal percentage error less than 0.03% and 0.12% in axial and radial direction respectively, as shown in Fig. 72; the magnetic field flux appears very uniform in the coil center. The radial field component is affected only by numerical error in the 3D FEM code and is comparable with the radial profile obtained in THELMA code, where B_r= 0 T is imposed as boundary condition. Extending the calculation in x and z direction of the background field we found the same accuracy and reliability of the two numerical model. We can assume that a numerical model of the PF joint will be subjected to a uniform background field of 1 T if placed at the very center of the excitation coil.

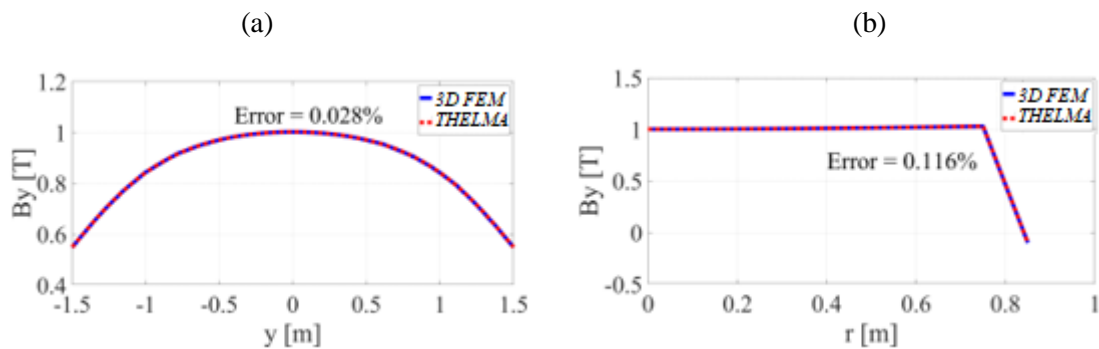(a)   (b)

Fig. 72: Comparison of (a) axial profile and (b) radial profile of the axial component of background field in the two numerical codes.

Since background field calculated distribution is reliable for the electromagnetic steady state, we can use the same geometry of the "Magnetostatic Analysis" in a "Transient Analysis" in which the excitation current varies in time generating a magnetic transient inside the coil, where the joint is placed. The joint will be then affected by eddy current loss, which steady state value depends on material resistivity and field variation frequency, according to eq. 49.

We want to evaluate the transient response of the PF6 DP join to a variation of B_{ref} in time in three directions independently, studying the effect of a magnetic field ramp of 0.5 T/s generated by an excitation current ramp of 1355.25 kA/s for 2 s in the external coil, thus having a constant magnetic field of B_{ref} = 1 T with a constant nominal current of I_{ref} = 2710.5 kA at the end of the transient regime. Since time variation of excitation current is constant, inductive response of PF6 joint inside the coil is supposed to reach a constant steady state value after a first transient regime in which an *e.m.f.* is induced and counteracts the magnetic flux variation, according to Faraday's Law (eq. 7). Ohmic loss steady state values in PF6 DP joint are given in Tab. 23 for every direction of 0.5 T/s background field ramp.

Ohmic Loss for 0.5 T/s field ramp [W]			
Domain	x	y	z
Copper	5.3	31.9	2.5
316L	2.4	0.5	0.6
Joint	7.7	32.4	3.1

Tab. 23: Ohmic loss steady state values in PF6 DP joint for 0.5 T/s field ramp in the three directions.

With a field ramp along *x* axis we found the maximum contribution of stainless steel in total ohmic loss (23.9% of power dissipated in the whole joint): this is because most of the current paths induced by the flux field variation are located on the stainless steel surface, however the most of ohmic loss is found in the copper domain as we see in Fig. 73. With a field ramp along *y* axis we have the maximum total power of 32.4 W (in which less than 2% is found in the stainless steel) because the induced current loops are found in the large copper cross section interested by a great magnetic flux variation in time, as we can see in Fig. 74. With a field ramp along *z* axis we have the minimum total power of 3.1 W, which 80% is found in the copper domain (the most conductive) and where current loops are mostly found as we can see in Fig. 75.
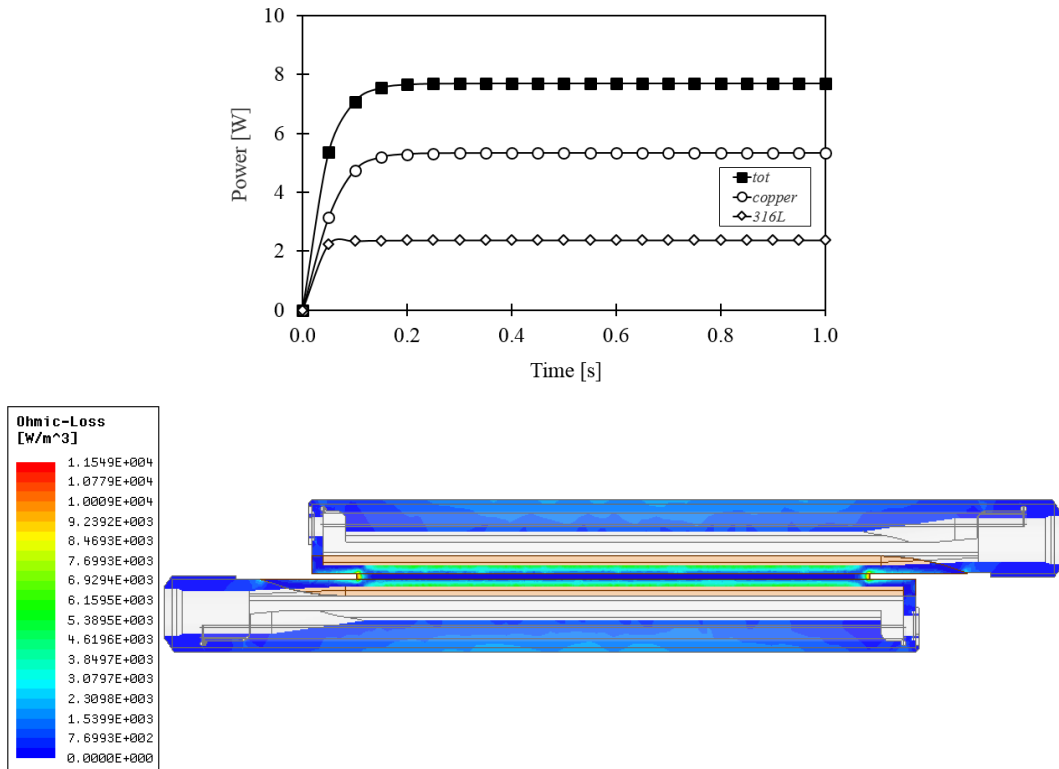

Fig. 73: Transient response (top) and ohmic loss distribution in *Y-Z* section view of PF6 DP joint (bottom) for a 0.5 T/s field ramp along *x* axis.
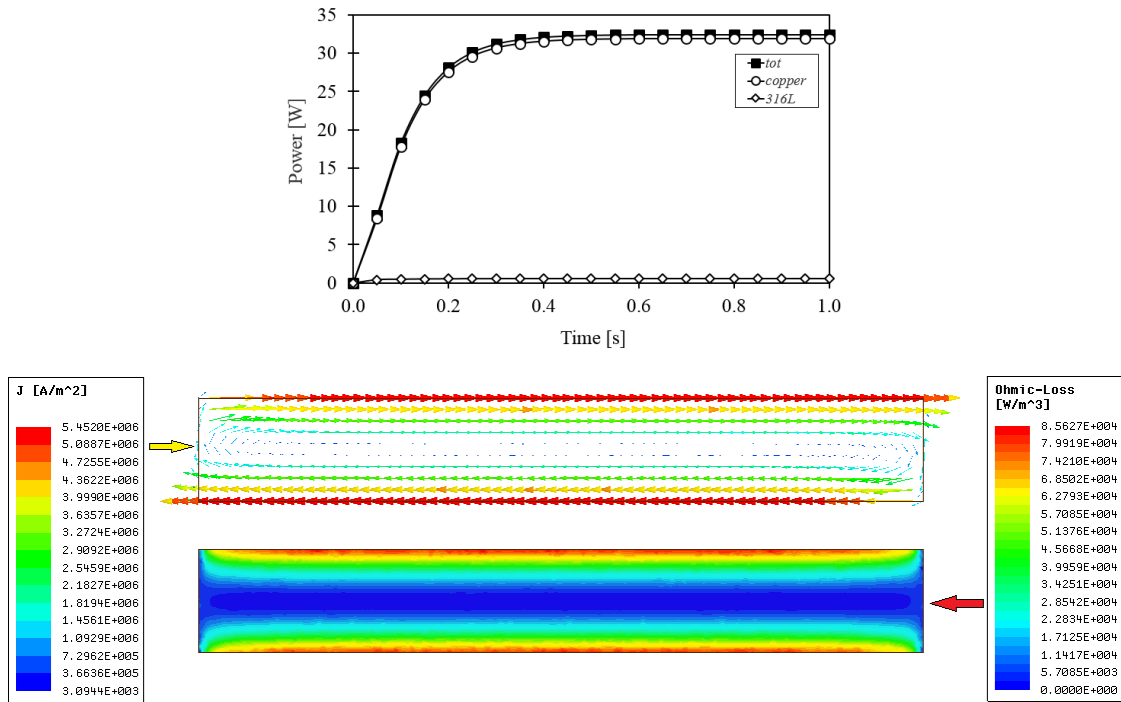
Fig. 74: Transient response (top) and induced current and ohmic loss distributions in *X-Z* section view of PF6 DP joint copper shim (bottom) for a 0.5 T/s field ramp along *y* axis.
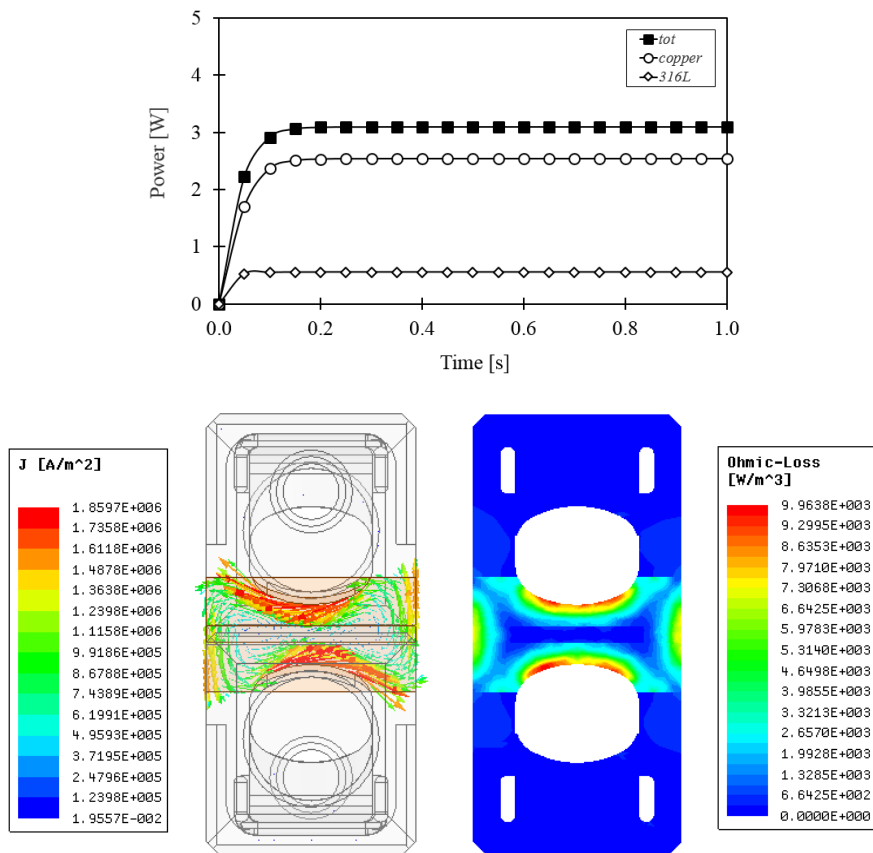

Fig. 75: Induced current (left) and ohmic loss distribution (right) in *X-Y* section view of PF6 DP joint for a 0.5 T/s field ramp along *z* axis.

The comparison of ohmic loss calculation in the two numerical codes is shown in Fig. 76 considering the same simplified model of PFJEU1 (Fig. 59 left). We can see that the steady state value is comparable, with a maximum percentage error of less than 0.25%. In the transient region a slower increasing of dissipation in time is found in the 3D FEM code, where the inductive effects are considered for every direction of the current in the joint, whereas the THELMA code neglects the inductive effects due to the transversal current crossing the joint plane from a cable to the other. The time constant of the electrical *RL* equivalent circuit is lower for the THELMA code, that reach fast the same steady state solution found in the 3D FEM code.
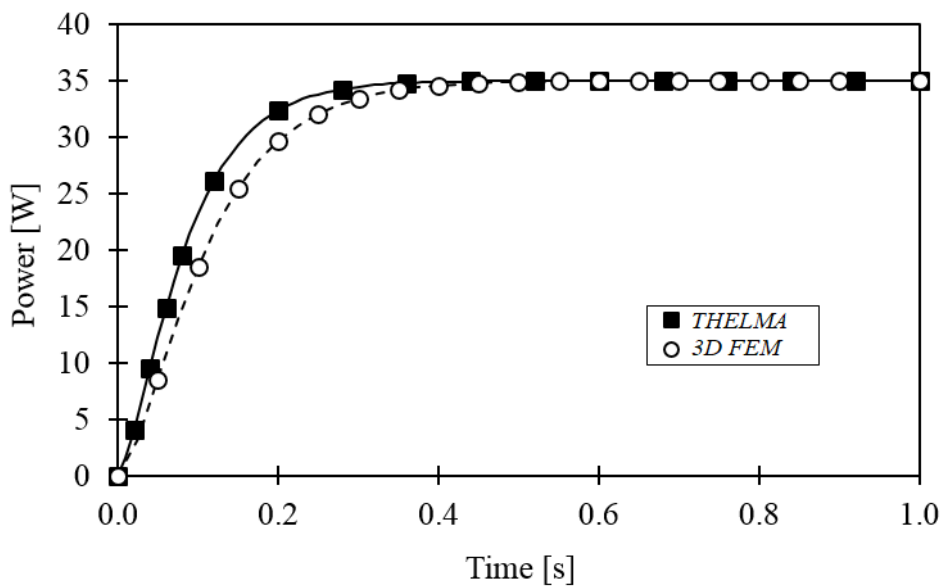

Fig. 76: Transient response comparison between the two numerical codes; eddy current loss decades faster in the THELMA code (higher initial slope of power vs. time curve) reaching the same steady state value of 3D FEM model.

7. Conclusions

The electromagnetic analysis of transients in the joint between two ITER Poloidal Field (PF) Cable-in-Conduit conductors (CICC) has been performed. The PF joint consists of a copper saddle embedded in a stainless steel structure of about 500 mm in length and it has been analyzed in two possible configurations, depending on the cable position: the "shaking hands" configuration in relevant for the real design of the joint between two Double Pancakes (DP) of the PF6 coil, whereas the "praying hands" configuration is relevant for the PFJEU1 SULTAN sample.

The DC resistance and the AC losses of PFJEU1 have been measured in the SULTAN test facility (Villigen, Switzerland) in October 2016. A 3D FEM model of the PFJEU1 sample was developed for the modeling of the superconducting junction whereas the comparison of AC losses has been performed using an integral model in the THELMA code, developed at the LIMSA laboratory of the University of Bologna.

The experimental analysis of the PFJEU1 sample is performed using a post-processing code. Results are compared with those reported by SULTAN, showing a difference in the energy losses at low frequencies and an underrating of the peak losses. A possible explanation of this might be the use of different datasets for the helium enthalpy evaluation, however the general trend of the losses vs. frequency curve for the PFJEU1 is respected. The DC resistance evaluation is well in line with reference values, showing an increasing of the joint resistance with EM cycling. The calorimetric measurements are reliable only for high currents.

Both numerical codes are not validated through the comparison between experimental results. The 3D FEM model does not take in account the twisted cable layout and contact resistance between cable and jacket; this could explain the difference in the joint resistance measurements. Since the superconducting cable is equipotential, due to the high longitudinal conductivity, the voltage drop is found only in the joint domain, mainly at the copper interface between the two bimetallic boxes, therefore is not possible to evidence the difference between the DC resistance measured at the two sensors sections (far and near) in the PFJEU1 SULTAN sample. The calculated resistance, in the range of 1.4-2.2 nΩ, is obtained by the fitting of the transvers conductivity of the NbTi cable and taking in account different copper resistivity, however these results do not allow us to obtain a good evaluation of the AC losses. Only a qualitative analysis of the real PF6 DP joint (without superconducting cables) can be considered. The maximum value of the AC losses is found for a background field varying in y direction, perpendicular to the joint plane, where the biggest current loops are found in the copper domain.

The THELMA model is validated in the range of 0 Hz – 1 Hz by using the per-unit-surface conductivity between cable elements as the fitting parameter of the model.

The numerical analysis at frequency up to 10 Hz shows an unexpected behavior of the energy losses in the joint. Therefore a more reliable simulation might be obtained by updating the dimensions and the electric parameters of the PFJEU1 model. The stainless steel domain is neglected in the THELMA model to reduce the computational burden, however it could have effect in the shielding current that could reduce the AC losses in the copper domain.

The THELMA model has been validated through the AC losses analysis of the simplified model of the PFJEU1 SULTAN sample via the comparison with the 3D FEM code, showing a good agreement at the steady state regime under the same geometric and boundary conditions. In the THELMA code the inductive effects due to the transversal currents in the joint are neglected, thus taking in account a lower inductance. Therefore the transient response in THELMA model is faster than that in the 3D FEM code, which takes in account the inducting effects of the eddy currents in all the three directions. The two numerical models reach the same value of AC losses at the steady state.

References

[1] C. Sborchia, *et al*., "Overview of ITER Magnet System and European Contribution*", IEEE/NPSS 24th Symposium on Fusion Engineering*, 2011.

[2] R. J. Donnelly, 1981, Cryogenics In *Physics Vade Mecum*, ed H. L. Anderson American Institute of Physics, New York.

[3] Mikael Holm, "Industrial Manufacturing of Low Temperature Superconducting (LTS) wires", European Summer School of Superconductivity 2011, Harjattula Mansion, Turku, Finland.

[4] EFDA Material Data Compilation for Superconductor Simulation, P. Bauer, H. Rajainmaki, E. Salpietro, EFDA CSU, Garching, 04/18/07.

[5] J.Simon, E.S.Drexler and R.P.Reed, "Properties of Copper and Copper Alloys at Cryogenic Temperatures", 850 pages, February 1992, U.S. Government Printing Office, Washington, DC 20402-9325.

[6] N. N Martovetsky, "Analysis of Losses in ITER Joints in a Varying Parallel Field", *IEEE Transactions on Applied Superconductivity*, vol. 7, no. 2, June 1997, pp. 266-269.

[7] S. A. Lelekhov, V. Tronza, "AC Loss Before and After Cyclic Mechanical Loading in the ITER FF CICCs*", IEEE Transactions on Applied Superconductivity,* vol. 24, no. 3, June 2014, 4201005.

[8] M. N. Wilson, *Superconducting Magnet*, Oxford, U.K.: Clarendon, 1983.

[9] S. A. Lelekhov, "A physical model and numerical method for losses investigation in superconducting cable-in-conduit conductors (CICC)", *Cryogenics,* vol. 46, no. 1, pp. 1-8, Jan. 2006.

[10] P. Bruzzone *et al*., "Coupling Current Losses Bench Mark Test of ITER Subsize Conductor", presented at MT-14 Conference, in press.

[11] M. N. Wilson, "NbTi superconductors with low AC loss: A review", *Cryogenics,* vol. 48 (2008), pp. 381-395.

[12] A. Nijhuis *et al*., "Change of interstrand contact resistance and coupling loss in various prototype ITER NbTi conductors with transverse loading in the Twente Cryogenic Cable Press up to 40,000 cycles", *Cryogenics,* vol. 44 (2004), pp. 319-339.

[13] E. P. A. van Lanen *et al*., "Full-scale calculation of the coupling losses in ITER size cable-in-conduit conductors", *Supercond. Sci. Technol*., vol. 25 (2012) 025012.

[14] V. Corato *et al*., "Direct measurement of interfilament resistance in Nb3Sn strands", *J. Appl. Phys*., vol. 105, pp. 093930 1-093930 4, 2009.

[15] C. Zhou *et al*., "Direct Measurement of Inter-Filament Resistance in Superconducting Multifilamentary NbTi and Nb3Sn Strands", *IEEE Transactions on Applied Superconductivity,* vol. 21, no. 3, June 2011, pp. 2501-2504.

[16] P. Bruzzone *et al*., "Design and R&D Results of the Joints for the ITER Conductor", *IEEE Transactions on Applied Superconductivity,* vol. 7, no.23, June 1997, pp. 461-464.

[17] A. Nijhuis *et al*., "Electromagnetic and mechanical AC loss of an ITER TF model coil conductor (DP4) under transverse cyclic loading", *IEEE Transactions on Applied Superconductivity,* vol. 10, no. 1, Mar. 2000, pp. 588-591.

[18] E. P. A. van Lanen *et al*.,"Validation of a strand-level CICC-joint coupling loss model", *Supercond. Sci. Technol*., vol. 25 (2012) 025013.

[19] H. Raajainmaki *et al*., "The ITER Magnet System: Status of Design and Procurements", Summer School, Kullaa, 17 June 2008.

[20] Y. Yao *et al*., "Design and Analysis of Full Size Joint Sample for ITER PF Coil", *J. Fusion Energy*, vol. 34, 2015, pp. 802-807.

[21] S. Nicollet *et al*., "Quench of ITER Poloidal Field Coils: Influence of some initiation parameters on thermo-hydraulic detection signals and main impact on cryogenic system", *Cryogenics*, vol.53, Jan. 2014, pp. 86-93.

[22] B. S. Lim *et al*., "Design of the ITER PF Coils", *IEEE Transactions on Applied Superconductivity,* vol. 21, no. 3, Jun. 2011, pp. 1918-1921.

[23] G. Rolando *et al*., "Analysis of Heat Load, Current Margin and Current Nonuniformity in ITER PF Coil Joints", *IEEE Transactions on Applied Superconductivity,* vol. 23, no. 3, Jun. 2013, 4201405.

[24] B. S. Lim *et al* "Development of the ITER PF Coils", *IEEE Transactions on Applied Superconductivity,* vol. 22, no. 3, Jun. 2012, 4201404.

[25] F. Simon *et al*., "Reliability considerations for the ITER poloidal field coils", *IEEE Transactions on Applied Superconductivity,* vol. 20, pp. 423-426, 2010.

[26] Y. Karasev *et al*., "Characterization of NbTi Strands in the Process of Industrial Production for the ITER Poloidal Field Coils", *IEEE Transactions on Applied Superconductivity,* vol. 26, no. 4, Jun. 2016, 6000104.

[27] C. Sborchia *et al*., "The ITER magnet system: progress on construction", *Nucl. Fusion*, vol. 54, 2014, 013006.

[28] Y. Ilyin *et al*., "Operating limits of the ITER poloidal field coils", *IEEE Transactions on Applied Superconductivity,* vol. 20, pp. 415-418, 2010.

[29] B. Turck *et al*., "Conceptual and experimental studies of electrical joints for NET-ITER coils", *Proceedings of the 17th SOFT (Roma, 1992),* p. 967.

[30] D. Ciazynski *et al*., "Test results of subsize joints between Nb3Sn cables as a first step for a design of joints for NET-ITER coils", *Proceedings of the 18th SOFT (Karlsruhe, 1994),* in press.

[31] D. Ciazynski *et al*., "Results of the European Study on Conductor Joints for ITER Coils", *IEEE Transactions on Magnetics*, vol. 32, no. 4, Jul. 1996, pp. 2332-2335.

[32]. B. Smith *et al*., "PTF; a new facility for pulse field testing of large scale superconducting." *IEEE transactions on applied superconductivity*, *7*(2), 1997, pp. 1049-1052.

[33] B. Gulenc *et al*., "Production of wire reinforced composite materials through explosive welding", *Archives of Civil and Mechanical Engineering*, vol. 16, issue 1, Jan. 2016, pp. 1-8.

[34] D. Ciazynski *et al*., "Fabrication of the First European Full-Size Joint Sample for ITER", *IEEE Transactions on Applied Superconductivity,* vol. 9, no. 2, Jun. 1999, pp. 648-651.

[35] D. Ciazynski *et al.*, "Large superconductors and joints for fusion magnets: from conceptual design to testing at full scale", Nuclear Fusion, vol. 41, no. 2, pp. 223-226, 2001.

[36] D. Ciazynski *et al.*, "Test Results and Analysis of Two European Full-Suze Conductor Samples for ITER", *IEEE Transactions on Applied Superconductivity,* vol. 10, no. 1, Mar. 2000, pp. 1058-1061.

[37] P. Decol *et al.*, "Joints for large superconducting conductors", *Fusion Engineering and Design*, 58-59, 2001, pp. 123-127.

[38] D. Ciazynski, A. Martinez, "Electrical and Thermal Design and Analyses of Joints for the ITER PF Coils", *IEEE Transactions on Applied Superconductivity,* vol. 12, no. 1, Mar. 2002, pp. 538-542.

[39] B. Jager *et al.*, "Test facility for joints of subsize cable-in-conduit conductors for NET/ITER winding studies", *Adv. Cryo. Engineering*, vol. 41°, p. 521, 1996.

[40] L. Zani *et al.*, "Manufacture and Test of NbTi Subsize Joint Samples for the ITER Poloidal Field Coils", *IEEE Transactions on Applied Superconductivity,* vol. 13, no. 2, Jun. 2003, pp. 1460-1463.

[41] P. Decol *et al.*, "Design and manufacture of a prototype NbTi full-size joint sample for the ITER poloidal field coils", *Fusion Engineering and Design*, 66-68, 2003, pp. 1165-1169.

[42] D. Ciazynski *et al.*, "Test results on the first 50 kA NbTi full size sample for the International Thermonuclear Experimental Reactor", *Supercond. Sci. Technol.*, vol. 17, 2004, pp. 155-160.

[43] V. I. Bondarenko *et al.*, "Technology and Tooling to Manufacture Low-Ohm (< 2 nΩ) Electrical Joints of the ITER PF1 Coil", *IEEE Transactions on Applied Superconductivity,* vol. 23, no. 2, Jun. 2013, 4201605.

[44] O. Kovalchuk *et al.*, "Test of PF1 Coil Electrical Joint", *IEEE Transactions on Applied Superconductivity,* vol. 28, no. 3, Apr. 2018, 4205104.

[45] Y. Ilyin *et al.*, "Qualification Program of Lap Joints for ITER Coils", *IEEE Transactions on Applied Superconductivity,* vol. 28, no. 3, Apr. 2018, 4201306.

[46] Y. Ilyin *et al.*, "Simulations of twin-box joints for ITER PF coils", *IEEE Transactions on Applied Superconductivity,* vol. 24, no. 3, Jun. 2014, 9001905.

[47] Y. Ilyin *et al.*, "Analysis of ITER PF coil joint design under reference operating scenario", *IEEE Transactions on Applied Superconductivity,* vol. 26, no. 4, Jun. 2016, 4201305.

[48] P. F. Pison *et al.*, "The Effect of specific manufacturing Characteristics on PF ITER Full-Size Joint Performances", presented poster at ASG 2018, Seattle, USA.

[49] SPC PFJEU1 SULTAN Sample Test Report, October 2016.

[50] A. Baikalov *et al.*, "Analyses of the ITER Poloidal Coil joints cold test results", *MT25 Meeting*, Amsterdam, 30 August 2017.

[51] R. Zanino *et al.*, "Modeling AC losses in the ITER NbTi poloidal field full size joint sample (PF-FSJS) using the THELMA code", *Fusion Eng. Des.C,* 2005, pp. 75–79.

[52] M. Ciotti *et al.*, "THELMA code electromagnetic model of ITER superconducting cables and application to the ENEA stability experiment", *Supercond. Sci. Technol.*, vol. 19, 2006, pp. 987–997.